Master Thesis

Gas Dynamics in Early Type Galaxies

Gasdynamik von Early Type Galaxien

Alexandra Shelest

Supervised by / Betreut von:

Dr. Federico Lelli

European Southern Observatory, Garching

Prof. Ralf Bender

Ludwig Maximilian University, Munich

November 23, 2019

To my amazing Dad.

Contents

Chapter 1

Introduction

1.1 Astrophysical evidence of dark matter

Dark matter is one of the most intriguing present-day scientific mysteries. Observations show that visible (baryonic) matter is not enough to explain the dynamics of galaxies, galaxy clusters, and the Universe as a whole. To fix the discrepancy, we have to either introduce a new type of (unseen, i.e., dark) matter, or to alter the laws of gravity, i.e., general relativity. To date, the first approach is more widely used and developed.
In the first two sections, we will present the observational evidence of missing matter and possible explanations in the dark matter framework. We will briefly discuss competing theories in the third section.

Vertical motions in the Milky Way. Historically, the first indications of missing matter came from the analysis of the vertical motion of stars in the Solar neighbourhood. The stars can be used as tracers of the galactic gravitational potential, which, itself, can be reconstructed from the distribution of visible matter. First estimates of the vertical gravitational potential using this technique date back to the 20s and 30s of the past century (Kapteyn, 1922, Oort, 1932). A theory describing the vertical force was developed by Kapteyn and Oort in the same works, and was later refined by Spitzer (1942) and Bahcall (1982).
Current estimates show that in the solar neighbourhood about 1/5 of the matter density is in dark matter with roughly 0.02 $M_\odot/pc^3$ (see, e.g., Hagen & Helmi, 2018, for the local dark matter density and, e.g., Table 2 in Kramer & Randall, 2016, for the local densities of visible galactic components).

Dynamics of galaxy clusters. The dynamics of galaxies in galaxy clusters also points to an invisible massive component. Assuming that a galaxy cluster is virialized (i.e., in dynamical equilibrium), the velocities of its individual galaxies are found to be much higher than expected from the visible matter distribution. Without an additional dark matter component, they should fly apart.
This observation was first made by Fritz Zwicky in 1933 on the Coma cluster (Zwicky, 1933) and was since confirmed on many other galaxy clusters. More recent analysis of X-ray emission from hot gas that fills galaxy clusters also confirms a deeper gravitational potential than produced by visible matter (e.g., Pointecouteau et al., 2005).

Galaxy rotation curves. Rotation curves of galaxies are another key observation of missing matter, and the main focus of this thesis. A rotation curve shows the rotation velocity of the galaxy as a function of radius, from which the gravitational potential can be deduced. From Newtonian gravity, the rotation curve is predicted to decline from a certain radius on, both for a spherical (Kent, 1986) and a disk-shaped (Casertano, 1983) mass distribution. However, observed rotation curves are found to be flat. First observations of this discrepancy come from observations of ionized gas and date back to the 1960-70s (Burbidge et al., 1959, Rubin et al., 1970, 1978, 1982). They were confirmed by rotation curves of neutral hydrogen gas, HI, which extends farther out than the stellar body of the galaxy and hence traces the gravitational potential up to larger radii (Rogstad & Shostak, 1972, Bosma, 1978, van Albada, 1985, Begeman, 1987).
The stellar mass of a galaxy is not directly measurable. It is estimated from the galactic luminosity using an empirically determined proportionality factor, the mass-to-light ratio (M/L). Historically, the flat rotation curve shape was explained by a steep rise of this ratio with radius, associated with the existence of a faint, but massive stellar population in the outskirts of galaxies (e.g., Oort, 1940, Roberts, 1975). However, this hypothesis was ruled

out as no stellar populations with M/L values high enough were found. Also, a more massive stellar type would not fit into the stellar evolution sequence or into galaxy evolution models (as developed by Tinsley, 1972a, 1972b, 1975). Therefore, the missing matter is associated with a so-called dark matter halo, in which the galaxy is embedded.

Stability of disk galaxies. In 1973, Ostriker & Peebles found from numerical calculations that thin rotating disks become thicker and form a bar during only one rotation period, and are eventually destroyed by instabilities. Since this clearly contradicted the observations of stable disk galaxies, a stabilizing mechanism was needed, for example a large spherical mass distribution enveloping the galaxy. This theoretical consideration supports the dark matter halo concept.

Gravitational lensing. Since the assumed dark matter halo is thought to be very massive, it should be deflecting by-passing light by its gravitational potential. Indeed, strong and weak gravitational lensing shows evidence of dark matter haloes in galaxies and in galaxy clusters. It also shows that the majority of the dark matter is not self-interacting, i.e., it does not clump when two galaxies or galaxy clusters pass through each other, as does, for instance, gas (Markevitch et al., 2002, Clowe et al., 2004).

1.2 Cosmological evidence of dark matter

By the late 1970s, there was plenty of astronomical evidence for the need of missing mass, and, since its properties could not be described by known stellar types or gas, non-baryonic dark matter has already been suggested. The real evidence for the non-baryonic nature of the dark matter, however, comes from cosmology. To understand the implications of the various observations, we need to introduce the Big Bang Theory. We sketch below a brief overview. Explaining the theory in more detail is beyond the scope of this thesis. For more information, please consult Zeldovich & Novikov (1983), or recent reviews (e.g., Samtleben et al., 2007 on CMB, Mukhanov, 2016 on inflation, Mukhanov, 2004 on primordial nucleosynthesis, etc.).

The Big Bang Theory. The Big Bang theory describes the evolution of the Universe starting from the first moments of its existence until present time. According to this theory, the Universe originated from a 'big bang', being very hot and dense in the beginning and gradually cooling by expansion. This process is marked by several important stages.
In the very beginning, there was a stage known as inflation. In this stage, the young Universe experienced a phase of exponentially accelerated expansion. During this expansion, quantum vacuum fluctuations, that were present in the pre-inflationary universe, got stretched to galactic scales, staying at nearly the same amplitude. This short period is crucial for structure formation in the Universe (see Guth, 1981, Linde, 1982, Steinhardt, 1983).
After inflation ended, the Universe continued to expand and cool, but at a slower rate. The details of particle physics processes happening at these early evolution stages are not relevant for this thesis. It is sufficient to say, that eventually the temperature got low enough for protons and neutrons to form light nuclei like deuterium, helium and lithium. The efficiency of this process, known as the primordial nucleosynthesis, depends on the matter density and therefore decreases with time. Since unbound neutrons are unstable, the nucleosynthesis is highly time-restricted, ending when all free neutrons decay. The amount of primordial baryons in the Universe is constrained by this short evolution period (for a

historical and physical review of the primordial nucleosynthesis, see Schramm, 1998, and refernences therein).
As the temperature and density of the Universe dropped further, electrons bound to the nuclei. This process is known as recombination. Photons are scattered much less by neutral atoms than they are by plasma, so this is when the Universe became transparent. We observe the freed photons in the cosmic microwave background (CMB). This background radiation is highly isotropic and has a blackbody spectrum (Smoot et al., 1992).
After recombination, gas filling the Universe started to collapse due to gravitational forces. (Before, the radiation pressure was preventing this). These initial density perturbations evolved to the structures we observe today, like galaxies and clusters.

The Cosmic microwave background. In 1964, the cosmic microwave background was discovered. This was one of the first important confirmations of the Big Bang Theory. It was found to be largely isotropic, in agreement with expectations (Doroshkevich & Novikov, 1964). As the measurement quality improved, anisotropies in the CMB temperature were measured. While the dipole anisotropy comes from the superposition of the movements of the Earth, the Sun and the Galaxy, higher order anisotropies map density fluctuations at recombination, which acted as seeds of structure formation. The scale of these anisotropies is of the order of 10^{-5} (Smoot et al., 1992).
Today, at $z = 0$, we observe complex structures in the Universe: galaxies are not distributed uniformly, but form a 'Cosmic Web', with galaxy-rich filaments and galaxy-poor voids. It can be calculated that, to form these structures in the provided time, density fluctuations at $z \sim 1000$ have to be of the order of 10^{-3}, so 100 times larger than observed.
In 1978, White & Rees proposed a non-baryonic explanation to structure formation consistent with much smaller fluctuations in the CMB. They could explain a deepening of the gravitational potentials by introducing a non-baryonic matter component, which decoupled from the ordinary matter before recombination and could already cluster at the density fluctuations coming from the pre-inflational Universe. After recombination, the baryonic matter falls into the already existing potential wells of the non-baryonic matter, speeding up structure formation and explaining the large-scale structure at $z = 0$.
The type of matter introduced above is called Cold Dark Matter (CDM), as it needs to have small velocities to efficiently cluster. Its particle nature is not known, although there are many competing theories and the experimental search for it is ongoing. We will not introduce any particle candidates for the CDM as this is beyond the scope of this thesis.

The power spectrum of the CMB. More insight about the Universe comes from analysing the structure of the CMB anisotropy (see, e.g., Bennett et al., 2003, Komatsu, 2009). For that, the CMB is decomposed into spherical harmonic functions, analogous to 2D Fourier decomposition, but on a sphere. The derived power spectrum of the CMB depends crucially on the matter-energy content of the Universe. The position of the first peak of the spectrum shows that the Universe is flat to a high accuracy, i.e. that the density of the Universe is equal to ρ_{crit}, where $\rho_{\mathrm{crit}} = \frac{3\mathrm{H}_0}{8\pi G}$ with the Hubble constant H_0. If this value was different, it would suggest that we live in an either open or closed Universe. Since the big bang nucleosynthesis predicts that baryons make up 5% of the critical density of the Universe, 95% of the mass-energy must be in some other form.
From the positions and heights of the next several peaks the total matter density can be derived. According to the latest measurements (Planck Collaboration et al., 2018), it is $(31.5 \pm 0.7)\%$, so ca. 26% of the matter must be of non-baryonic nature. The remaining 69% is assigned to another poorly understood component of the universe, the dark energy, which drives the accelerated expansion of the Universe that we observe with Type-Ia super-

novae (Riess et al., 1998).

Simulations. The cosmological picture presented above is known as the ΛCDM cosmology, in which Λ denotes the cosmological constant (possibly related to dark energy), while CDM stands for cold dark matter. In this framework, a consistent picture of galaxy formation can be developed, known as hierarchical structure formation (Toomre, 1977). According to it, small dark matter haloes formed on the initial density perturbations. They grew through mergers and accretion of diffuse dark matter. Baryonic matter fell into the dark matter haloes after recombination and formed galaxies. The whole process becomes quickly non-linear, so numerical simulations are needed to probe whether the theory is correct.
Starting from the late 1970s, such N-body simulations have become feasible. They simulate the evolution of the Universe, starting from initial perturbations and taking into account the tested models of cosmology (for reviews, see Ciardi & Ferrara, 2005, Borgani & Kravtsov, 2011). When ΛCDM is probed, initial conditions are set to mimic perturbations predicted by inflation theory.
The results of these simulations reproduce the structure of the Universe remarkably well on supergalactic scales (see, e.g.,Navarro et al., 1996, Springel et al., 2005, Boylan-Kolchin et al., 2009), but there are some discrepancies between the simulations and the observations on galaxy scales (e.g., Bullock & Boylan-Kolchin, 2017).

1.3 Competing theories

We have described how cold dark matter can explain various astrophysical and cosmological observations. There are, however, competing theories that try to solve the missing mass problem not by introducing a new particle, but by altering the theory of gravity. The most prominent example is the Modified Newtonian Dynamics theory (MOND) by Milgrom (Milgrom, 1983), which proposes a different law of gravity in the non-relativistic regime when the accelerations are smaller than a critical value. At higher accelerations, Newtonian laws act as usual. This theory gives a surprisingly good phenomenological description of galactic dynamics, finding the same critical acceleration for different types of galaxies (see Lelli et al., 2016 and references therein). However, a fully satisfactory extension of the theory to general relativity does not exist yet, so a MOND-like approach cannot currently explain the CMB and the cosmological evolution of the Universe (Sanders & McGaugh, 2002, Famaey & McGaugh, 2012).
Theories of modified gravity will not be discussed for the rest of this thesis.

1.4 Galaxies as island universes

Galaxies can be classified based on their morphology and physical properties. Edwin Hubble was the first to perform such a classification (Hubble, 1926) and his naming scheme for galaxies is still used, although it has been shown that his underlying ideas of galaxy evolution have been erroneous (Buta, 2013). This scheme is presented in Fig. 1.1 and known as the 'tuning fork diagram'.
All the galaxies on the left side are Early Type galaxies (ETGs). They can be either ellipticals (E) or lenticulars (S0). The galaxies in the 'forked' part of the diagram are Late Type Galaxies (LTGs). These are disk galaxies that are divided into branches depending

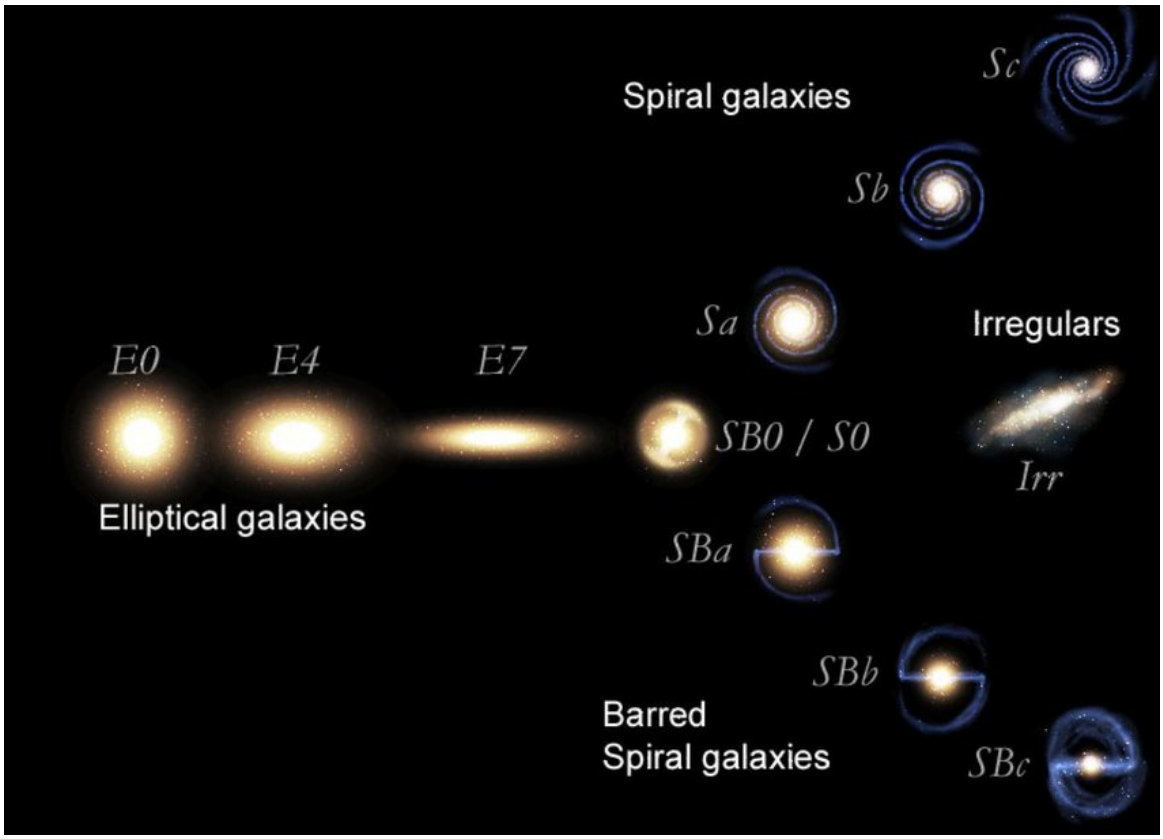

Figure 1.1: The Hubble sequence of galaxies, known as the 'tuning fork'. Figure credits: Fahad Sulehria, www.novacelestia.com (Astronomical illustrations and space art).

on whether they have or do not have a bar. Their position on the diagram is defined by the visible features and the winding of their spiral arms. Not included in the initial Hubble diagram are the Irregulars. These are galaxies that host lots of gas and star formation (Keel, 2007). Irregulars form a heterogeneous class of galaxies: they are either gas-righ galaxy mergers or low-mass dwarf galaxies (the so-called dwarf irregulars, dI).
LTGs are spirals and irregulars. Their stellar component can be divided into several parts: a disk, a stellar halo and, if existent, a bulge and/or a bar. The stellar halo is a roughly spherical, low-luminosity structure that contains a low percentage of the stellar mass. The halo stars are old and metal-poor and exhibit chaotic motions.
Most of the stellar mass is confined in the disk and the bulge. The disk generally exhibits circular motions, with random speeds less than 10% of the circular speed. Therefore, it is dynamically cold and thin. The disk luminosity can be approximately modeled by exponential functions both in the radial and the vertical direction, with the characteristic scaleheight being related to the characteristic scalelength. For most spiral galaxies, the disk extends for several kiloparsecs, and may abruptly end at a maximal radius, where, star formation is supposedly no longer efficient (see van der Kruit & Freeman, 2011, for a review).
The stars in the disk form multi-armed patterns, known as spiral arms, that typically contain younger stars and therefore are brighter in the optical (Roberts, 1969).
Spiral galaxies host considerable amounts of cold gas ($10^9 - 10^{12}$M$\odot$, e.g., Lelli et al., 2016), which is usually aligned and co-moving with the stellar disk. Typically, spiral arms contain giant molecular clouds, in which star formation is happening (Roberts, 1969). The amounts of hot gas tend to be small, so LTGs are faint in X-rays.

Many spiral galaxies have a bulge in the center. This is an ellipsoid stellar structure that has a higher star density and older stars than the disk. It is typically devoid of gas expect for its innermost part, where it may host star formation and nuclear star clusters. In contrast to disk stars, bulge stars have considerable random motions (for more information on spiral galaxies, see, e.g., Sparke & Gallagher, 2007, Keel, 2007).
In this thesis, we focus on ETGs. They are characterized by exhibiting no (or very weak) spiral structure and a ellipsoidal, rather than disky, shape. They have old stellar populations and host (nearly) no star-formation, therefore appearing redder than spiral galaxies. They also contain gas with lower densities than LTGs (Cappellari et al., 2011).
The breakthrough in the investigation of ETGs came when it has been discovered that ETGs exhibit a well-defined dichotomy (see Davies et al., 1983 Bender, 1988, Bender et al., 1989, Cappellari et al., 2011, and references therein). They can be subdivided into the classes of so-called slow and fast rotators (Kormendy & Bender, 1996, Emsellem et al., 2007) that not only have very different properties, but also differ in their evolution histories. These observations were later confirmed with integral-field spectroscopy (IFS), which provides velocity measurements at each point of the galaxy, rather than just along the main axis, as it was with long-slit spectrographs. Over the last 20 years, several large scale IFS surveys (SAURON, ATLAS^{3D}, etc.) collected data for hundreds of ETGs.
The slow rotators tend to be more massive ($M_V \lesssim -21.5$mag), have a very old, metal rich population (Thomas et al., 2005) and a boxy isophote shape[1](Bender, 1988). They contain hot X-ray emitting gas (Bender et al., 1989), but host (nearly) no atomic or molecular gas that is needed for star formation (Kormendy & Bender, 2012). As the name suggests, the rotation support of these galaxies is negligible over pressure support (Illingworth, 1977). These galaxies probably form in a series of mergers of massive, not star forming galaxies (although their formation history is still debated, see, e.g. Cappellari, 2016, Kormendy et al., 2009).
The fast rotators, on the other hand, are less luminous ($M_V \gtrsim -21.5$mag), have younger populations with respect to the slow rotators, and have disky isophotes, indicative of stellar disks with large bulges. While slow rotators typically exhibit cores (Ferranese et al, 1994), fast rotators are usually core-less (Faber et al., 1997). Also, they are not α-enhanced and do not contain X-ray emitting gas, but host small to medium amounts of cooler radio emitting gas and can have small amounts of star formation. Typically, they are axisymmetric, while slow rotators are triaxial (Kormendy & Bender, 2012, Cappellari, 2016). The angular momentum content and morphology of these galaxies suggest that they evolve from spirals with large bulges. Either through tidal interactions with the bulge or through outflow effects from supernovae and AGNs, the star formation in the galaxy gets quenched, while interactions with the environment might strip the galaxy of its gas and puff it up vertically. For more information on the ETGs and their evolution, see, e.g., Cappellari, 2016, Kormendy et al., 2009, Kormendy & Bender, 2012.

1.5 Gas as a tracer of galactic kinematics

The visible component of a galaxy is made of stars and gas. The stellar component can be used by itself to trace the gravitational potential of the galaxy. Gaseous disks, when existent, can cover different radial ranges. The HI disk can extend about twice as far as the stellar distribution does (van der Kruit & Freeman, 2011). Disks of other gaseous phases,

[1]isophote - curve of constant brightness

like molecules and ionized gas, are only found in the central parts of the galaxy.
The larger size of the HI disk is beneficial for using it as a tracer of the gravitational potential. Another advantage in looking at HI kinematics comes from its velocity dispersion. It is much lower than the velocity dispersion in the stellar disk, hence it provides a direct tracer of the circular velocity of a test particle, without the need of corrections for pressure support (so-called asymmetric drift).
From the elemental composition of the universe it is known that hydrogen forms 74% of the gas, helium makes up about 24% and heavier elements form $\lesssim 2\%$ of the gas (Wagoner et al., 1967). As mentioned above, HI disks can be very extended and therefore are a good dynamical tracer. However, they often have holes or depletions in the central parts, so other gas types have to be considered to fill the gap.
Using gas as a tracer of galactic kinematics requires three conditions: the gas of choice is present in sufficient concentration to be detected (as we have seen above, ETGs have been long thought to be devoid of gas due to its low surface densities), the gas has to have a strong and well identifiable emission line, and this emission line has to have a wavelength at which it can be well observed from Earth. The last one is a crucial factor in the choice of the lines used for observations, as the Earth atmosphere absorbs light at several frequencies. In the following sections, we will introduce the gases chosen for tracing the gravitational potential in this work.

1.5.1 The 21 cm line of atomic hydrogen

For tracing the HI emission, we use observations of the famous 21 cm line. The name is referring to the corresponding wavelength, which lies in the radio and can readily be measured from Earth.
Atomic hydrogen consists of an atom and an electron. The energies associated with level transitions of the electron lie in the optical and infrared. However, these wavelengths are subject to dust absorption, while radio waves penetrate dust clouds without alteration. Therefore, it is desirable to use transitions that emit photons of radio frequencies, i.e. transitions with the lowest energies possible.
Such a transition for the hydrogen atom comes from the hyperfine energy level splitting. In the ground state, the spins of the two particles can be either aligned or anti-aligned, the two states having slightly different energies. Naturally, the system goes to the state of minimal energy, namely the one where the spins are anti-parallel. The energy difference of 5.874 μeV is emitted in the form of a photon with the corresponding frequency of 1420.4 MHz (and wavelength 21.106 cm).
As the transition between the two states of different spin is forbidden, it happens only with a transition rate of $2.9 \cdot 10^{-15}$ per second. The extremely long lifetime of the hyperfine excited level together with the very big number of hydrogen atoms in the galaxies ensure that we can observe the 21cm line continuously and independent of the origin cloud temperature, as the process does not require any specific excitation temperature. This fact, together with the natural abundance of HI, explain the extensive use of 21 cm observations in astrophysics. The 21 cm line was predicted by van de Hulst in 1944 (van de Hulst, 1944) and first time observed by Ewen and Purcell in 1951 (Ewen & Purcell, 1951).

1.5.2 CO as a tracer of molecular hydrogen

For the innermost parts of the galaxies, we need a different gas tracer since ETGs often show central HI holes. Molecules emit light from electron transitions, just as atoms, but they can also emit light when they transition between different rotational and vibrational states. These processes have excitation energies much lower than the ones associated with

e^- transitions and hence emit in a different frequency range.
Cold molecular clouds are still dominated by hydrogen, now in the form of H_2. This molecule, however, is neutral, diatomic and symmetric. As it is made of two identical atoms, it possesses no dipole moment. The first rotational transition it possesses is quadrupolic. The corresponding radiation is very weak and lies in the far infrared. Both higher order rotational and vibrational transitions have higher excitation energies, making cold H_2 effectively invisible (see, e.g., Bolatto et al., 2013).
The next most abundant elements are helium (which, being monoatomic, is also very hard to observe), oxygen and carbon. The latter two form CO molecules that, being made out of two different atoms, possess a rotational dipole moment. The first rotational excitation energy of CO is very small (corresponding to roughly 5 K), making the $J = 1 \rightarrow 0$ transition with 2.6 mm the perfect aim for millimetre and sub-millimetre astronomy (Bolatto et al., 2013). The first observation of the CO($J = 1 \rightarrow 0$) line was performed by Wilson et al. in 1970.
The problem arises when trying to relate the measurable CO flux to the total molecular gas mass. Over the last 40 years, there have been debates about the accuracy of such a conversion (see Dickman et al., 1986, Bolatto et al., 2013, Clark & Glover, 2015 and references therein).
Commonly, the measured (velocity-integrated) luminosity of CO is related to a H_2 mass by an factor empirically established from observations in the Milky Way (Dame et al., 2001). Following Bolatto et al. (2013), we use the factor $X_{CO} = 2 \cdot 10^{20} \mathrm{cm}^{-2} (\mathrm{K\ km\ s}^{-1})^{-1}$ as estimated in the disk of the Milky Way.

1.5.3 Deriving the emitter velocity

The physically measurable observable in astronomy is not the velocity, but the frequency of the radio wave emitted by the object in consideration. To retrieve the velocity of the emitter from this measurement, one makes use of the relativistic Doppler effect (Einstein, 1905). In general it is given by

$$\nu = \nu_0 \cdot \frac{\sqrt{1 - (v/c)^2}}{1 - v/c \cdot \cos\theta}, \tag{1.1}$$

where ν and ν_0 are the measured and the emitted frequencies, respectively, v is the velocity of the emitter and θ is the angle between the velocity vector and the emission direction in the system of the receiver. $\theta = 0$ corresponds to the velocity and emission vectors aligning, i.e. the emitter moving right towards the receiver, while $\theta = \pi$ corresponds to the emitter moving straight away from the receiver.
However, galaxies rotate at velocities much smaller than the speed of light, therefore we can expand eq. 1.1 to first order in v/c to find

$$\nu = \nu_0 (1 - v/c), \tag{1.2}$$

where we also assumed that the galaxy is moving straight away from us.
From this, the velocity of the emitter can be expressed as

$$v = c \cdot (1 - \nu/\nu_0). \tag{1.3}$$

1.6 This thesis

The aim of this master thesis is to exploit interferometric observations of HI and CO lines to derive the rotation curves of early type galaxies. All previous rotation curve estimates

of ETGs are derived from stellar motion due to the low surface brightness of their gas. The increased observational power gives us the possibility to check whether rotation curves derived from gas motions and extending to higher radii fit our expectations. Also, it is interesting to test whether some empirical relations derived for late type galaxies also hold for the ETGs and can therefore be imposed as constraints on theoretical dark matter models.

This work will concentrate on the properties of fast rotators. To date, there are no extended rotation curves available for galaxies of that type. Lelli et al. (2017) attempted at estimating rotation curves for 9 slow rotating and 16 fast rotating ETGs, but for the fast rotators only two rotation curve points per galaxy were available. Another group, den Heijer et al. (2015), used the same observations of fast rotating ETGs as our work, but only derived the rotation velocity of the flat part of the rotation curve (i.e. at large radii). In this work, we derive the detailed rotation curves for three early type galaxies: NGC3626, NGC2824 and UGC6176. These are the only galaxies from the ATLAS^{3D} survey that have an inner CO disk and an outer extended HI disk. This allows us to trace the rotation curves from the inner parts (using CO) out to the very outer parts (using HI). We then fit various dark matter profiles to our rotation curves and place our findings in the context of knowledge acquired from galaxies of other types.

1.6.1 The data

We use data from ATLAS^{3D} (Cappellari et al., 2011), a large multiwavelength survey that focused on a volume-limited[2] sample of 260 nearby ETGs. It provides observations of these objects in radio, millimetre and optical. We use the observations of HI (Serra et al.) and CO (Alatalo et al.), specifically.
ATLAS^{3D} was one of the groundbreaking surveys verifying that ETGs do contain gas. Initially, ETGs have been thought to be devoid of interstellar gas due to its low surface brightness. Results of radio, millimetre- and submillimetre measurements by the ATLAS^{3D} collaboration showed that 40% of the observed non-cluster galaxies (and 10% of galaxies in the Virgo cluster) contain gas, but also this gas is found in different states - in some galaxies it is in regular structures such as disks and rings, while in others it is clumpy and disturbed, indicating recent or ongoing accretion events.
The ATLAS^{3D} group classified the HI morphology of the galaxies as D (when most of the gas forms regularly rotating disk or ring structures larger than the stellar body), d (when the disk or ring structures are smaller than the stellar body), u (when the gas is unsettled, forming tails or streams) or c (when the gas is found in clumps in or around the galaxy) (see Serra et al., 2012). Of the three galaxies chosen in this work, NGC2824 is characterized as d, while NGC3626 and UGC6176 are classified as D. Deeper observations of NGC2824, however, show that this galaxy also hosts an extended HI disk, so it should be re-classified as D (P. Serra, private communication). All of them are located outside of the Virgo cluster.

Additionally to the information about galaxy kinematics, we need the luminosity profiles of the galaxies. For those, we use data from SPARC (Lelli et al., 2016), which is the largest database to-date of galaxies with available 3.6 μm (hereafter [3.6]) Spitzer images and rotation curves from various sources. SPARC contains information on 240 galaxies, including 25 ETGs and, in particular, the three objects chosen in this work.
The SPARC database provides the stellar density profiles and the decomposition of those

[2] D < 42 Mpc, $|\delta - 29°| < 35°, |b| > 15°$

into disk and bulge components, as well as distances to the galaxies determined from the Hubble flow. For our three objects, we compare the latter ones to distance estimates from Cappellari et al. (2011) in Tab. 1.1. While the distances to NGC2824 and UGC6176 in Cappellari et al. (2011) are also estimated from Hubble flow, the one to NGC3626 is determined from surface brightness fluctuations, which explains the larger difference to the SPARC estimate. Although distances estimated by surface brightness fluctuations in general have smaller errors, in this work we decide to use the distance estimates from the SPARC database for consistency, since the difference between the values is within 1 sigma.

1.6.2 The galaxy sample

In this section, we summarize existing information about the three galaxies we investigate in this thesis. We show optical images of the galaxies from the Sloan Digital Sky Survey at 623.1μm in Fig. 1.2. In Tab. 1.1, we summarize their known properties.

NGC2824 is classified as S0, i.e. a lenticular. HI is seen in absorption in the central parts. It hosts nuclear H_2O masers that can be associated with parsec-scale jets or outflows (Zhao et al., 2018).

UGC6176 is characterized as SB0, i.e. a barred lenticular. It is a regular field rotator. In Alatalo et al. (2013) it is marked to have a ring and filaments in CO. Its HI and CO disks are co-rotating and aligned with the stellar disk (Serra et al., 2014). However, in Serra et al. (2012) it is marked to have a warp.

NGC3626 is characterized as (R)SA0ˆ+(rs), i.e. an unbarred lenticular galaxy with structures transitioning to rings (rs) in the inner parts and an outer ring (R). It has a minor spiral structure seen in near-IR, and a series of inner rings in the innermost parts ($R < 5''$) seen in the CO (T. Davis, private communication) and the stellar body (Silchenko et al., 2010). The stellar rings are formed of young stars. Silchenko et al. (2010) find they have ongoing star formation with an average age of 1 Gyr, while the age of the galaxy is estimated to be 11.5 Gyrs (Mazzei et al., 2014). NGC3626 has a companion galaxy with significant HI emission. We remove its emission for all of our analysis.
NGC3626 is an off-center galaxy in the X-ray bright group Leo II. It has been largely investigated as it was one of the first detected galaxies to have a large-scale counter-rotating gas disk (Ciri et al., 1995, Jore et al., 1996). NGC3626 exhibits a complex inner structure both from morphology and from kinematics. Haynes et al., 2000 found a separate gas population co-rotating with the stars in the innermost region of the galaxy ($R < 6''$), which must lie in a different plane than the plane of the galaxy (Silchenko et al., 2010).
Silchenko et al. (2010) found that the galaxy can be modeled by two disks and a compact bulge. They find a projected orthogonal gas disk in the innermost parts of the galaxy ($R < 8''$). This disk is accompanied by higher velocity dispersion in the stellar disk, pointing to the existence of a stellar counterpart, the motion of which is superimposed with the motion of the main stellar population. They also note a strong warp in the inner parts of the galaxy ($R < 500$pc).
Silchenko et al. (2010) offer three possible explanations for the observed features: a recent merger with a dwarf galaxy, the remains of which are observed near the center of NGC3626, an interaction with a companion galaxy that moves in the equatorial plane of NGC3626 in the other direction than its stellar rotation, or interactions with a bar that recently dissolved

	NGC2824	NGC3626	UGC6176
RA (J2000) [hms]	09 19 02.22648	11 20 03.79392	11 07 24.66072
DEC (J2000) [hms]	+26 16 11.9964	+18 21 24.4476	+21 39 25.8660
Morph. type	S0	(R)SA0ˆ+(rs)	SB0
D_{SPARC} [Mpc]	39.6	22.9	39.3
D_{ATLAS} [Mpc]	40.7	19.5	40.1
M_K [mag]	−22.87	−23.65	−22.56
$\log M_{HI}/M_\odot$	7.19	12.32	8.66
$\log M_{H_2}/M_\odot$	8.43	11.47	8.41
L[3.6] [$10^9 L_\odot$]	39.6	74.6	29.0
R_{eff} [kpc]	1.09	2.43	1.18
Σ_{eff} [$L_\odot/pc^2$]	5209.91	2017.58	3317.65

Table 1.1: Information on the galaxy sample. The galactic centre coordinates are from Cappellari et al. (2011). We show the distances determined in Cappellari et al. (2011) and Lelli et al. (2016). For this thesis, we adopt the distances from the SPARC database. M_K, the total galaxy absolute magnitude (corrected for the foreground galactic extinction), and the total masses of atomic and molecular hydrogen are from Cappellari et al. (2011), Serra et al. (2012) and Alatalo et al. (2013), respectively, and converted to distances from Lelli et al. (2016). L[3.6], the total galaxy luminosity from Spitzer [3.6], R_{eff}, the effective radius encompassing half the total luminosity and Σ_{eff}, the associated surface brightness of the galaxies, are from from Lelli et al. (2016).

or nearly dissolved. The second possibility is interesting, since NGC3626 has a companion galaxy, but not further discussed in the literature. Chemo-photometric smooth particle hydrodynamical simulations by Mazzei et al. (2014) favour the merger scenario.

1.6.3 Outline

The thesis is structured as follows: in chapter 2, we derive the moment maps and velocity fields for our galaxies, which we use in chapter 3 to derive the rotation curves. We proceed by modeling the galaxies and calculating the rotation curves predicted by the visible mass distribution. We compare these predictions to the measured rotation curves in chapter 4. Finally, in chapter 5 we fit four dark matter profiles to our rotation curves and analyse our results in the context of the ΛCDM theory. We summarize our work and provide a brief outlook in chapter 6.

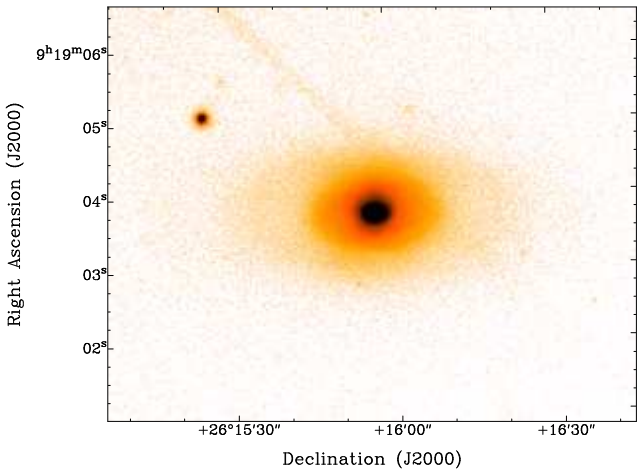

(a) NGC2824

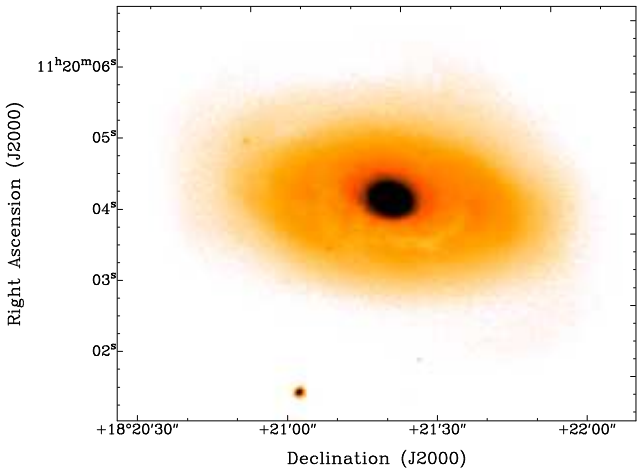

(b) NGC3626

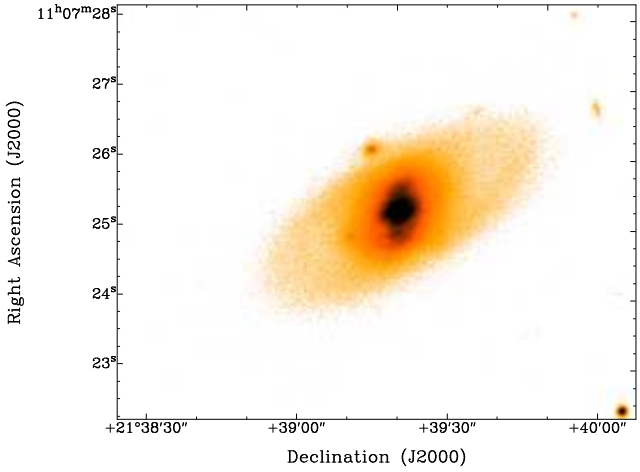

(c) UGC6176

Figure 1.2: SDSS images (in the red filter) of our three galaxies. Please note that these images are rotated by 90 degrees with respect to all other images in this thesis, having the right ascension along the y axis.

Chapter 2

Analysis of data cubes

In this chapter, we explain the methods and procedures to work with the observed data. We derive several parameters and maps of our galaxies that are used for a deeper scientific analysis in the following chapters.

2.1 Radio and millimetre/sub-millimetre observations

As explained in section 1.5, HI emits at radio wavelengths, while CO emits in the sub-millimetre range. The angular resolution θ of a telescope with one antenna dish is given by

$$\theta = 1.22 \, \frac{\lambda}{D} \tag{2.1}$$

where the wavelength λ and the dish diameter D are in meters and θ is in radians.
This shows that the angular resolution is limited by the physical size of the telescope, which cannot be arbitrarily large. For example, for HI obsevations at 21 cm, a single-dish telescope with a diameter of 100m would give an angular resolution of ca. 15 degrees, which is not sufficient to resolve the distribution and kinematics of galaxies outside the Local Group. To increase the resolution of observations, one makes use of interferometry.
In interferometry, one source is observed by multiple antennas located at different positions, a so-called array. The distances from the source to the individual antennas differ, so between each two measured light rays there is a difference in phase and amplitude, which gets recorded. The observations of all antennas are combined to create the interferometric image of the source. The resolution of this image is limited by two values: the smallest scale that can be resolved is given by the largest distance between two antennas. However, the bigger the distance between two antennas, the smaller the structures that can be observed, i.e. the large scale diffuse emission cannot be detected (see, e.g., Jackson, 2008).
Interferometric observations measure the Fourier components of the physical image (so-called visibilities). The image is then obtained by a Fourier transformation of these. The quality of the physical image depends on how well the uv-plane (which is the Fourier equivalent of the xy-plane) is sampled. The measurement is typically performed in frequency bins that cover the range of frequencies in which the source emits. The Fourier transformation is performed for each frequency bin.

2.2 Data cubes

Radio and mm/submm interferometry, as well as integral-field spectroscopy (IFS), provide so-called datacubes. These have right ascension and declination along the x and y axes and velocity (or frequency) along the z axis.
In general, datacubes contain not only line emission, but also continuum emission. In the case of radio observations, the continuum emission comes from synchrotron radiation. Since we are interested in gas emission lines, the continuum is estimated in line-free channels and subtracted from the datacube. Hence, scrolling through the continuum-subtracted cube along the z axis, one sees gas moving with a specific velocity, as projected along the line of sight. For the HI, we use datacubes that have been reduced and continuum-subtracted by the ATLAS^{3D} collaboration (Serra et al., 2012). For the CO, no continuum subtraction was performed, as there is nearly no continuum emission in the relevant frequency range (Alatalo et al., 2013).
Compressing the data cube along the velocity axis shows areas that emit at all observed frequencies, resulting in an intensity map. Maps of other quantities can be derived by compressing the data cube, as described below. This way, the dimensionality of the data can be reduced, facilitating the analysis process. One must note, however, that in this process some information is bound to be lost.
Another way of getting 2D information out of the data cube is by taking slices of it along a given direction in the (RA, DEC) plane. The resulting dependency of velocity on position can be plotted in so-called position-velocity diagrams. Typically, one takes slices along the

major or the minor axis of the galaxy, so one can visualize the dependency of the velocity on position along that axis.

2.3 Masking

The data contains noise, which we want to minimize when building moment maps. The noise can be distinguished from real signal as it is of the order of the size of the beam and does not appear in adjoining velocity frames. There are two main methods to analyze only the physical emission. One could perform sigma-clipping to remove all emission fainter than a particular value. Unfortunately, this also removes signal that is faint, but adjoining to brighter regions and continuous in velocity, e.g., signal at the edges of the galaxy. Therefore, this method is not preferable.
The alternative is masking the data cube. In this case, one creates and applies a mask that, in each velocity frame, identifies the region of emission. For all further operations, one can then use only the regions inside the mask. To create such a mask, the cube is smoothed in space and velocity. In the process of the smoothing, the signal is averaged over bigger areas, resulting in the physical signal being boosted and the noise going down, as positive and negative noise regions get averaged. Estimating the noise of the smoothed cube and applying sigma-clipping now, one will remove less of the physical emission than when applying sigma-clipping directly to the full resolution cube. Setting regions above the sigma-clipping threshold to 1 and those below to 0, one gets a Boolean mask cube with continuous 3D regions that show where the emission is located in the initial data cube. Now, one can apply this mask to the data cube at full resolution, working only with the signal inside the mask. After the masking process, there may be some noise left, but these noisy regions are small enough to be neglected in the analysis. The degree of smoothing required to create a good mask is cube-dependent.
For many computational tasks in this thesis, we have used the *gipsy* software (the Groeningen Image Processing System), which was developed continuously starting from the 1980s by R.J. Allen, K. Begeman, M. Voogelar and other staff members and students of the University of Groeningen[1]. It is a package for image processing which is specifically targeted to work with datacubes and deriving rotation curves. We determine the average noise in the cubes with the *gipsy* task *stat* selecting channels that are free of line emission. Then, the cubes are being smoothed in space and velocity with the *gipsy* tasks *smooth* and *velsmo*.
The velocity smoothing redistributes the signal among the channels such that 0.5 of the signal stays in the initial channel and 0.25 of it is shifted to the two adjacent channels. This weighting scheme is called Hanning smoothing.
In the smoothed cubes, the noise is determined again and sigma-clipping to a 3 sigma level is performed with the *gipsy* task *combin*. The resulting masks are visually expected and the grade of the smoothing is increased until the results are satisfactory. The properties of the full-resolution and smoothed cubes are provided in Tab. 2.1.
The masks are applied to the cubes with the *gipsy* task *combin*.

2.4 Moment maps

As mentioned above, summing the emission from the cube along the velocity axis gives a flux density map of the observed galaxy. This map is also referred to as the moment-0 map. We create intensity maps using the *gipsy* task *moments* with option 0, i.e. summing up

[1] `https://www.astro.rug.nl/~gipsy/`

all channels without weighting. For HI, the flux can be uniquely related to the density of the emitting gas, while for CO one has to relate the amount of the latter to a H_2 column density, as described in subsection 1.5.2.
Getting a map of the line-of-sight velocities is more tricky, since this procedure is not unique. At each position (x,y), the profile of the emission line, i.e., the dependence of intensity on the frequency, is measured. This profile has a finite width and usually one peak value, although there might be several peaks if there are multiple sources emitting along the line-of-sight. The profile is not always symmetric. Estimating the line-of-sight velocity at a particular position of the sky means characterizing the line profile with a single value. There are several sensible possibilities for the choice of this value leading to slightly different velocity estimates (see also de Blok, 2008).

Peak value. The value of the velocity at the peak emission along the line profile is a choice that is independent of further assumptions about the shape of the profile. However, it gets easily biased for small S/N levels. Therefore, the velocity estimation with this method may be unreliable at the edges of the emitting regions.

Intensity weighted mean value The choice of the intensity-weighted mean value is very sensitive to asymmetries in the line profile such as broad wings on one side, which would give values far from the peak value. This estimate is also easily biased if the noise is not properly removed. Traditionally, maps created with this estimate would be referred to as moment 1 maps. In this work we will use this term also for maps created with other velocity estimates.

Single Gaussian fit. Fitting a Gaussian to the line profile and choosing its central value is a more stable estimate of the adopted velocity, although it also is subject to asymmetries in the line profile.

Multiple Gaussians. To better describe the profile shape, one might fit multiple Gaussians to the line. This way, one can disentangle separate components of the measured velocity, such as those coming from the main galaxy rotation, non-circular motions etc. One would typically fit a number of Gaussians simultaneously. To reduce the degeneracies in the parameters, one might also fit a Gaussian, subtract this from the line profile and fit another Gaussian to the remaining signal.

Gauss-Hermite polynomial fit. Fitting a Gauss-Hermite polynomial that has a h_3-term (skewness) accounts for possible asymmetries in the line profile.

In this work, we use two different methods. On one hand, we use *moments* with option 1, which is defining the intensity-weighted mean velocity in the masked cube. On the other hand, we construct the velocity fields using the central value of a single Gaussian fit using the task *xgaufit*. For each galaxy and tracer gas, the same velocity field is used for all analytical tasks. Which of the methods was chosen is galaxy-specific depending on the quality and S/N of the cubes.

One can also construct higher order moment maps, but their physical meaning gets more obscured and depends substantially on the quality of the data. The moment 2 map, which measures the broadening of the profile line can be used to characterize the gas velocity dispersion. However, the construction of this map is a delicate procedure. For data with low signal-to-noise the peak in the line profile might be only a little above noise level, so its width is hard to quantify. The resulting maps might turn out strongly biased by the noise. A more serious concern is beam smearing, as we discuss in the following paragraph. We do

not construct moment 2 maps for our data.

An important effect in the construction of moment maps is known as beam smearing. The signal that is measured within one beam gets averaged. This is very important in areas with high intensity or velocity gradients. If the characteristic gradient scale length is comparable with the beam size, the gradient will appear shallower in the observation. Beam smearing generally leads to an underestimation of the observable. The line profiles in these areas will get broadened and asymmetric, so also higher order moment maps will be biased. In particular, the moment-2 map (velocity dispersion) will be systematically over-estimated since most of the line broadening is not physical but driven by the low spatial resolution. The beam smearing is especially significant near the galactic center, where the velocity growths steeply. If not accounted for, it may lead to crucial underestimates of the rotation curve.

2.5 Estimating the noise in moment-zero maps

When a mask is used to construct a moment zero map, a special caveat is that the usual definition of the noise for N channels ($\sqrt{N}$ times the average noise) can no longer be used for the final maps. This is because a different number of channels is summed at each position (x,y) due to the masking process. Moreover, if the cube was continuum subtracted, the subtraction increases the noise in each channel. This is not a problem for defining the noise value in each channel, but has to be accounted for when calculating the noise for a sum of the channels.
It is therefore useful to introduce an alternative measure of the noise: the pseudo 3 sigma noise level. The derivation of the pseudo sigma value consists of two steps. First, we take into account effects coming from continuum subtraction and possible velocity smoothing of the data in the cubes. The derivation of the corresponding $\sigma^{\rm cor}$ values can be found in the appendices of Verheijen & Sancisi (2001) and Lelli et al. (2014), depending on the form of the correlated noise in the data.
In our case, the cubes are Hanning smoothed, so adjacent channels are not independent any more. Therefore, we use the formula from the appendix of Verheijen & Sancisi (2001), namely

$$\sigma_N^{\rm cor}(x,y) = \sqrt{N(x,y) - 0.75 + N^2(x,y)A^2} \cdot \frac{4}{\sqrt{6}}\sigma_0, \tag{2.2}$$

where σ_0 is the noise, N is the number of channels with signal at each position (x,y), $\sigma_N^{\rm cor}$ is the value of sigma corrected for continuum subtraction, and A is depending on the way the continuum is subtracted in each data cube.
For the HI data of NGC2824 and UGC6176, A is given by

$$A = \frac{1}{2} \cdot \sqrt{\frac{N_l - 0.75}{N_l^2} + \frac{N_h - 0.75}{N_h^2}}, \tag{2.3}$$

where N_l and N_h are the number of channels used for estimating the continuum at the low and high velocity ends of the data cube, respectively.
For the HI data of NGC3626, additional channels in the middle of the velocity range of the data cube were used to model the continuum, so a further term $(N_m - 0.75)/N_m^2$ has to be added under the square root in eq. 2.3, as well as the factor in front of the root changed from 1/2 to 1/3.
For the CO cubes, no continuum subtraction was performed, so A can be set to 0.
As the next step to estimate the pseudo sigma value, for each galaxy and tracer, we construct

a signal-to-noise map using the intensity map and the sigma value from eq. 2.3. Then, a pseudo 3 sigma value is estimated as the average intensity in the region that has a value between 2.75 and 3.25 in this signal-to-noise map. This mean intensity is what we define to be roughly $3\sigma_{pseudo}$. This way we account for the different number of summed channels in each pixel. This value is used to plot the contours in all moment-zero maps.

2.6 Results

In Figs. 2.1 to 2.3, we present the intensity and velocity maps for our galaxy sample. We also show optical images taken with Palomar Observatory's 48-inch Samuel Oschin (Schmidt) Telescope at 645 μm. In the upper row of each figure, we show HI moment maps, while in the lower row, we show a zoom into the CO region in the optical image together with the CO moment maps.
From the intensity maps, one can see that the HI distribution is more extended than the stellar body for all three galaxies, while the CO distribution is concentrated near the galactic center. The HI intensity map shows that NGC2824 and NGC3626 are strongly inclined. In the HI intensity map of NGC3626, a ring feature of higher density can be seen, in agreement with previous results outlined in chapter 1.6.2. The NGC2824 HI intensity map shows an off-center over-density.
The velocity fields display regular rotation.
On large scales, the morphological position angle in the emission line maps agrees with the kinematic PA from the velocity maps. It also agrees with the orientation of the stellar bodies for NGC2824 and UGC6176. For NGC3626, the PA suggested by the elongation of the stellar disk differs from the average HI position angle, being a possible indication of a warp.
In the lower left corner of each map, the size of the beam is shown. The emission that lies within one beam size gets averaged, so features smaller than the beam cannot be resolved. On these scales, there might be beam smearing effects. We will quantify them in the next chapter.

Galaxy	Line	Velocity res. [km/s]	Angular res. [arcsec^2]	PA_{beam} [°]	σ [Jy/beam]	smoothing grade in space [arcsec]	smoothing grade in velocity [times]	σ_{pseudo} [Jy/beam]
NGC2824	CO	25	4.28 x 4.00	-27.24	0.01019	8 x 8	1x	0.0265
	HI	8.245	28.6 x 12.9	0.5	0.00015	60 x 60	2x	0.0007
NGC3626	CO	25	3.95 x 3.68	4.67	0.00053	10 x 10	1x	0.0101
	HI	8.245	59.36 x 32.38	5.15	0.00054	180 x 90	2x	0.0038
UGC6176	CO	15	3.54 x 2.81	89.01	0.01071	6 x 6	1x	0.0302
	HI	8.245	51.48 x 33.33	5.39	0.00053	150 x 150	1x	0.0067

Table 2.1: Parameters of the data cubes together with the smoothing grades used for creating the masks and the estimated noise values. Note the higher σ values for the CO cubes of NGC2824 and UGC6176.

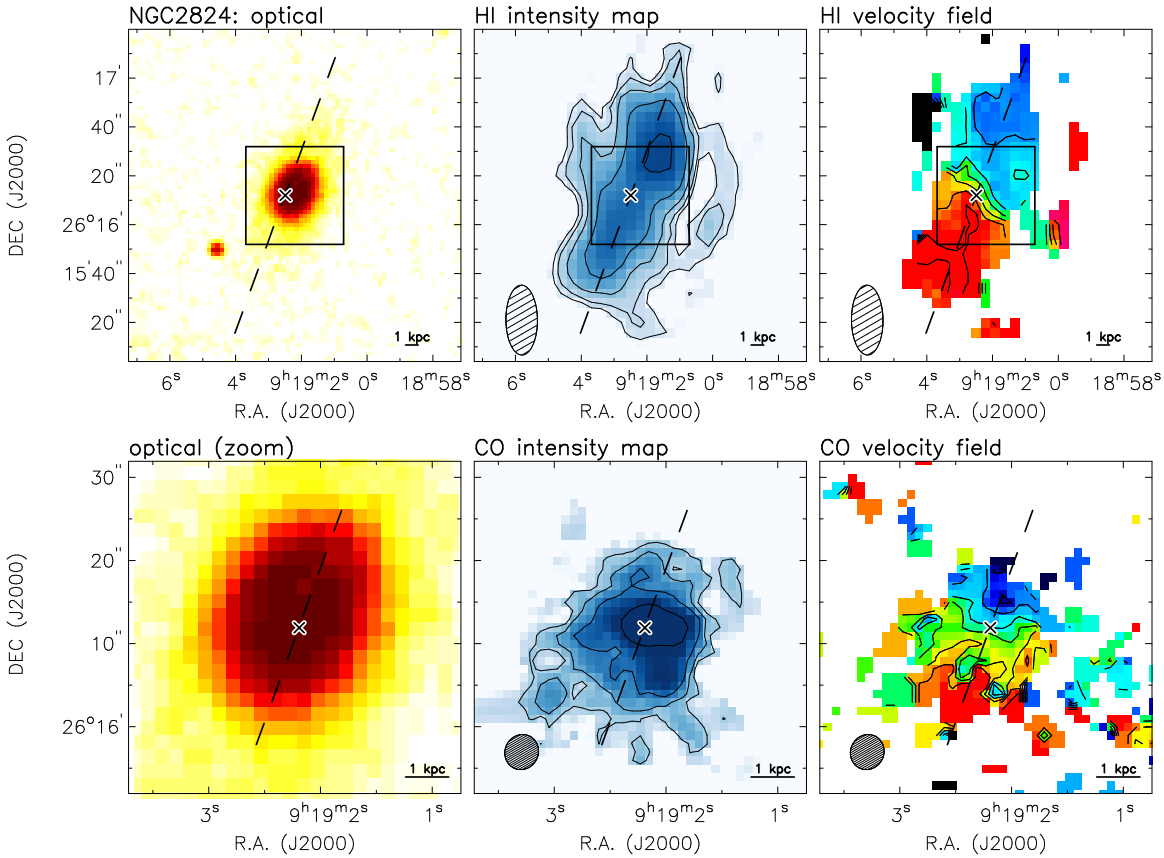

Figure 2.1: Optical image, intensity maps and velocity fields for NGC2824. In the top panels, we show the optical image (left), the HI intensity map (middle) and the HI velocity field (right). In the bottom panels, we show a zoom-in of the optical image (left), the CO intensity map (middle) and the CO velocity field (right). The intensity map contours correspond to multiples of $3\sigma_{\rm pseudo}$. Contour levels in the velocity fields are chosen for optimal visualization. The black box in the top panels shows the sky region in the bottom panels. The HI and CO beams are shown in the bottom-left corner of each panel. The physical scale for the assumed galaxy distance is shown in the bottom-right corner.

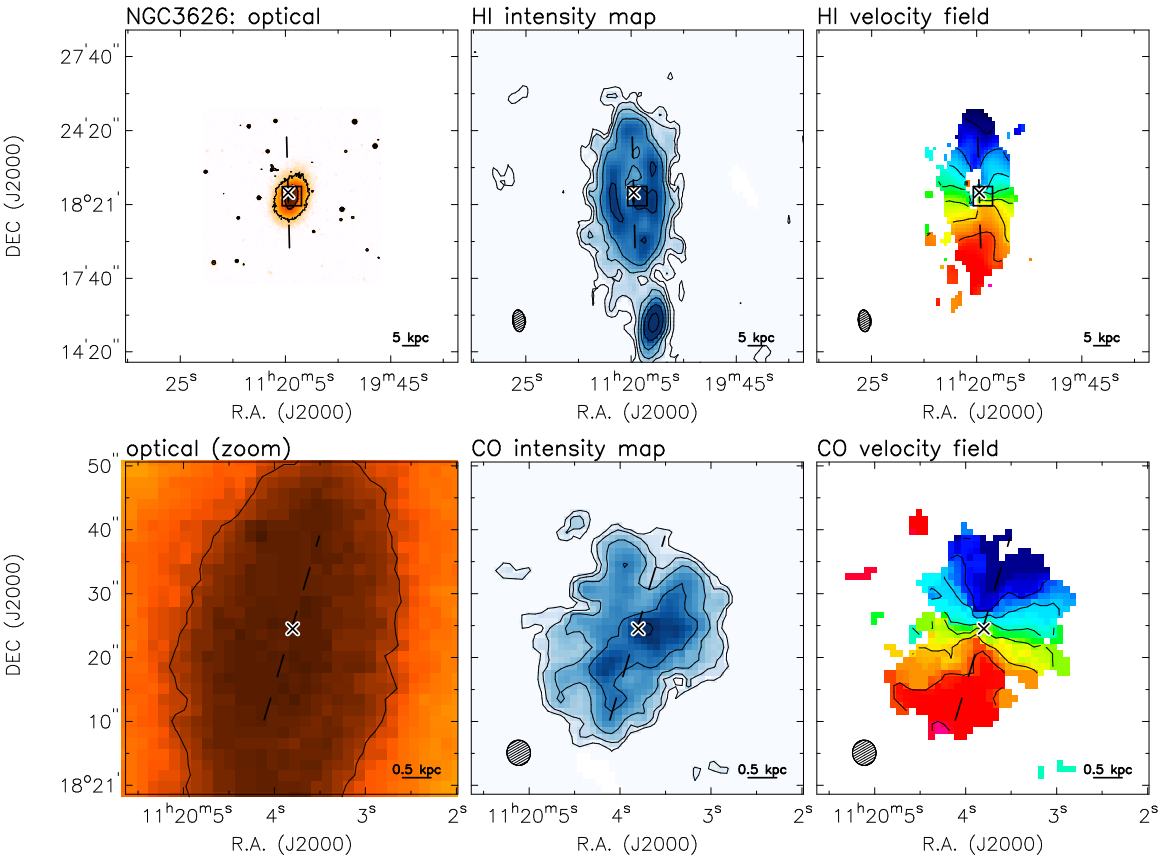

Figure 2.2: Same as Fig. 2.1, but for NGC3626.

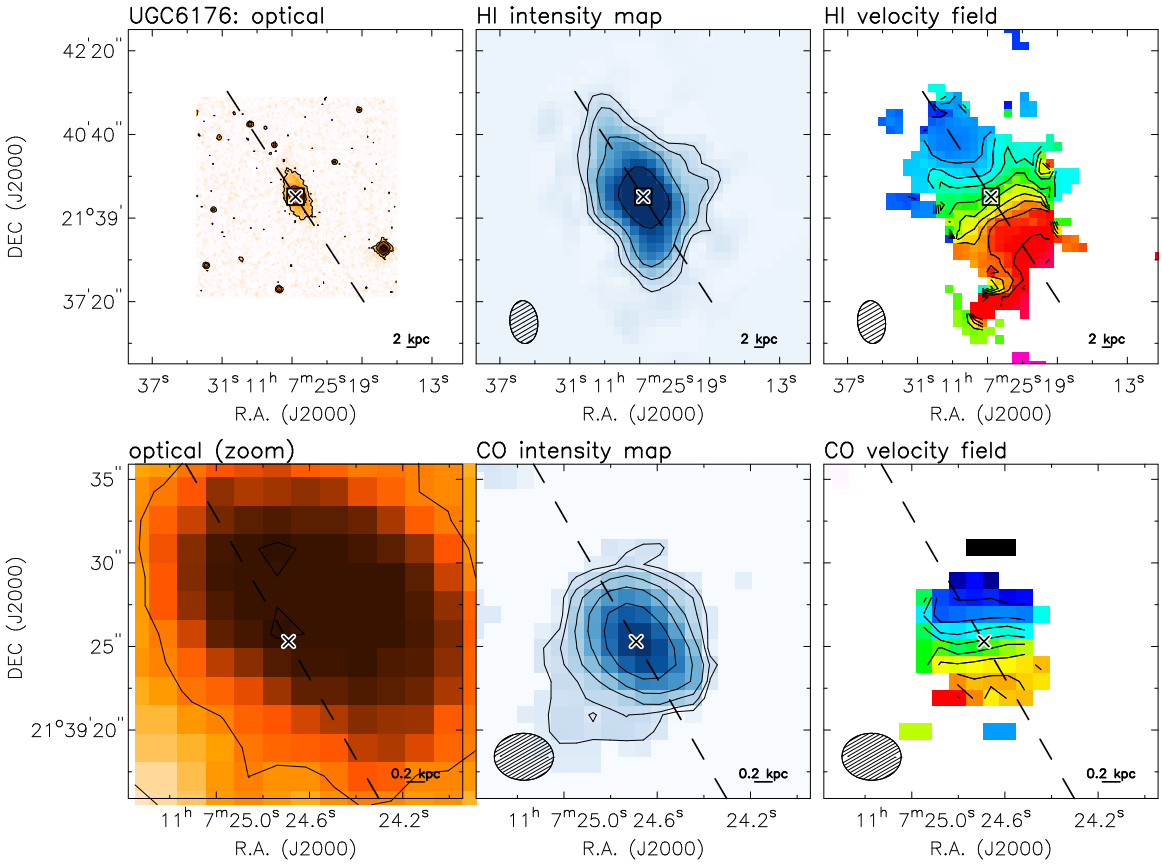

Figure 2.3: Same as Fig. 2.1, but for UGC6176.

Chapter 3

Rotation curves

In this chapter, we describe how rotation curves can be derived from the data and present the results for our sample. We use two different methods to derive the rotation curves and show that they provide consistent results.

3.1 Tilted-ring modeling

Galaxy disks have random orientations on the sky. The tilt of the disk plane with respect to the sky plane can be characterized by two angles: the position angle (PA) and the inclination angle (i). The inclination measures the angle between the normal vector to the plane of the gas disk and the line of sight, while the position angle specifies the orientation of the major axis in the plane of the sky. Conventionally, it is defined as the angle taken anti-clockwise between the Northern direction on the sky and the major axis of the galaxy.
The projection of the rotation velocity on the line of sight depends on both PA and i. Assuming that the gas disk is infinitely thin and purely rotating (i.e., exhibits no strong non-circular motions), the observed velocity at a radius R is given by

$$v(x,y) = v_{\rm sys} + v_{\rm rot}(R)\sin(i)\cos(\phi) + v_{\rm rad}(R)\sin(i)\sin(\phi), \tag{3.1}$$

where ϕ is the azimuthal angle in the plane of the galaxy and depends on the position angle in the following fashion:

$$\begin{aligned}\cos(\phi) &= \frac{1}{R}(-(x-x_0)\sin(\mathrm{PA}) + (y-y_0)\cos(\mathrm{PA})) \\ \sin(\phi) &= \frac{1}{R\cos i}(-(x-x_0)\cos(\mathrm{PA}) - (y-y_0)\sin(\mathrm{PA})).\end{aligned} \tag{3.2}$$

Here, (x_0, y_0) denotes the position of the centre of the galaxy. It has to be stressed that eqn. 3.1 is the first term in the harmonic expansion of a general velocity field. Hence, it can only be used when non-circular or random motions are negligible compared to the rotation velocity.
It is obvious from eqn. 3.1 that the projection of the rotation velocity along the line of sight is maximal at the major axis of the galaxy and null along the minor axis. Indeed, at the major axis the rotation velocity is perpendicular to the plane of the sky. On the other hand, at the minor axis the rotational velocity component is entirely on the plane of the sky. Here, one can directly measure the systemic velocity of the galaxy, given by the sum of the recession velocity (from cosmological redshift) and the galaxy peculiar velocity.
Therefore, to derive the rotation curves of galaxies, we have to choose objects with an inclination that is neither too big nor too small. For a face-on galaxy one would only measure its systemic velocity. Meanwhile, for an edge-on galaxy the emission of different parts of the galaxy moving at different speeds is projected at the same position on the sky and require a different approach to be disentangled. This is called the envelope tracing method (e.g. Gentile et al., 2004, Fratenali et al., 2011), and goes beyond the scope of this thesis.

To determine the rotation curve of the galaxy, we need to fit eqn. 3.1 to the observed velocity field. For this, one divides the galaxy into rings, that become ellipses when convolved with i and PA to reproduce the visible orientation of the galaxy on the sky. The widths of the rings are commonly set to be equal and roughly equivalent to the spatial resolution of the data. For each ring, one can determine centre, inclination, position angle, and the systemic and rotation velocities by a χ^2 fit of eqn. 3.1 to the observations. Given the large number of free parameters, the fit is performed in several iterations, fixing the parameters one by one until only the rotation velocity is the only remaining variable (a more detailed discussion of this procedure is provided in section 3.2).
The galactic centre and the position angle of the galaxy can be double checked with the optical observations of the galaxy. Also, first estimates can be provided from inspecting the density maps. Another easy-to-estimate parameter is the systemic velocity. As the rotation velocity points perpendicular to the line of sight at the minor axis, the observed velocity

must be equal to the systemic one.
The inclination and position angle might vary with radius, which would suggest that the disk is warped. For each galaxy, it has to be decided whether a warp is present and should be modelled, or whether the angles should be kept fixed for all radii.

3.2 Deriving the rotation curves

In this work, we use two methods to determine the rotation curves. On one hand, we perform the traditional analysis, using 2D maps and the *gipsy* task *rotcur* to derive the rotation curves. Then, we use these rotation cuvres as inputs to construct 3D kinematical models with the task *galmod*. On the other hand, we use the program ^{3D}Barolo that determines the rotation curve fitting the entire datacube and using a full 3D approach.

3.2.1 Deriving the rotation curve with *rotcur*

To derive the rotation curves from moment maps, we use the *gipsy* task *rotcur*. It performs the tilted ring fit, as described in section 3.1, provided a velocity map. The user should also provide first estimates for the systemic velocity, galaxy center, position angle and inclination, as well as v_{exp}, a parameter that describes radial motions within the galaxy plane, which we set to zero.

We summarize our parameter choices in table 3.2. The inital guesses for the systemic velocity, galactic center and PA are estimated by visual inspection of the cube (with *karma*'s *kvis* and *gipsy*'s *sliceview*) and cross-checked with values provided by Serra et al. (2012), Alatalo et al. (2013) and on the NASA NED website. The width of the rings is chosen to be either equal to the width of the beam major axis or $\sqrt{(b_{\rm maj} \cdot b_{\rm min})}$, if the beam is strongly elongated and not aligned with the PA of the galaxy. Here, $b_{\rm maj}$ and $b_{\rm min}$ are the major and minor axes of the beam, respectively. The number of the rings is determined such that the major axis of the galaxy is fully covered. In all cases, we simultaneously fit both halves of the galaxy, neglecting possible asymmetries between the different sides as they cannot be investigated at the given resolution. The pixels in the velocity maps are weighted using a cosine function in order to give more weight to points close to the major axis, which provide most information regarding the rotation velocity.
We perform a series of iterations, keeping $v_{\rm sys}$, x_0, y_0, i, PA and $v_{\rm rot}$ free in the first one and fixing $v_{\rm sys}$, x_0 and y_0 to the retrieved values in the second one. In the next two iterations, the inclination and position angle get fixed to the values estimated by the code in arbitrary order. We have verified that the order does not change the resulting rotation curve within error bars. The last run of *rotcur* is performed having only $v_{\rm rot}$ as a free parameter.

3.2.2 Checking the rotation curve with *galmod*

The procedure described in section 3.1 depends on 5 parameters that might be degenerate. The latter is especially true for i and $v_{\rm rot}(R)$ as they enter into equation 3.1 as a direct product. On the other hand, as mentioned in section 2.6, the beam smearing flattens out velocity gradients in the observed velocity field and always leads to an underestimation of the rotation velocity, especially in the innermost parts of the galaxy. Hence, one needs to double check if the determined parameters are correct, i.e., if a mock galaxy constructed with these parameters reproduces the observations.

In this section we describe how to construct 3D model using the derived rotation curve and a density distribution mimicking the observations.

Deriving the density distribution

To construct a model cube that reproduces the observations as closely as it is possible, we need information not only on the kinematics of the gas, but also on its density distribution. We derive the latter from the intensity map, using the *gipsy* task *ellint*. This task divides the galaxy into rings (of provided radii and widths) and calculates the mean intensities or surface brightnesses (depending on settings) for each ring, averaged over the area of either the ring or all non-blank pixels in the ring. The task returns also face-on flux values, corrected for the galaxy inclination. We use the task with option 2, calculating the mean surface brightness averaged over the total area.
From the latter, we can retrieve the mass surface density of the HI using the known relationship

$$N_H = \frac{1.25}{1.13} \cdot 10^{24} \cdot I_{\text{total}} \Delta v \cdot \frac{A_{\text{pix}}}{x_{\text{beam}}\ y_{\text{beam}}}. \tag{3.3}$$

Here, A_{pix} is the area of the pixel. Regarding the H_2, its flux density is determined from the one of CO as described in subsection 1.5.2 with

$$N_{H_2} = X_{\text{CO}} \cdot I_{\text{CO}}(J = 1 \rightarrow 0). \tag{3.4}$$

We adopt the value of $X_{\text{CO}} = 2 \cdot 10^{20} \text{cm}^{-2} (\text{K km s}^{-1})^{-1}$ following Bolatto et al. (2013).

Constructing a model cube

Now we can proceed to create model cubes using the task *galmod*. This task creates a 3D mock galaxy from a user supplied density distribution and rotation curve. It is assumed that the galaxy is axis-symmetric. The task divides the galaxy into rings and populates them with gas clouds. Within each ring, the algorithm chooses the azimuthal angle and the rotation radius of the clouds randomly in a way to make the distribution in the galactic plane uniform. The height of the clouds is drawn from a probability distribution proportional to the chosen function for the vertical density distribution. The clouds are assigned velocities calculated from the systemic velocity and the rotational velocity at the given radius with a provided velocity dispersion. The resulting model is projected on the sky for the given center, v_{sys}, PA and i. Later, it is convolved with the observational beam.
For the CO cubes, *galmod* is not applicable, because it is converting the supplied surface density into the observed surface brightness in Jy/beam assuming HI emission. This conversion is frequency dependent. There is no analogue for the CO. We use a variation of *galmod* developed by F. Lelli, *galmodvert*, which performs the same operations as *galmod*, but independently of the frequency of the input data. However, as a simple conversion relation from H_2 surface density to CO surface brightness does not exist, the resulting model has arbitrary units. Therefore, we renormalize the total flux of the model cube to be equal to the one of the original cube to get sensible results.
To compare the model with the data, one creates moment maps. The comparison can be performed visually or by subtracting the maps from one another and plotting the residuals. The better the model is, the smaller the residuals will be.
As the maps probe only the similarity between the 2D compressions of the data cubes, we also construct position-velocity diagrams to see whether the inner 3D structure of the model cube reproduces the observations. For this, we take slices through the cubes along the major and minor axes. Like for the maps, we examine both the visual agreement of the PVs and

their residuals.

A disagreement between the data and the model indicates that the inputs for the modeling were not accurate enough. Typically this is an effect of beam smearing on the input rotation curve or the input surface density profile that can be corrected manually. If the intensity maps do not agree, the central part of the density distribution might need an adjustment. As beam smearing always flattens and lowers the profile, the innermost points can be placed a little higher until a good agreement is achieved.
Once the intensity maps agree, any discrepancy in the PVs comes from beam smearing effects on the rotation curves. Also here beam smearing will always result in an underestimation of the velocity. The rotation curve points are adjusted manually (especially in the innermost regions) until the residuals between the model and the data get as small as possible.

3.2.3 Deriving the rotation curve with ^{3D}Barolo

As mentioned in subsection 2.2, when the analysis is performed using moment maps, some information that is contained in the originally three dimensional data-cubes is lost. Additionally, biases are induced by the intermediate steps of moment map creation. These come from the dependence of the derived velocity field on the ambiguous definition of the velocity value, as described in subsection 2.4, as well as problems arising when the line profile at some given position has two peaks, which may happen if the galaxy displays complex kinematics like non-circular motions, inflows or outflows, so the emission of two components at different velocities is measured.
It is therefore clearly favourable to use methods that analyze the entire data cube without reducing its dimension as described in section 2.4. Programs to do so have been recently developed. Since there exist no analytic three dimensional fitting procedures, these programs rely on Monte Carlo simulations. Model data cubes are created and compared to the original one, until the χ^2 between the observed cube and the model cube is minimized. This is similar to what we have interactively done with *galmod*, but it is performed in an automatic fashion by a fitting algorithm. Although computationally intensive, this procedure allows to model asymmetries in the line profiles that might be lost in creating the velocity map, avoids the above mentioned problems with velocity extraction and, last but not least, does not suffer from beam smearing since the model cubes are convolved with the instrumental resolution.
Programs that perform 3D fits are naturally very sensitive to the quality of the input data. In this work, we use ^{3D}Barolo (Di Teodoro & Fratenalli, 2015), as this program is specifically developed to work with low resolution cubes.
This program performs a 3D fit on a ring by ring basis, using the tilted ring model, until a good fit is achieved. The simulation happens in six dimensions (space and velocity), and gets projected into the 3D space of a data cube (two spatial and one velocity dimensions), convolving the model with the beam as in the observations. The surface density of the model is normalized to reproduce the one of the observations.
The user can supply initial guesses for the parameters either globally or on a ring by ring basis, and can also fix parameters during the fit, similar to working with *rotcur*.
For our galaxies, we ran ^{3D}Barolo iteratively, fixing first the position of the center of the galaxy and the systemic velocity, then the velocity dispersion of the gas, position angle and inclination (in varying order depending on the case), finally leaving only the rotation velocity as a free parameter. We have checked that the order in which the parameters are fixed does not alter the final rotation curve within the errors.

We also use ^{3D}Barolo to estimate the uncertainty on each of the free parameters. For that, we run the code with all parameters (including the rotation velocity) fixed to the final estimated value and only the parameter of interest left free.
The errors on the rotation velocity and the inclination can be simply propagated into a total error on $v_{\rm rot}$. Errors on the other parameters cannot be easily propagated, but rather systematically change the result. For example, if the position angle was estimated wrongly, it would lead to a systematically under-estimated rotation curve, as the latter would have not been estimated along the major axis. So this error cannot be accounted for merely by Gaussian error propagation.
We calculate the error on $v_{\rm rot}$ as

$$\Delta v_{\rm rot} = \sqrt{(\Delta v_{\rm Barolo})^2 + \left(v_{\rm Barolo} \cdot \frac{\Delta i_{\rm Barolo}}{\tan(< i_{\rm Barolo} >)}\right)^2}, \tag{3.5}$$

where $v_{\rm Barolo}$ is the rotation velocity estimated by ^{3D}Barolo and $< i_{\rm Barolo} >$ is the mean value of the inclination estimated by ^{3D}Barolo for the different radii.
As for the errors on the other parameters, we find that they are small, so our estimates are trustworthy.

3.3 Results

In this section, we present the rotation curves we derived for our galaxy sample. The manual rotation curves estimates agrees well with the ones from ^{3D}Barolo, but occasionally fit the data a little better, so these are our fiducial ones. We compare the two methods in section 3.3.4.

3.3.1 NGC2824

In Figs. 3.1 and 3.2, we show our results for the CO and the HI emission of NGC2824, respectively. The figures are structured in a uniform way. In the top panel, we present the intensity maps of the observed and modeled cubes together with the residual map calculated by subtracting them from one another. In the two bottom panels, we show the position-velocity diagrams taken along the major and the minor axes. Again, the left column shows the data, the middle one shows the model, and the right one displays the residual. In the major axis PVs, we project the rotation curve we have derived accounting for the best-fit inclination. We also show the outermost contour of the model PV in blue over the observed PV to facilitate the comparison.
For the HI, the agreement between data and model is quite good, although the model slightly overpredicts the density along the major axis. In the HI data, negative signal can be seen in the center of the galaxy, associated with HI absorption, which our model cannot reproduce. The residual intensity maps show no regular structures. The over-density in the northern part of the HI distribution cannot be reproduced by the axisymmetric model.
For the CO, the measured PV diagrams display asymmetries. Specifically, the two halves of the PV along the major axis have different extensions, making them hard to model. We decide to put more trust to the receding half of the galaxy due to the small clump (reproduced by our rotation curve) at the corresponding position in the approaching half. Due to the small amount of rings available for the fit, the model is the best representation we could achieve.
A comparison of individual channel maps from the observed cube and the model cube is presented for the CO in Fig. 3.3 and for the HI in Fig. 3.4. In red, we overplot a contour

R [kpc]	v [km/s]	δv [km/s]	Σ [$M_\odot/pc^2$]
0.38	140.	29	105.1
1.15	194	29	59.48
1.91	211	29	28.91
0.96	160	10	1.30
2.88	160.	13	1.35
4.80	160.	11	1.25
6.72	160.	8	0.98
8.64	160.	10	0.55

Table 3.1: Rotation curve and density profile of NG2824. Top section: H_2, bottom section: HI.

of the optical image, giving an idea of the extent of the gas compared to the stellar body of the galaxy. The data is plotted in grey, the model in blue. Again, it can be seen that the model cannot reproduce the asymmetric features and absorption features around the galactic center that are visible in the HI data. However, the overall agreement is quite good for both for the HI and the CO data.

3.3.2 NGC3626

Our results for the HI and the CO of NGC3626 are presented in the Figs. 3.5 and 3.6. The figures are structured as for NGC2824.
The HI residual map shows that our model reproduces the data well except for the ring feature at approx. 3 arcminutes. In the CO, the intensity residual map shows no peculiarities. The rotation curve traced by HI shows a prominent dip. Since the the dip is seen on both sides in the observed PV diagram along the major axis, we think it is a physical feature (not, i.e., an effect of non-circular motion). Apart from some asymmetry, the minor axis PV is also reproduced well in the HI.
The CO observations unfortunately did not cover all the frequency range of galaxy emission, as can be seen in the sharp cut of the PVs at low velocities. Since *rotcur* cannot take this into account, we adjust the rotation curve points by hand to reproduce the receding part of the PV. It can be seen that this rotation curve also reproduces the approaching half, including the non-measured part of it. The density distribution in the model is slightly different than in the observations, as can be seen from the residual maps for both PVs. The model still gives a very good description of the data.
The CO data confirms a dip in the total rotation curve of NCG3626. The rotation velocity inwards from the dip might be lower if the inclination of the CO disk was determined incorrectly (for example, due to a misinterpreted, broken CO disk in the outer parts). However, a dip feature would still be present. Even for the extreme case of an edge-on CO disk (which is clearly not the case as seen in Fig. 2.2), the rotation velocity at low radii stays around 200 km/s.
We find that our PA estimates in the outer parts of the galaxy are about 10° bigger than the literature values (Silchenko et al., 2010), which, nevertheless, is still within the estimated uncertainty on there values. Our rotation curve is about 50 km/s higher in the innermost parts of the galaxy than the one presented in Mazzei et al. (2014), which might be due to the data quality in previous works, beam smearing or modeling effects.
We found indications of a warp from the comparison of the inclinations and position angles for the CO and the HI, and ^{3D}Barolo also attempts to model a warp. The extension of this

Galaxy	Line	RA [hms]	DEC [hms]	v_{sys} [km/s]	i [°]	PA [°]	i_{Barolo} [°]	PA_{Barolo} [°]	v_{disp} km/s
NGC2824	CO	9 19 2.19	+26 16 11.9	2720.	50 ± 2.3	157 ± 8.8	52 ± 2.3	160 ± 8.8	10 ± 0.8
	HI	9 19 2.49	+26 16 12.0	2730.	70 ± 1.7	160 ± 11.2	70 ± 1.7	162 ± 11.2	7 ± 0.02
NGC3626	CO	11 20 3.80	+18 21 24.5	1468.	44.9 ± 1.8	163 ± 7.1	–	–	4 ± 0.2
	HI	11 20 4.50	+18 21 34.5	1468.	65 ± 4.3	181 ± 9.7	–	–	17 ± 5.2
UGC6176	CO	11 7 24.69	+21 39 25.3	2680.	54 ± 0.6	30 ± 5.0	53 ± 0.6	35 ± 5.0	10 ± 0.08
	HI	11 7 24.70	+21 39 25.9	2670.	58 ± 1.0	33 ± 7.5	56 ± 1.0	27 ± 7.5	15 ± 8.9

Table 3.2: Radius independent rotation curve parameters. Right ascension and declination are given in J2000. The angles are given as determined in the interactive derivation and by ^{3D}Barolo, respectively. The errors on the angles, as well as the velocity dispersion with uncertainty, are determined from ^{3D}Barolo. "–" indicates that the respective value was modeled as radius-dependent. These values can be found in Tab. 3.3.

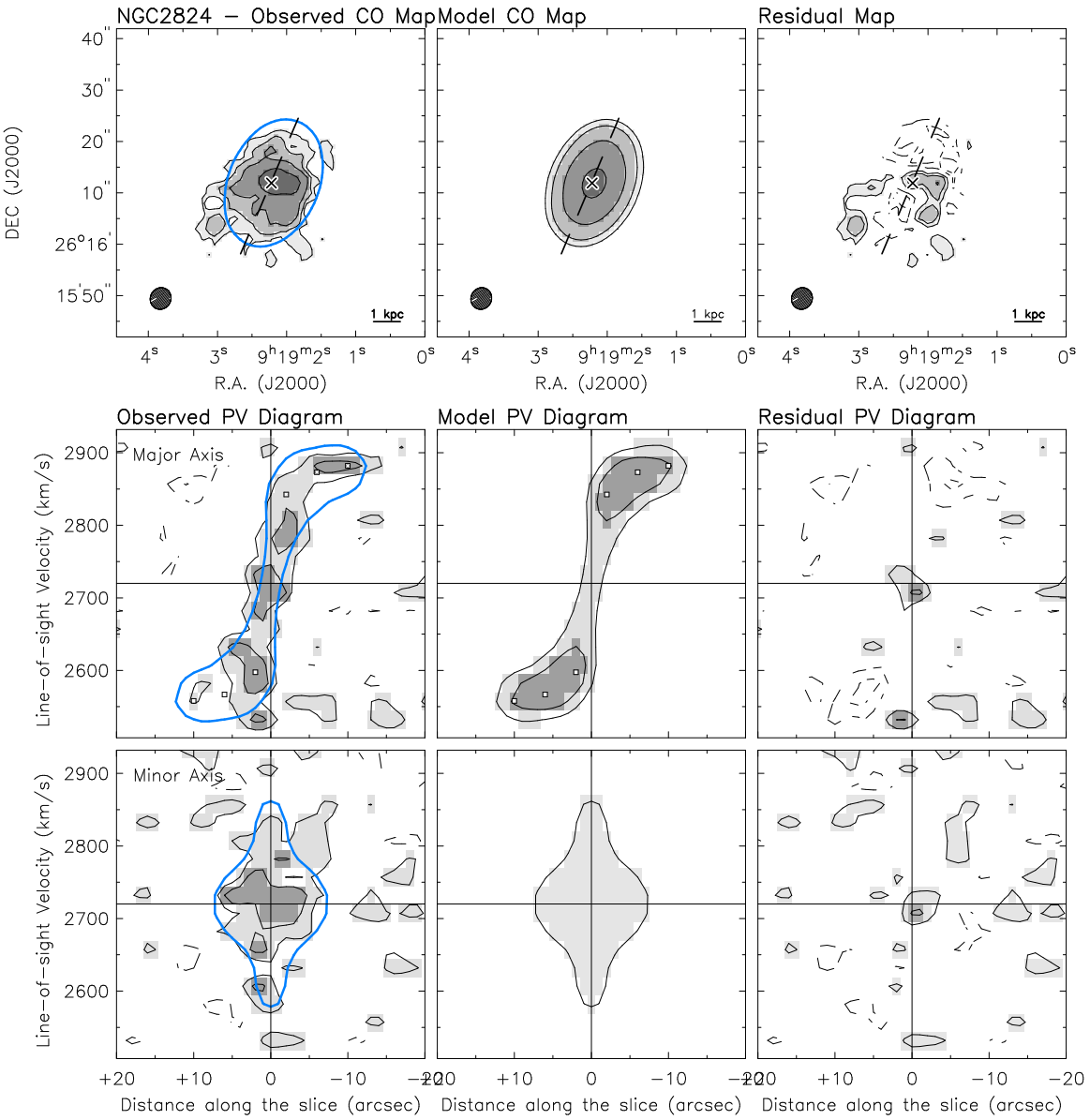

Figure 3.1: Top-left panel: CO intensity map derived from ATLAS^{3D} observations, overlaid in blue with the outermost contour of the model intensity map. Top-central panel: model intensity map. Top-right panel: residual intensity map. Bottom panels: position-velocity diagrams taken along the major and minor axes from the observed datacube (left), model datacube (middle) and residual datacube(right). The white squares show our derived rotation curve. The outermost contour of the model is plotted in blue over the observed PVs for comparison. The density contours in the PV diagrams correspond to -1.5σ, -3σ, -6σ, and so on (dashed) and 1.5σ, 3σ, 6σ, and so on (solid), where σ is the measured noise in the cube (see Tab. 2.1). The contours in the maps correspond to 1$\sigma_{\rm pseudo}$, 2$\sigma_{\rm pseudo}$, 4$\sigma_{\rm pseudo}$, 8$\sigma_{\rm pseudo}$, and so on.

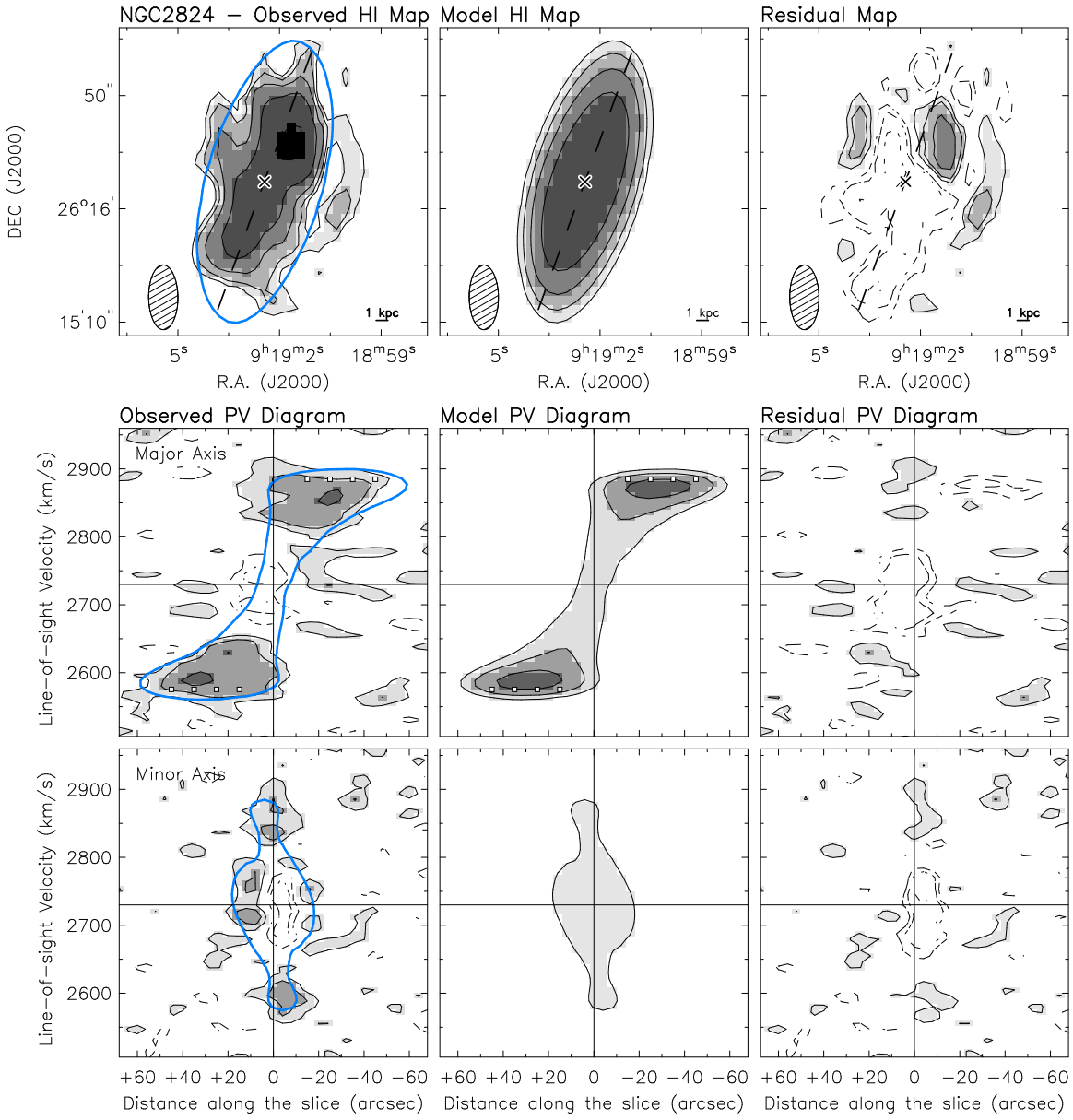

Figure 3.2: Same as Fig. 3.1, but for the HI of NGC2824.

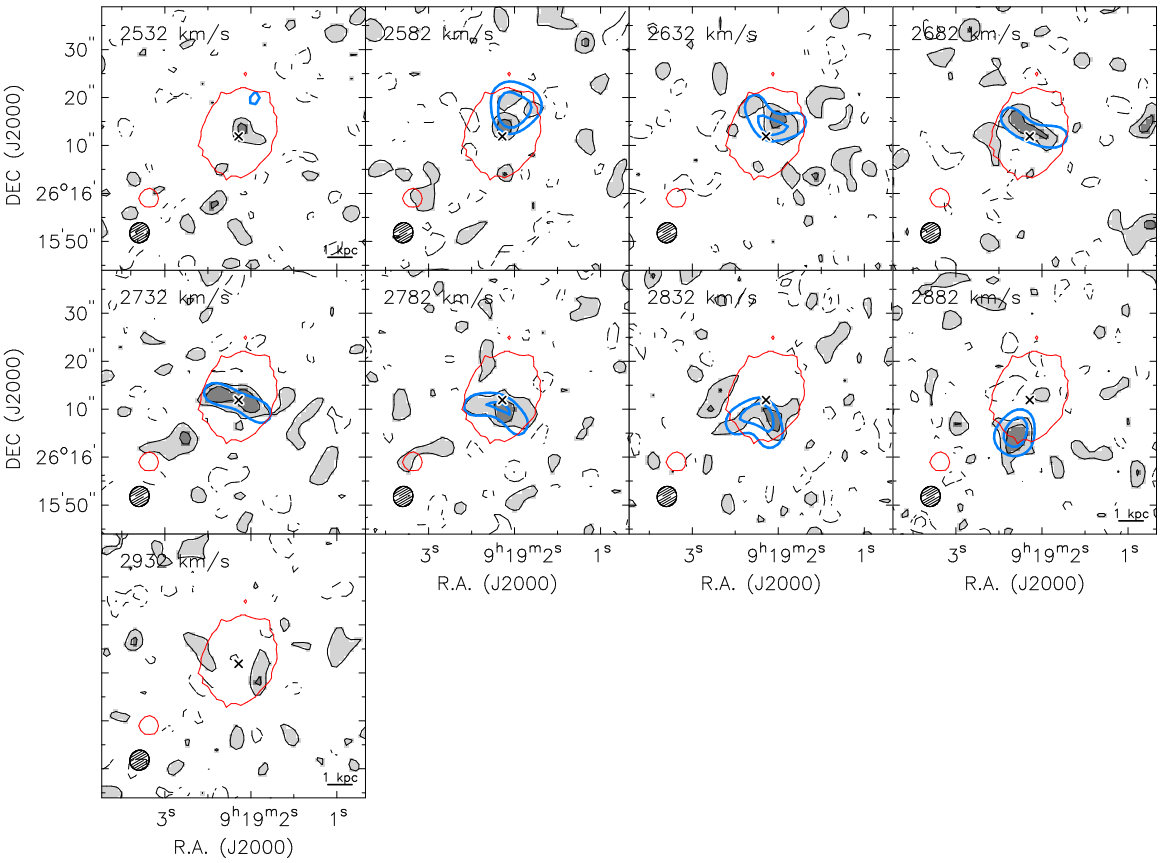

Figure 3.3: CO channel maps for NGC2824. In black - the observed cube, in blue - the model, in red - the extent of the stellar body. The line-of-sight velocity is shown in the upper left corner. The contours correspond to 1.5σ, 3σ, 6σ, and so on.

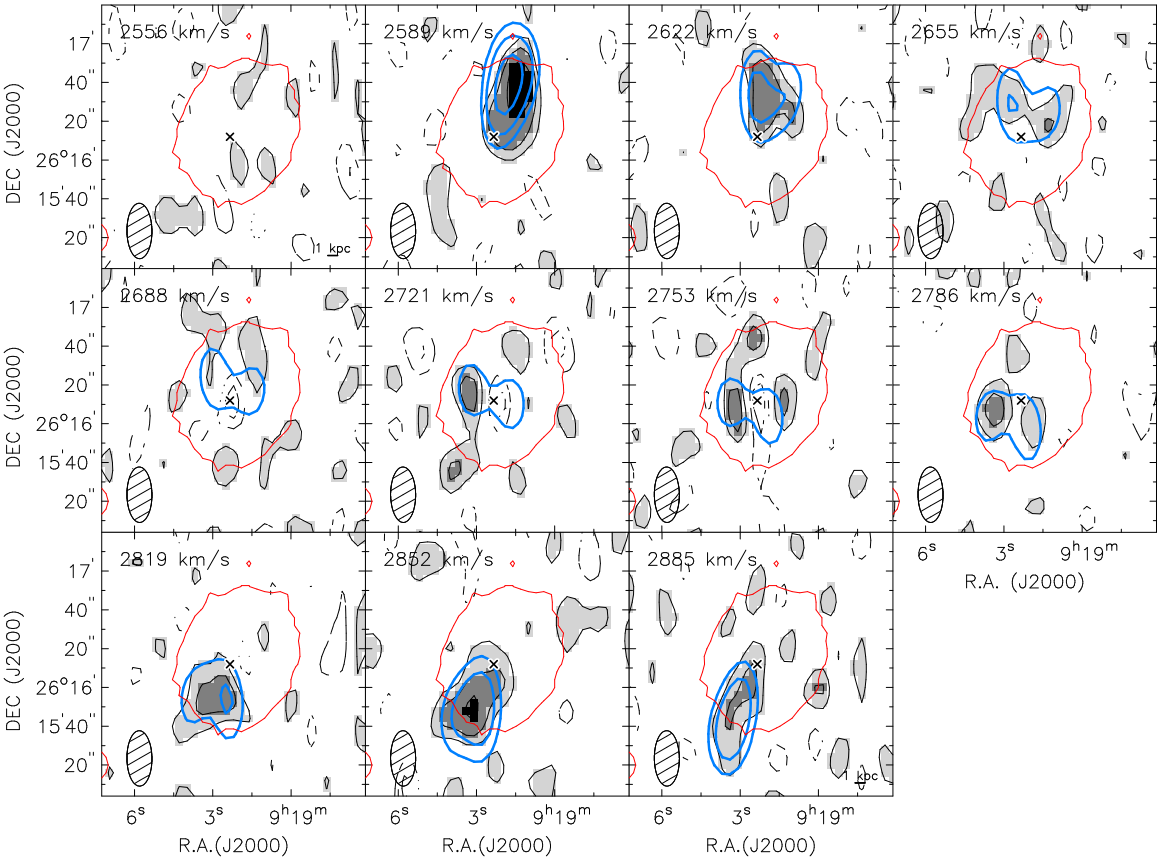

Figure 3.4: Same as Fig. 3.3, but for the HI of NGC2824.

R [kpc]	v [km/s]	δv [km/s]	$\Sigma_{\rm HI}$ [$M_\odot$/pc^2]	$i_{\rm Barolo}$ [°]	$PA_{\rm Barolo}$ [°]
0.22	168	15	58.73	47	170
0.66	216	15	45.15	47	170
1.11	241	15	34.37	47	170
1.55	251	16	19.06	50	170
1.67	256	10	0.93	50	170
4.50	154	12	0.74	60	178
8.33	127	13	0.71	67	181
11.66	148	13	0.76	67	181
14.99	163	10	0.81	66	181
18.32	175	10	0.73	65	181
21.65	185	13	0.49	65	181
24.99	195	20	0.23	65	181

Table 3.3: Rotation curve and density profile of NGC3626. In ^{3D}Barolo, we modeled the warp, fixing the inclination and position angles to the values in the last two columns.

warp is much bigger than the warp structures near the galactic center described in section 1.6.2. We modelled the warp with ^{3D}Barolo and compared to the rotation curve derived interactively where the warp is modelled very roughly by assuming different i and PA for CO and HI and not modeling any transition between the values. The values of the angles we fixed for the ^{3D}Barolo modeling together with the estimated rotation curve values can be found in Tab. 3.3. We find that the rotation curve is not very sensitive to the modeling we performed.
In Figs. 3.8 and 3.7 we display the individual channel maps of the observations and the model in the same manner as in subsection 3.3.1. Good agreement is observed.

3.3.3 UGC6176

The results for the CO and the HI of UGC6176 can be seen in Figs. 3.9 and 3.10, organized as in the previous figures. Due to the elongated beam, in both HI and CO observations we can divide the galaxy only in a few rings. The shape of the beam leads to an extreme beam smearing in the intensity map, so we have to multiply the derived density by 1.25 to better reproduce the observed density distribution. The resulting model reproduces the density distribution quite well, although the CO intensity residuals show that the density is slightly overpredicted. The modeled density profile of the HI model is also not quite accurate, as can be seen from the residuals of the major axis PV diagram. However, these small deviations do not significantly influence the shape of the derived rotation curve and will be accounted for in the uncertainty estimation.
The strong beam smearing can be seen also in the PVs of the HI, with a roughly constant rotation velocity at all radii. The CO helps to determine the rotation curve shape in the inner part of the galaxy, as the velocity determined for it is slightly smaller than the one for the HI.
Although the ATLAS^{3D} collaboration denotes UGC6176 as a warped galaxy, we find no evidence for that. Both the position angles and the inclinations of the HI and the CO are consistent with each other and show no big variation with radius.
In Figs. 3.11 and 3.12, we present the channel maps of the data and the model for the CO and the HI respectively. Again, the model cannot reproduce asymmetric features, but overall the contours agree, showing that the rotation curve estimate is accurate.

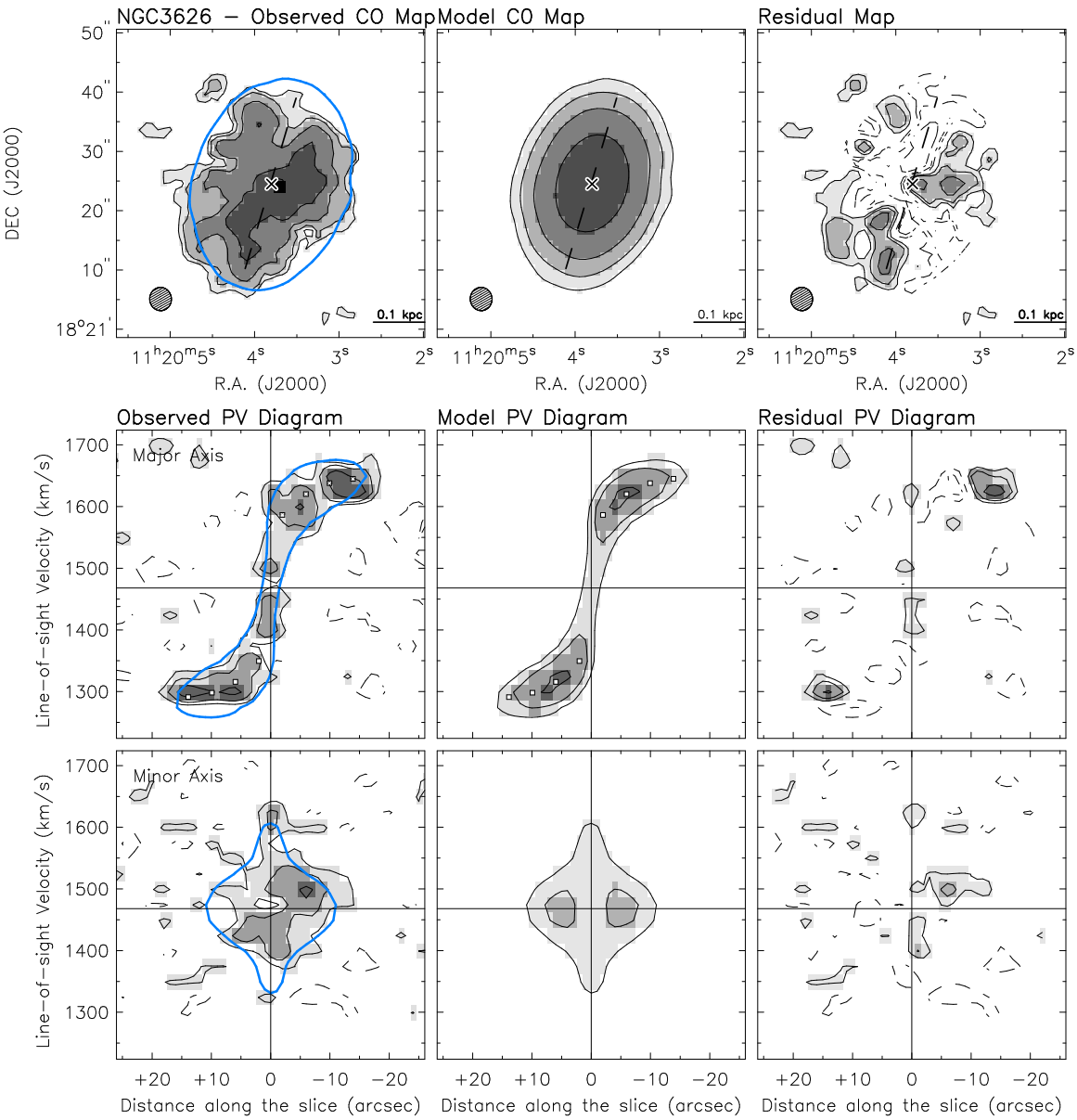

Figure 3.5: Same as Fig. 3.1, but for the CO of NGC3626.

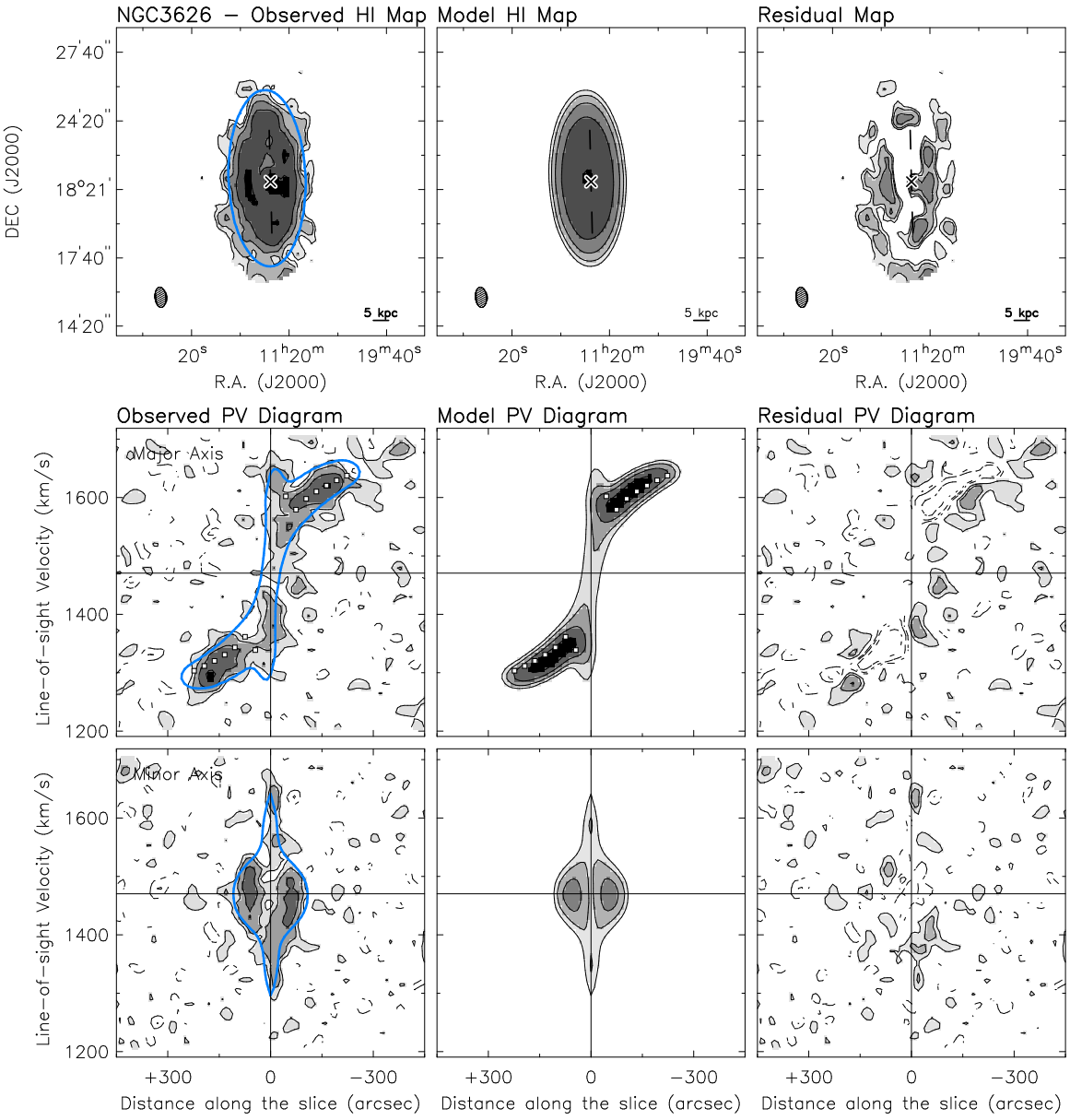

Figure 3.6: Same as Fig. 3.1, but for the HI of NGC3626.

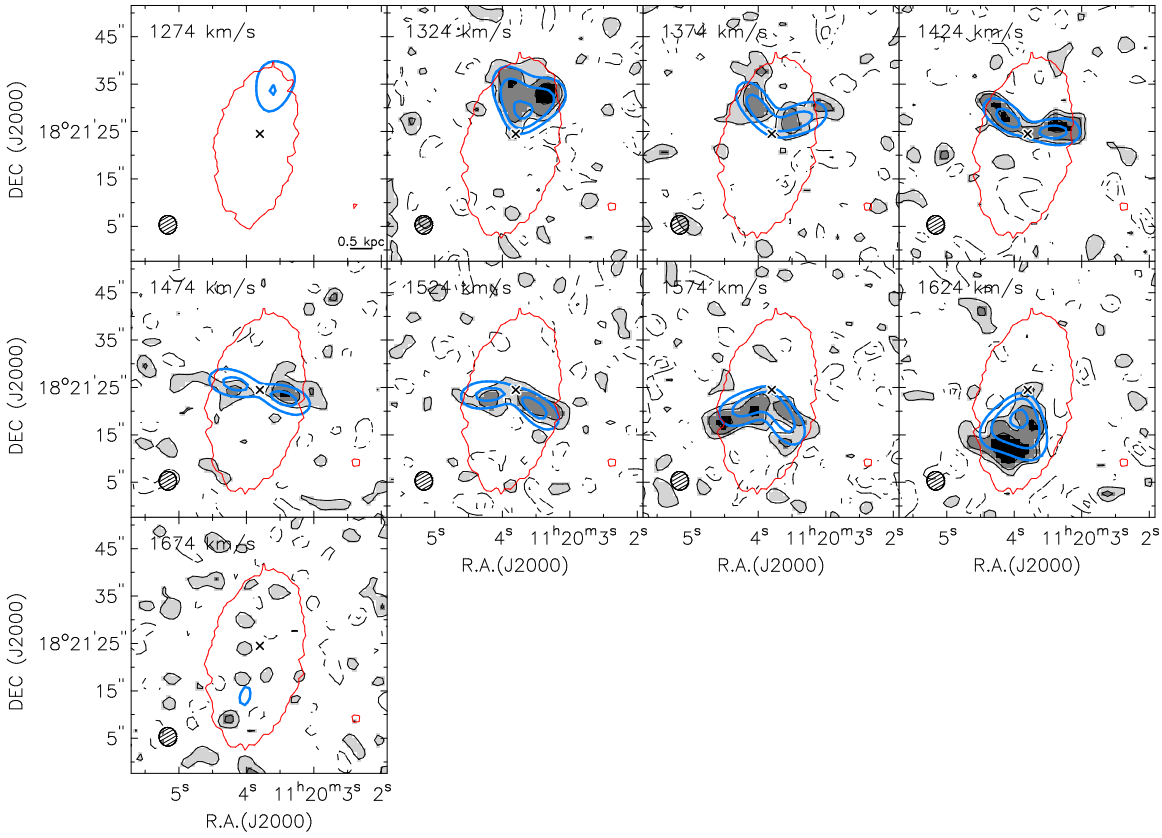

Figure 3.7: Same as Fig. 3.3, but for the CO of NGC3626.

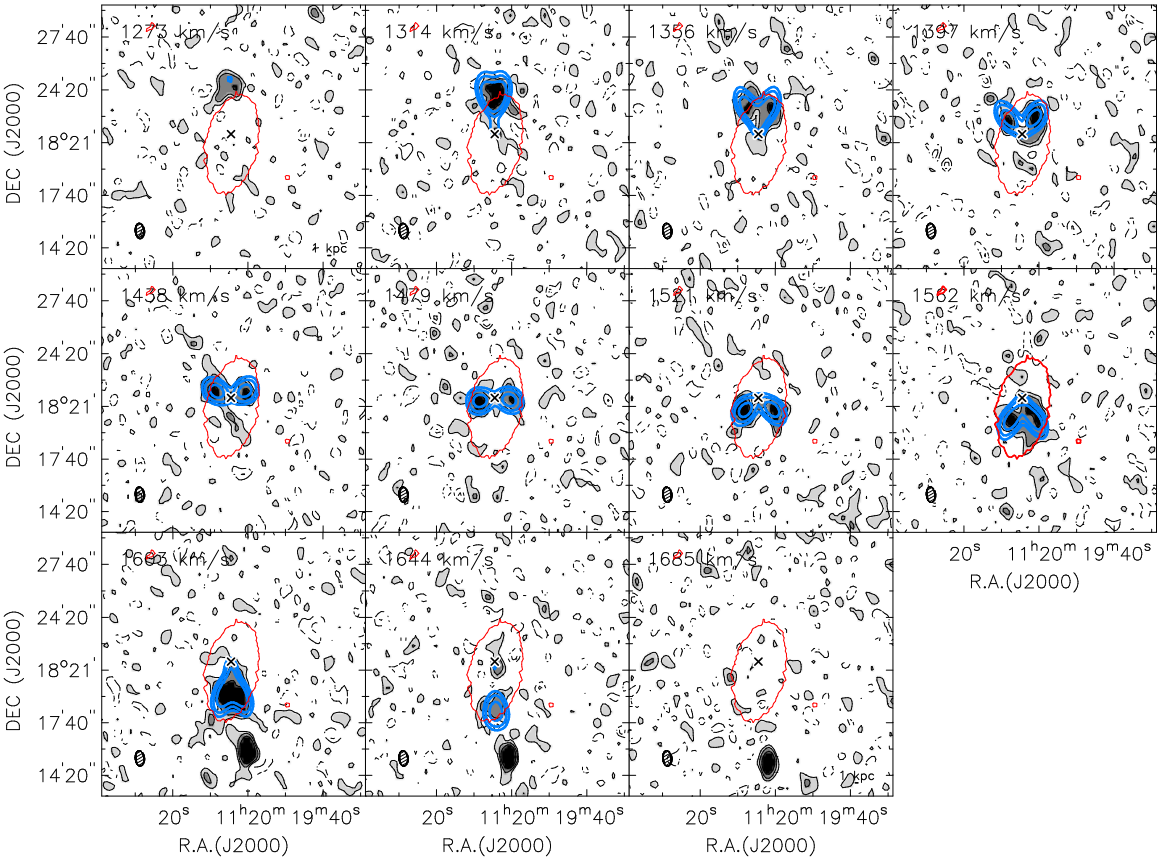

Figure 3.8: Same as Fig. 3.3, but for the HI of NGC3626.

R [kpc]	v [km/s]	δv [km/s]	Σ_{HI} [$M_\odot/pc^2$]
0.29	135.	14	287.3
0.86	135.	14	73.01
3.81	140.	8	1.39
11.43	140.	8	0.81
19.05	140.	8	0.30

Table 3.4: Rotation curve and density profile of UGC6176.

3.3.4 Comparing the two methods to derive rotation curves

In Fig. 3.13 we plot the rotation curves derived with the two methods (*rotcur* plus *galmod* vs ^{3D}Barolo) to check whether they agree.
For the CO of NGC2824 and both the CO and the HI of UGC6176, we chose smaller radius widths for the ^{3D}Barolo modeling, as the small number of radii used in the manual derivation was not sufficient to get a reasonable result with the algorithm.
In general, a good agreement between the different curves is seen, especially for NGC3626. An exception is the CO of NGC2824, where the spatial resolution and signal-to-noise levels of the galaxy were not high enough. Also, this galaxy has an absorption feature in the galactic centre, which ^{3D}Barolo cannot process. Together, this is leading to an unphysical rotation curve estimate by ^{3D}Barolo. In fact, the ^{3D}Barolo estimate of the rotation curve does not lie on the position-velocity diagram. This is highlighting the importance of visual inspection of each galaxy.
In NGC3626, the dip in the rotation curve gets reproduced also with ^{3D}Barolo. The determined inclination values are close to the ones we found in the interactive modeling, giving support to the rotation velocities we adopt inwards of the dip.
In the bottom panels of Fig. 3.13, we show the inclination and position angle values adopted for the ^{3D}Barolo fits. We model the warp in NGC3626, but not in NGC2824, due to the low resolution of the data. As stated before, we do not see evidence for a warp in UGC6176.

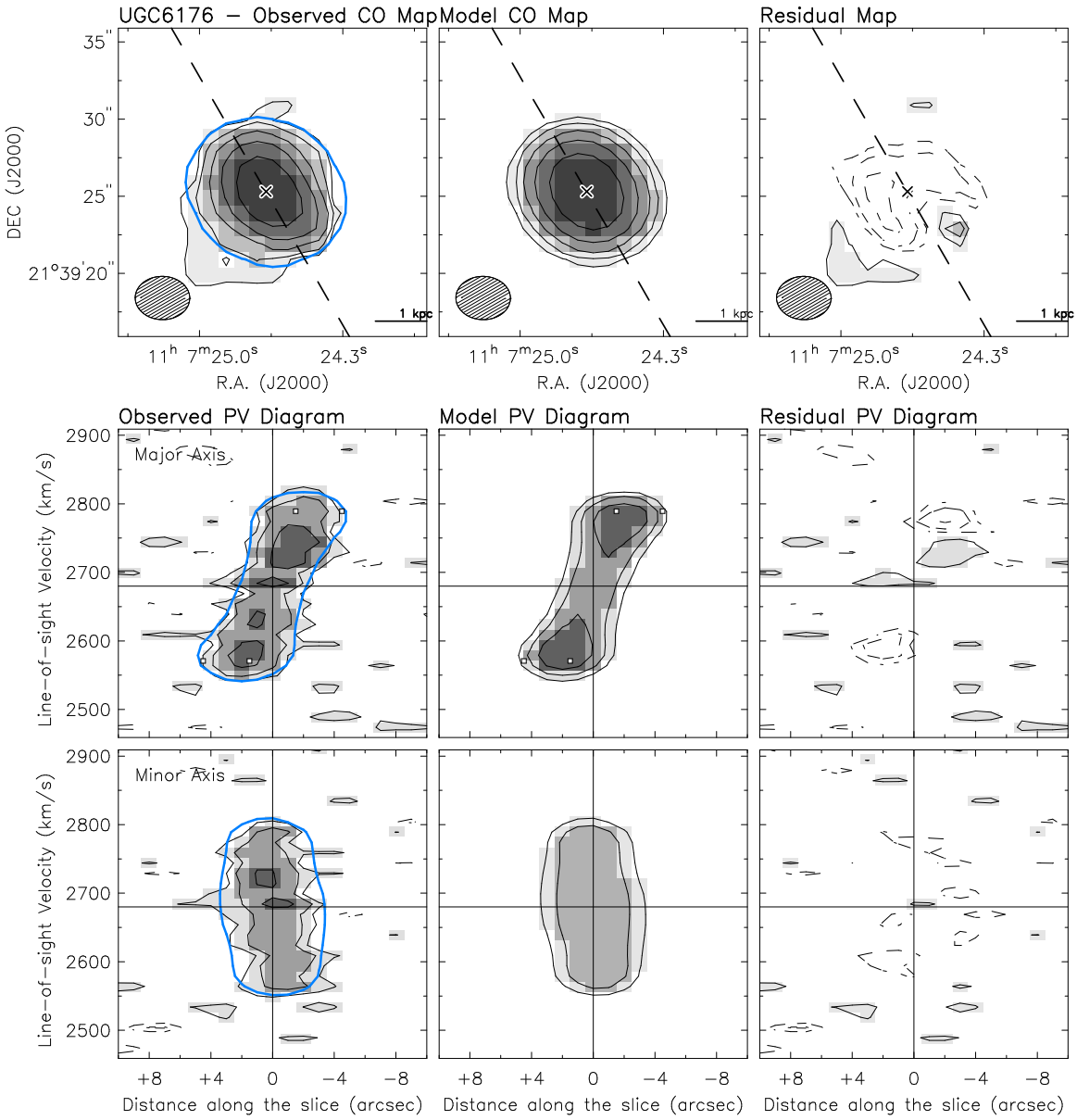

Figure 3.9: Same as Fig. 3.1, but for the CO of UGC6176.

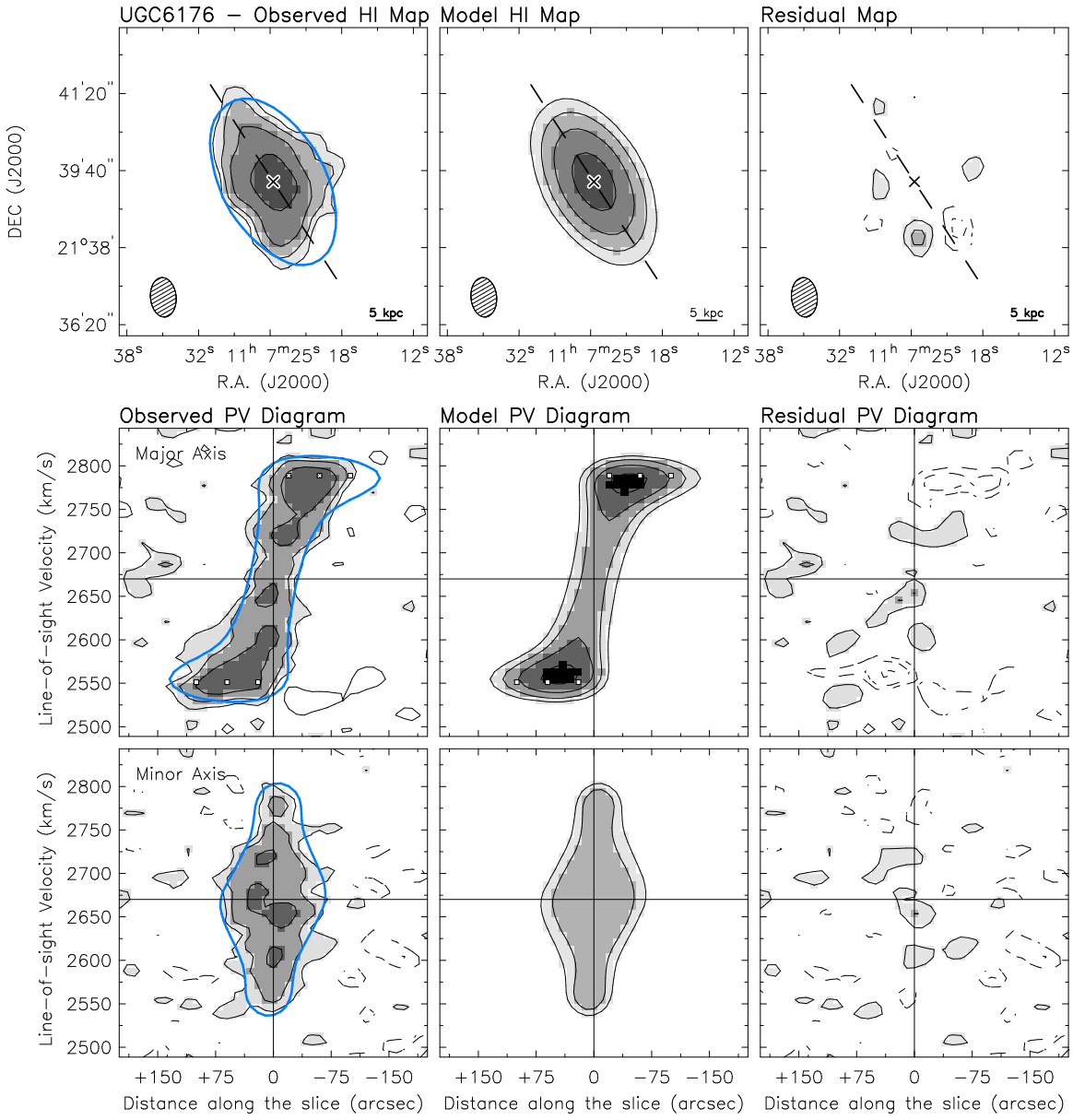

Figure 3.10: Same as Fig. 3.1, but for the HI of UGC6176.

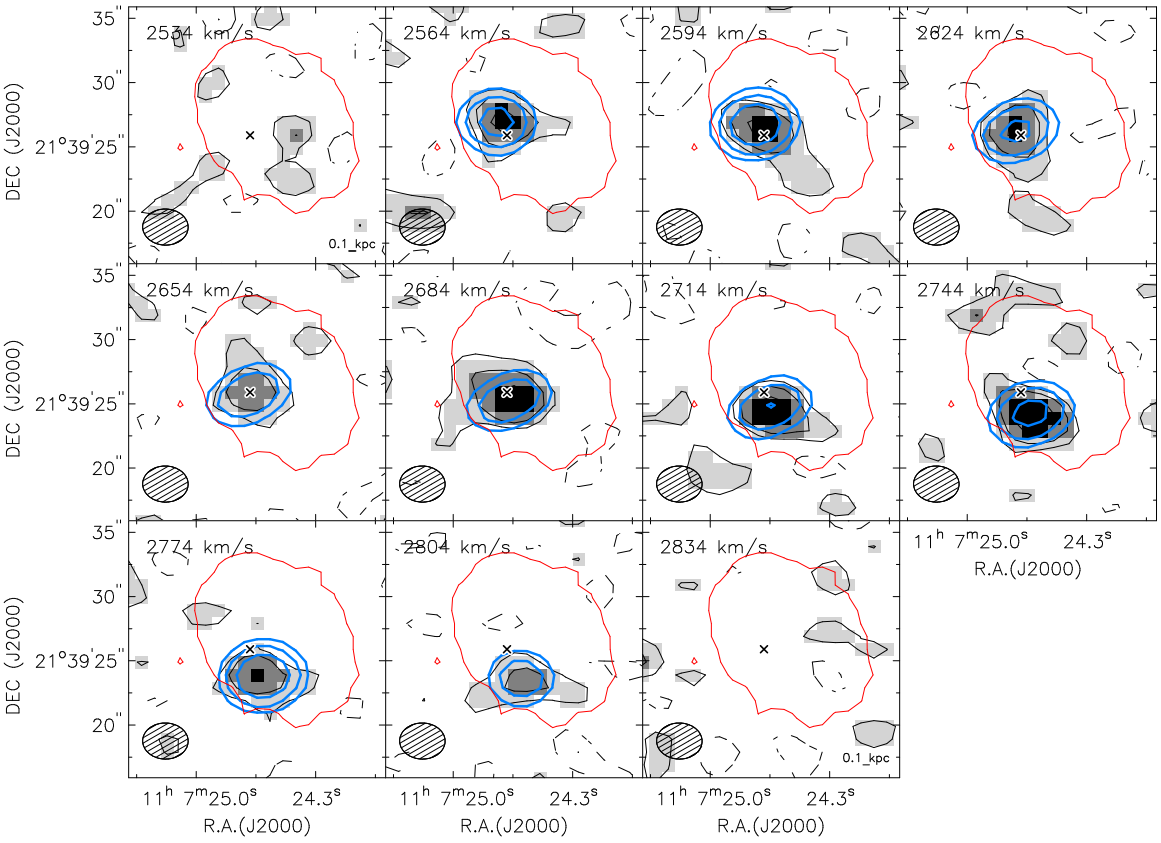

Figure 3.11: Same as Fig. 3.3, but for the CO of UGC6176.

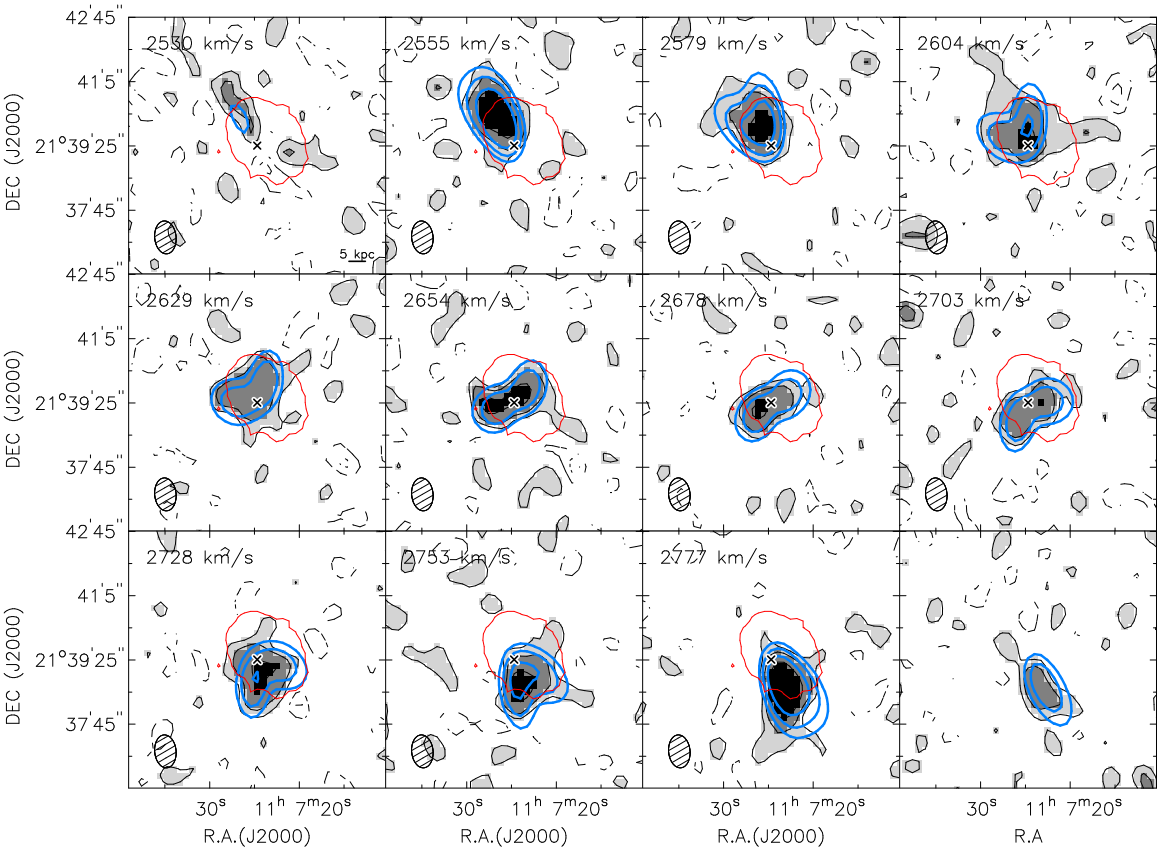

Figure 3.12: Same as Fig. 3.3, but for the HI of UGC6176.

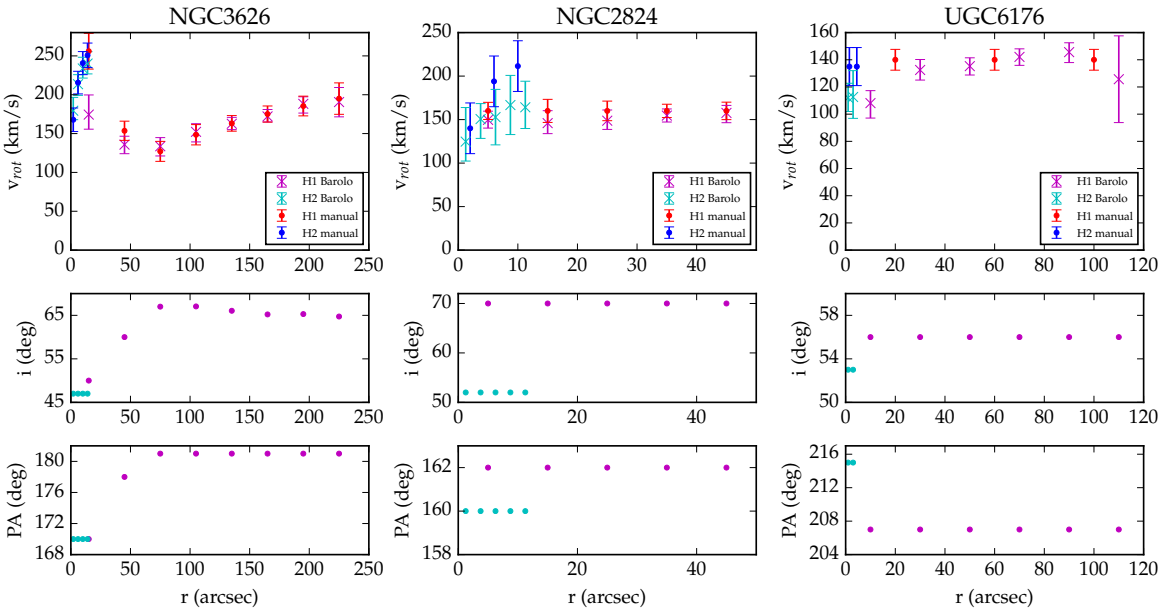

Figure 3.13: Comparison of the rotation curves derived with *rotmod* and *galmod* and with ^{3D}Barolo. In the bottom panels, the inclination and position angle used for the ^{3D}Barolo fit.

Chapter 4

Mass models and Radial acceleration relation

In this chapter, we will discuss what can be inferred about the mass composition of our three sample galaxies using the rotation curves derived in chapter 3. For this, we need to estimate the mass contained in the visible components of the galaxies, calculate the expected rotation velocities, and compare them with the observed rotation curves.

4.1 Estimating the mass distribution of luminous galactic components

Estimating the mass of the gas and the stars inside a distant galaxy is not a straightforward task. For the gas, the total mass can be estimated quite accurately due to the known element abundances in the universe. Hydrogen dominates the universe with 74%, followed by helium with 24%. Heavier elements contribute only with roughly 2%. With the relations described in section 3.2.2, one can calculate the mass of atomic hydrogen in a galaxy from its 21cm flux. To estimate the H_2 mass from the CO luminosity, we use the conversion $\Sigma_{H_2} = X_{CO} T_{CO}$ (Bolatto et al., 2013), with the emission temperature

$$T_{CO} = 1.222 \cdot 10^6 \frac{S_{CO} \Delta v}{\nu^2 \cdot x_{beam} y_{beam}} \cdot x_{pxl} y_{pxl} \tag{4.1}$$

where S_{CO} is the measured intensity, Δv is the channel width and ν is the rest frequency of the emission and the rest are the sizes of the beam and the pixel.
The total hydrogen mass can be then scaled, taking into account the contribution of helium, such that $M_{gas} = 1.33 M_H$. Measurement uncertainties in the surface brightness profile and the absolute flux calibration translate into an error of roughly 10% on this mass estimate.
As for the mass of the stars, it is harder to assess, as in most galaxies individual stars cannot be resolved. Therefore, the mass has to be concluded from the integrated color and luminosity of the whole galaxy. In general, the mass of the galaxy can be related to its luminosity by a mass-to-light ratio (M/L), derived empirically. This ratio depends on the observation wavelength. For instance, in the UV, recent star formation has a very strong effect, while in the IR one probes the bulk of old stars.
Typical M/L values for the different galaxy colors can be found from stellar population synthesis models that take into account the star formation history and stellar evolution as a function of age. It has been shown (e.g., Rix & Zaritsky, 1995) that these values are the most robust and suffer the least from star-formation fluctuations in the near-IR, probing old stars that contain most of the mass of the stellar body. Therefore, typical values of the M/L can best be provided at these wavelengths.
We use [3.6] Spitzer images to derive the luminosity profiles of the bulge and the disk. We then adjust the M/L values for the disk and the bulge contributions to the rotation curve in order to achieve a maximally satisfying fit to the observations.

4.2 Luminosity profile decomposition

We use the [3.6] luminosity profiles from Lelli et al. (2017) and non-parametrically decompose them into the bulge and the disk components.
The SPARC database already provides a luminosity profile decomposition for all its galaxies. However, in this work, we repeat the decomposition procedure for our three galaxies to estimate the impact of the ambiguity involved in this process and results derived from it.
For the decomposition, a characteristic radius R_{bul} is identified up till which the bulge dominates the intensity profile. The bulge contribution beyond this point and the disk contribution inward from it are modeled by exponential profiles. The rest of the surface brightness gets assigned to the respective other component.
We estimate by trial and fail the largest R_{bul}, for which the decomposition into bulge and disk is physically possible and also sensible. We compare the achieved decomposition with the decompositions provided by SPARC in Fig. 4.1. We find that for NGC3626 and NGC2824 the bulge and disk components nearly do not change, while for UGC6176 the bulge in the

SPARC decomposition is significantly smaller than estimated in this work. We decide to use our decomposition for the rest of this work. However, we performed all analysis also using the SPARC decomposition and have seen that the results are mostly not sensitive to this choice.
The outer parts of the disk also get fitted by an exponential profile to be able to extrapolate it continuously beyond a certain radius, where the intensity profile is not reliably traced. This allows us to avoid abrupt, unphysical truncations in the outer disk profile.

4.3 Mass models

To find out how much each individual component of the galaxy contribute to the rotation velocity, one needs to calculate the contribution of each component to the gravitational potential. This is done using the task *rotmod* in *gipsy*. The task takes the density distribution and (if provided) an estimated total mass of the component, and calculates the gravitational potential as a function of R in the galactic plane for a given 3D geometry. For the bulge, we assume spherical geometry, while the disk is assumed to be thick with a vertical exponential profile. We set the characteristic scale heights of the HI and CO disks to be 100 pc, while for the scale height of the stellar disk we assume it correlates with the disk size as $z_{char} = 0.196 R_d^{0.633}$. This relation is derived by studying edge-on galaxies (Bershady et al., 2010).
If a total mass is provided, *rotmod* norms the resulting profile to reproduce this mass.
For the spherical profile, the force can be found to be

$$\frac{\partial \Phi}{\partial r} = \frac{2\pi G}{R^2} \int_0^R u \Sigma_{\rm bulge}(u)\ du + \frac{4G}{R^2} \int_R^\infty \left(\arcsin\left(R/u\right) - \frac{R}{(\sqrt{u^2 - R^2})} \right) u \Sigma_{\rm bulge}\ du, \quad (4.2)$$

where $\Sigma_{\rm bulge}$ is the projected surface brightness (Kent, 1986).
For the disk,

$$\frac{\partial \Phi}{\partial r} = 8\pi G \int_0^\infty u \Sigma_{\rm disk}(u) \int_0^\infty \frac{\partial \rho(u,z)}{\partial u} \cdot \frac{K(p) - E(p)}{\pi \sqrt{rup}}\ dz\ du, \quad (4.3)$$

where $p = x - \sqrt{x^2 - 1}$, $x = (r^2 + u^2 + z^2)/2ur$, K(p) and E(p) are the complete elliptical integrals of the first and second kind respectively. $\rho(u,z) = \Sigma(u) \cdot Z(z)$, where $\Sigma(u)$ is observed and $Z(z) = \exp\left(-z/z_0\right)/z_0$ is the adopted exponential vertical density distribution in the disk (Casertano, 1983).

From the forces, the circular velocity as a function of the radius in the disk can be derived as

$$v_c^2(R) = r \frac{\partial \Phi}{\partial r}. \quad (4.4)$$

In Tabs. 4.1 to 4.2, we display rotation velocities and density profiles for the individual components of our galaxies at radii, with measured rotation velocities.

4.4 The total rotation curve

From the density distribution of the individual components, we can calculate their contribution to the gravitational force. Hence, we can also calculate the rotation velocity

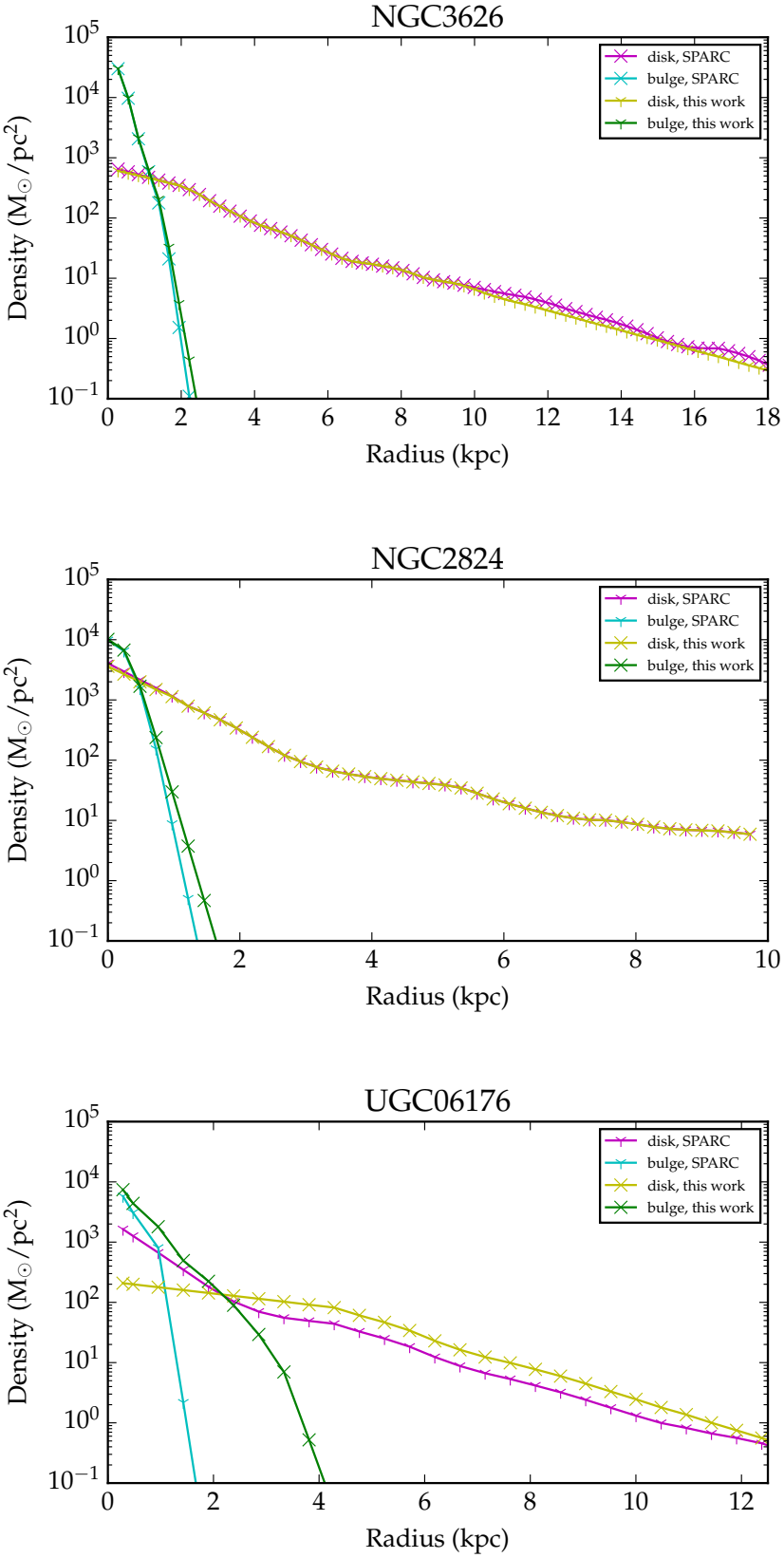

Figure 4.1: Comparison of the luminosity profile decomposition performed in Lelli et al. (2016) and in this work. Only for UGC6176 a significant difference is seen. We use the decomposition derived in this work in all further analysis.

R [kpc]	v_{H_2} [km/s]	v_{HI} [km/s]	v_{disk} [km/s]	v_{bulge} [km/s]	Σ_{H_2} [$L_\odot/pc^2$]	Σ_{HI} [$L_\odot/pc^2$]	Σ_{disk} [$L_\odot/pc^2$]	Σ_{bulge} [$L_\odot/pc^2$]
0.38	11.92	-0.03	114.812	229.53	61.73	0.33	4526.11	7239.94
1.15	26.56	0.66	212.01	192.68	35.81	0.34	1715.51	14.16
1.92	31.03	1.20	232.53	149.40	17.81	0.34	707.11	0.02
2.88	33.28	1.96	213.44	121.92	8.94	0.35	194.90	0
4.81	30.22	3.66	177.21	94.44	2.01	0.34	83.33	0
6.73	25.90	5.35	160.29	79.82	0.45	0.31	24.92	0
8.65	22.42	6.73	142.18	70.39	0.10	0.24	14.13	0

Table 4.1: NGC2824: rotation curves and density profiles of the individual baryonic galaxy components from *rotmod*, evaluated at radii, at which observed rotation velocities are available.

R [kpc]	v_{H_2} [km/s]	v_{HI} [km/s]	v_{disk} [km/s]	v_{bulge} [km/s]	Σ_{H_2} [$L_\odot/pc^2$]	Σ_{HI} [$L_\odot/pc^2$]	Σ_{disk} [$L_\odot/pc^2$]	Σ_{bulge} [$L_\odot/pc^2$]
0.29	0.71	25.36	14.04	202.73	3.77	239.88	320.42	14644.58
0.86	2.62	41.57	36.53	240.96	3.66	57.28	280.67	1883.00
3.81	9.45	24.78	104.82	162.22	3.13	0	140.59	0.12
11.43	20.80	13.78	88.64	93.64	1.74	0	1.89	0
19.05	24.78	10.70	65.45	72.54	0.60	0	0.28	0

Table 4.2: As Tab. 4.1, but for UGC6176.

R [kpc]	v_{H_2} [km/s]	v_{HI} [km/s]	v_{disk} [km/s]	v_{bulge} [km/s]	Σ_{H_2} [$L_\odot/pc^2$]	Σ_{HI} [$L_\odot/pc^2$]	Σ_{disk} [$L_\odot/pc^2$]	Σ_{bulge} [$L_\odot/pc^2$]
0.22	7.27	-0.61	36.37	308.75	55.47	1.09	3079.72	34120.81
0.67	17.85	1.03	96.73	345.55	40.54	1.06	2662.19	2088.62
1.11	25.99	1.73	146.16	300.14	27.23	1.03	2301.26	510.46
1.55	29.34	2.32	188.50	261.14	10.66	1.00	1965.91	22.37
4.99	14.86	4.73	266.27	145.97	0	0.78	253.86	0
8.32	11.37	5.82	225.72	113.07	0	0.78	59.23	0
11.65	9.58	9.06	198.28	95.56	0	0.86	22.29	0
14.98	8.44	14.13	176.17	84.28	0	0.82	5.13	0
18.31	7.63	18.20	158.38	76.23	0	0.55	0	0
21.64	7.02	18.44	141.82	70.12	0	0.23	0	0
24.97	6.53	17.01	130.81	65.28	0	0.12	0	0

Table 4.3: As Tab. 4.1, but for NGC3626.

$v_{\rm rot}^2 = R\,\partial\Phi/\partial R$ of the test particle at every radius. The gravitational potential of the components adds linearly. It follows that the velocities of the components add in quadrature. Therefore, the expected rotation curve is given by

$$v_{\rm tot}^2(R) = \left(\frac{M}{L}\right)_{\rm disk} \cdot v_{\rm disk}^2(R) + \left(\frac{M}{L}\right)_{\rm bulge} \cdot v_{\rm bulge}^2(R) + 1.33 \cdot (v_{\rm HI}^2(R) + v_{\rm H2}^2(R)), \quad (4.5)$$

where the contribution of the stars has been decomposed into the individual contributions of the disk and the bulge and the contributions of HI and H_2 account for the gaseous components. Here, (M/L) denotes the mass-to-light ratio for the stellar disk and the bulge (as indicated), while the 1.33 factor in front of the gaseous components takes the mass contribution of helium and heavier elements into account.
The error on $v_{\rm tot}(R)$ can be estimated by error propagation as

$$\Delta v_{\rm tot}(R) = \frac{1}{2v_{\rm tot}} \sqrt{\left(v_{\rm disk}^2 \Delta M/L_{\rm disk}\right)^2 + \left(v_{\rm bulge}^2 \Delta M/L_{\rm bulge}\right)^2 + \left(\Delta {\rm M_{gas}} \cdot (v_{\rm HI}^2 + v_{\rm H2}^2)\right)^2 + \left(\frac{v_{\rm tot}}{2D}\Delta D\right)^2}, \quad (4.6)$$

where we denote the relative error on the gas mass by $\delta {\rm M_{gas}}$. We take it to be 10%. We estimate the relative errors on the mass-to-light ratios to be 30% in all cases. For the distances, we assume the relative error to be 10%.

4.5 Results

4.5.1 Maximum disk mass models

Using equation 4.5, we have calculated the shape of the rotation curve predicted from the luminous matter distribution for our galaxy sample. These rotation curves depend on the adopted mass-to-light ratios for the disks and the bulges of the galaxies (see eq. 4.5). We adjust the mass-to-light ratio values in a way to achieve the best agreement in the inner parts of the galaxies between the observed and the predicted rotation curves. This is known as a maximum disk fit (van Albada & Sancisi, 1986), as, in this fit, the inner rotation curve shape can be fully described by baryonic matter.

Our best fits can be seen in Figs. 4.2 and 4.3 for the disk-bulge decompositions from SPARC and this work, respectively. The parameters for these fit are summarized in Tab. 4.4.
The calculated rotation curves do not agree with the observed ones at large radii. This was to be expected and suggests the presence of dark matter in the galaxies. We will fit various dark matter haloes to the data in chapter 5.
Clearly, the choice of both the disk-bulge decomposition and the mass-to-light ratio affect the shape of the predicted total rotation curve. However, these changes are only important in fitting the inner parts of the rotation curve and have to be considered when quantifying the uncertainty of the latter, not influencing the shape of the expected rotation curve at large radii.
For comparison, in Fig. 4.4 we show a model where we set the M/L to 0.5 for all components (using the decomposition from this work). This choice shifts the rotation curve contributions of the disk and the bulge up with respect to our best fit, with the result that the calculated rotation curve overpredicts the velocities in the inner parts of the galaxies.
The best fit values we found for the M/Ls are much lower than expected for ETGs, being

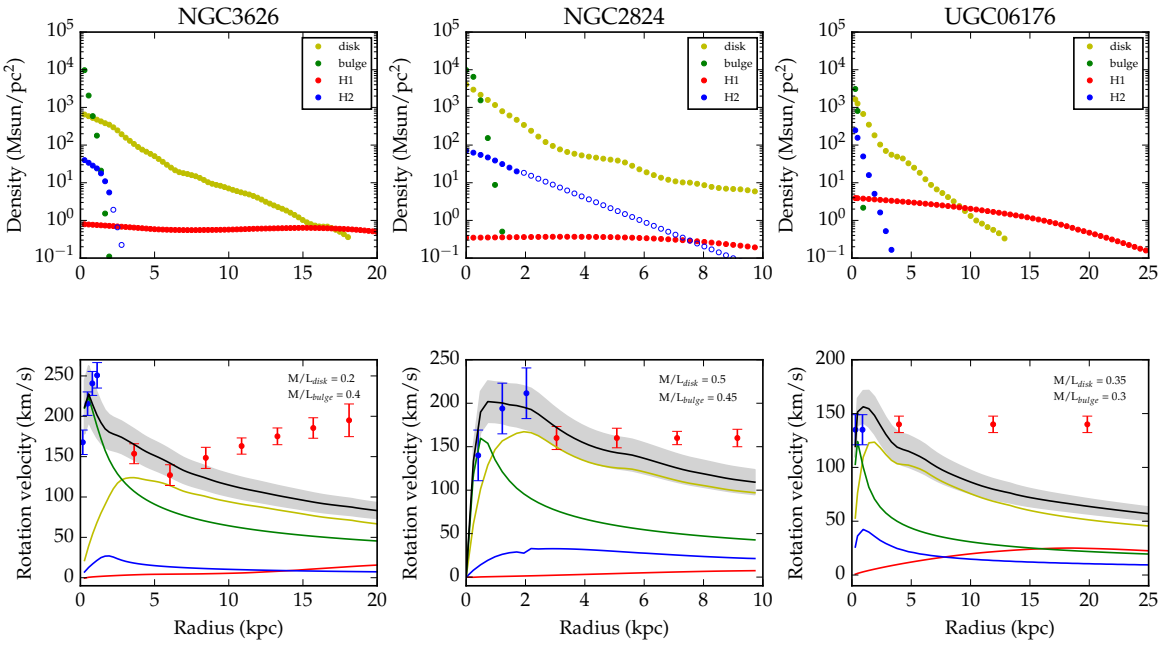

Figure 4.2: Density profiles (top) and maximal disk mass models (bottom), using the disk-bulge decomposition from SPARC.

Decomposition	Galaxy	M/L$_{\text{disk}}$	M/L$_{\text{bulge}}$
this work	NGC2824	0.5	0.45
	NGC3626	0.2	0.4
	UGC6176	0.65	0.3
SPARC	NGC2824	0.5	0.45
	NGC3626	0.2	0.4
	UGC6176	0.35	0.3

Table 4.4: Mass-to-light ratios derived for a maximum disk fit. The fitting is performed using the disk-bulge decomposition derived in this work and using the one provided by SPARC. Since the two decompositions vary significantly only for UGC6176, this is also the only galaxy where one can see a change in the M/L values. Assigning more mass to the bulge, one has to significantly decrease the M/L value of the disk to achieve a fit of comparable quality. From now on we will only use the decomposition derived in this work.

rather in the range typical for star-forming spiral galaxies (see Schombert, McGaugh & Lelli, 2019). This suggests that the three galaxies have only recently stopped forming stars and therefore are faded spirals.

This observation is consistent with the findings of Yildiz et al. (2017), who use a sample of HI-rich and HI-poor galaxies from the ATLAS^{3D} survey. They compare the UV colors of the stellar populations of the two samples and find that HI-rich ETGs are bluer than HI-poor ETGs. The most gas-rich galaxies are as blue as outer parts of typical LTGs. They conclude that gas-rich ETGs host young stellar populations in their outskirts. They also find evidence of low efficiency star formation in these regions. Although our galaxies are not part of their sample (for NGC3626 and UGC6176 no UV observations were available, while NGC2824 was not considered, due to its small HI extension), their HI mass places them among the gas rich ETGs, so our findings of low, LTG-like M/L values are consistent with Yildiz et al.'s suggestion of recent or ongoing star-formation.

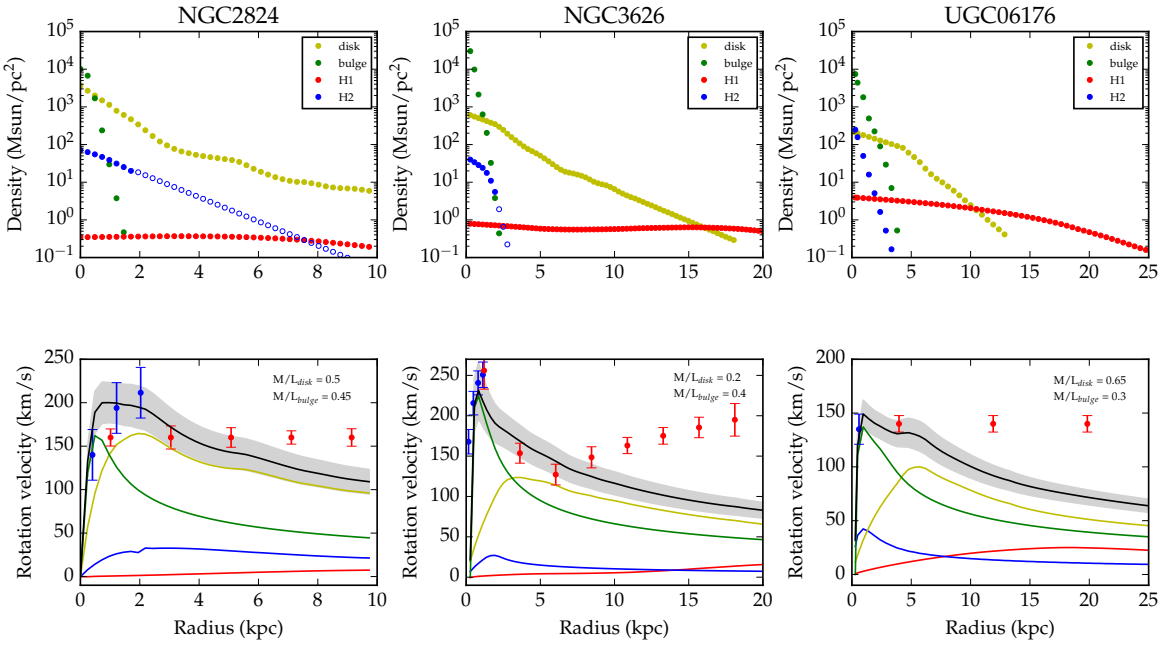

Figure 4.3: As Fig. 4.2, but for the bulge-disk decompositions derived in this work.

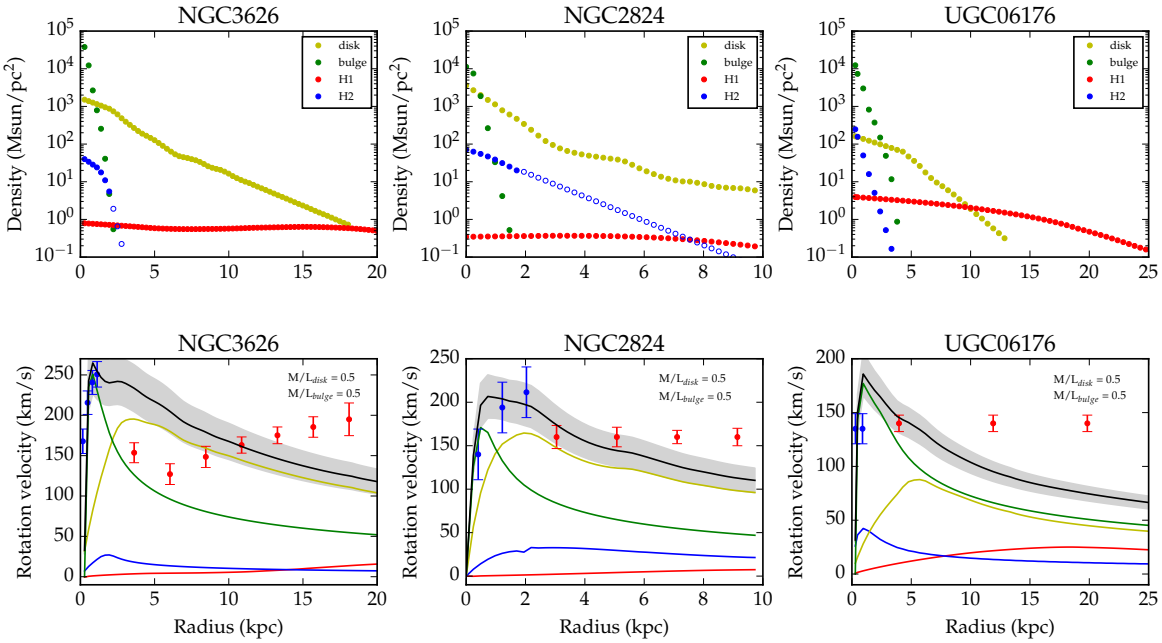

Figure 4.4: Rotation curves for a constant M/L of 0.5 for all stellar components.

4.5.2 Radial Acceleration Relation

In the 1970s, Tully and Fisher observed an empirical relation between galaxy luminosity and rotation velocity in the flat part of the rotation curve. This relation, however, breaks down for low-mass galaxies, where the gas mass is generally higher than the stellar mass. McGaugh et al. (2000) found a more general relation substituting the stellar mass by the total baryonic mass (stars plus gas) of the galaxy, leading to a baryonic Tully Fisher relation (BTFR). The BTFR is valid for a large range of galactic morphologies and masses. This relation links the baryonic content of galaxies to their rotation velocity at large radii (where the rotation curve is flat). The relation presumably is driven by the dark matter halo and thus has to follow from the assumed cosmological model. It is still up to debate whether it is consistent with ΛCDM predictions (McGaugh, 2005).
However, the BTFR only considers the outer part of the rotation curve, neglecting its shape at smaller radii. The specific slope and scatter of the relation can depend on the definition of this velocity value (see, e.g. Lelli et al., 2019).
Lelli et al. (2017) and McGaugh et al. (2016) have investigated the link further, taking into account the full rotation curve shape, and found a radial accelaration relation (RAR), which relates the measured gravitational acceleration at each radius to the acceleration predicted from the baryonic galaxy components. They find that different galaxies follow the same relation over many orders of magnitude in mass. More surprisingly, galaxies of different types, such as LTGs and dwarf spheroidals (dSphs) seem to follow the same relation. The scatter around the RAR is remarkably tight, dominated by observational scaller and leaving little space for intrinsic scatter in the relation. Several empirical relations can be derived from or explained by the RAR.
Due to the local nature of the RAR, it places severe problems for ΛCDM models. Since it gives a way of predicting the total rotational velocity from the baryonic mass distribution at all radii, it cannot be explained by hierarchical structure formation theories without substantial fine-tuning. The authors argue that the radial acceleration relation might be an indicator of a law of nature.
It is of particular interest to see whether the radial acceleration relation is universal for galaxies of different types. Lelli et al. (2017) tried to use the ETG data derived in den Heijer et al. (2015), but, as noted in the introduction, the rotation curves derived in this work consist of only two points for fast rotating ETGs, giving limited insight on the behaviour of ETGs of the RAR.
We place the rotation curves of our three galaxies on the RAR to see whether they lie on it. Following Lelli et al. (2017), we calculate the observed centripetal accelerations ($g_{\rm obs}$) and the ones predicted from the baryonic content ($g_{\rm bar}$) as

$$g_{\rm bar} = v^2_{\rm rot}(R)/R \tag{4.7}$$

and

$$g_{\rm obs} = v^2_{\rm tot}(R)/R. \tag{4.8}$$

Here, $v^2_{\rm rot}$ is the rotation curve we found in chapter 3 and $v^2_{\rm tot}$ is the rotation velocity predicted from the baryon distribution in section 4.4. It is evaluated at the radii for which we have values of $v_{\rm rot}$. The errors on the accelerations are estimated as $\Delta g = \frac{2v}{R}\Delta v$ with Δv calculated as in chapter 3 and section 4.4, respectively, with the difference that in eq. 4.6 the term with the distance dependence is dropped. The uncertainty in distance estimation is accounted for in $\Delta g_{\rm obs}$.

Our results can be seen in Fig. 4.5. On the left side, we present the RAR calculated for a constant mass-over-light ratio of 0.5 as in McGaugh (2016), Lelli et al. (2017). On the

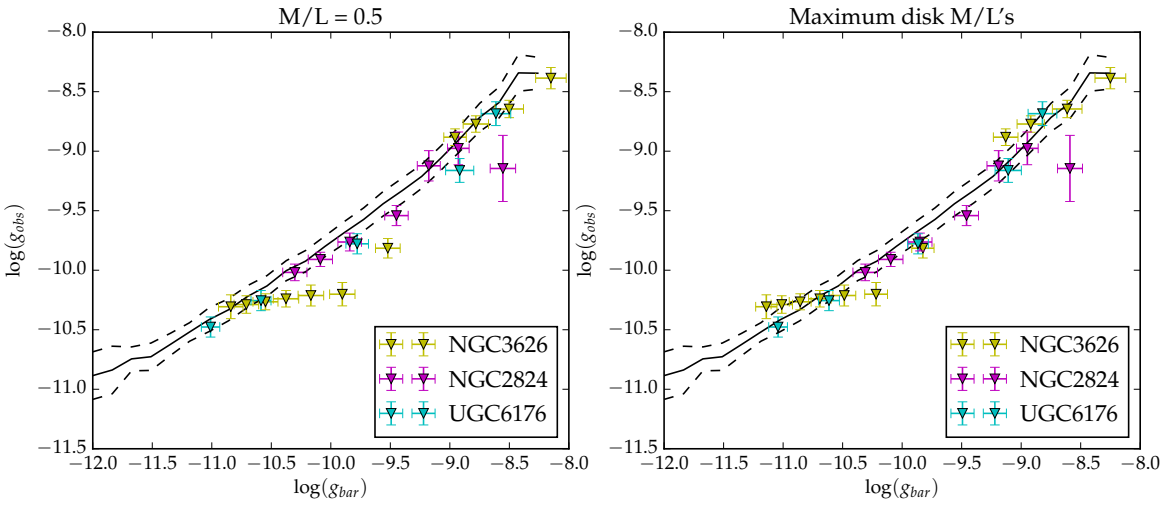

Figure 4.5: The radial acceleration relations derived from our data, using a for constant mass-to-light ratios of 0.5 for all stellar components (left) and the maximal disk M/L's from Tab. 4.4 (right). Black and dashed lines correspond to the mean and 1σ values of the RAR derived for LTGs from the SPARC database.

right - for our best-fit values of M/L as estimated in section 4.5.1. The solid line indicates the radial acceleration relation found for the LTGs in Lelli et al. (2017), the dashed lines show a 1σ deviation from the relation. The data points for our galaxy sample are displayed in colors.

We find that our data points lie on top of the RAR derived for late type galaxies within 1σ. From comparison of the two panels it is clear that the exact location of the points depends on the chosen mass-to-light ratio, although this dependency is reasonably weak. As expected, the agreement is better for our best-fit M/L values.

This finding is very important in the context of galaxy formation. Although we have argued in chapter 4 that the three galaxies in our sample have recently transitioned to being ETG from being spiral, our result hints that for ETGs the shape of the rotation curve at all radii can be predicted from the total baryonic mass by the same relation, as for LTGs. This points again to the possible universality of the radial acceleration relation. A bigger ETG sample including older and more settled early type galaxies is needed to confirm this result.

Chapter 5

Dark matter halo fits

In the previous chapter, we have seen that the baryonic matter distribution predicts a different rotation curve at large radii than we have observed. In this chapter, we attempt at fixing this discrepancy by adding a dark matter halo.

5.1 Halo profiles

As mentioned in the introduction, there are various dark matter models available that can be potentially differentiated with the help of data as they predict different measurable effects. Specifically, they predict different profiles of the dark matter halo.
The dark matter halo has to explain the observed rotation curve. In the inner parts of massive galaxies, the potential of the visible components strongly contributes to the total potential or even dominates it. Meanwhile in the outer parts the visible matter hardly contributes such that the dark matter halo has to come up for nearly all of the total potential to ensure a flat rotation curve. The density of the halo therefore has to change with radius to explain both effects.
We fit several dark matter haloes to our data to see which of the models provides the best fit. The differences between the models as well as their functional forms are explained below.

5.1.1 Isothermal profiles

Pseudo-isothermal profiles are empirically motivated as they provide the most satisfactory fits to galaxy rotation curves (e.g. van Albada, 1985, de Blok, 2008). They can be described by

$$\rho_{\mathrm{PI}} = \rho_c \cdot \frac{1}{1 + r/r_c^2} \tag{5.1}$$

with ρ_c and r_c being density and the radius of the core.
From observations of dwarf galaxies, a good fit to the data is provided if the velocity component induced by the dark matter is growing linearly with radius, which, for a spherical dark matter distribution, implies a constant density core. The pseudo-isothermal profile ensures this feature as well as a constant velocity at large radii.
However, this profile is unphysical, as the enclosed mass diverges with radius.

5.1.2 NFW profiles

The Navarro-Frenk-White profile is derived from dark matter only N-body simulations based on ΛCDM (Navarro et al., 1996). Therefore, this model is not empirical, but motivated by cosmology.
The profile can be described by

$$\rho_{\mathrm{NFW}} = \frac{\delta_c \rho_{\mathrm{crit}}}{r/r_s \cdot (1 + r/r_s)^2}, \tag{5.2}$$

with $\rho_{\mathrm{crit}} = \frac{3H_0^2}{8\pi G}$ the critical density of the Universe and δ_c, the so-called critical overdensity. r_s is the characteristic radius of the halo. One can define the concentration $c_{200} = r_{200}/r_s$ with r_{200} being the radius at which $\delta_c = 200$. The velocity at this radius can be defined to be $v_{200} = 10 H_0\ c_{200}\ r_s$ (with the Hubble constant $H_0 = 73$ km s^{-1}Mpc^{-1}).
The NFW profile fits simulated haloes very well over a large range of masses. However, in the innermost parts it goes as $\rho \sim \mathrm{r}^{-1}$, much steeper than suggested by observations of dwarf galaxies. Profile types such as predicted by NFW are referred to as cuspy. The discrepancy between the observations and the prediction is called the core-cusp problem (de Blok, 2001, 2008, de Blok & Bosma, 2002) .
Using the NFW profile, one implicitly assumes that baryonic feedback effects on the DM halo are negligible, as they are not included in the N-body simulation.

5.1.3 Einasto profiles

As the resolution of simulations improved, it has been seen that the profile shape in the galactic center goes even steeper than suggested by NFW, with a logarithmic slope about -1.3 ± 0.2 at 1 kpc (with the exact value varying from simulation to simulation, see de Blok, 2010). This exacerbates the core-cusp problem.
A profile found to fit the simulations better and for a bigger range of masses than NFW is the Einasto profile (Navarro et al., 2004), described by

$$\rho_E(r) = \rho_s \exp\Big\{ -\frac{2}{\alpha_\epsilon}\Big[\Big(\frac{r}{r_s}\Big)^{\alpha_\epsilon} - 1\Big]\Big\}, \tag{5.3}$$

where α_ϵ is the parameter modeling the variation of the profile slope with radius, ρ_s and r_s are as above.
This profile also is derived from dark matter only N-body simulations, so it also ignores baryonic feedback.

5.1.4 Di Cintio (DC14) profiles

While baryonic feedback on the DM halo is ignored in the simulations used to derive NFW and Einasto profiles, it has often been suggested as a solution to the core-cusp problem.
Indeed, there are various effects by which baryonic matter could influence the DM halo. Stellar and AGN feedback can cause gas outflows large enough to alter the total gravitational potential of the galaxy, causing a re-distribution of the dark matter to a more cored profile (Di Cintio et al., 2014a, Di Cintio et al., 2014b). However, there are also processes steepening the inner DM profile, driven by the gravitational pull of baryons falling and settling in the dark matter halo (for a discussion, see Katz et al., 2014, and references therein). The effectiveness of the dark matter redistribution depends on the ratio between the stellar and the halo mass. If this parameter is too small, there is not enough energy stored in supernovae to impact the DM distribution. On the other hand, if it is too large, the gravitational potential of the stars deepens the total potential in the center enough to not only counteract the outflow effects, but even induce a steeper cusp. There is therefore a parameter range where the core creation is the most effective, found to be around $M_\star/M_{halo} \sim 0.5 \cdot 10^{-3}$ (Di Cintio et al., 2014b).
A DM profile taking into account stellar (but not AGN) outflows was derived by Di Cintio et al. (2014b). It is given by

$$\rho_{\mathrm{DC14}}(r) = \frac{\rho_s}{(r/r_s)^\gamma \big[1 + (r/r_s)^\alpha\big]^{(\beta-\gamma)/\alpha}}, \tag{5.4}$$

with the parameters

$$\begin{aligned} \alpha &= 2.94 - \log\big((10^{X+2.33}) \cdot (10^{-1.08} + 10^{2.29})\big) \\ \beta &= 4.23 + 1.34X + 0.26X^2 \\ \gamma &= 0.06 + \log\big((10^{X+2.56}) \cdot (1 + 10^{-0.68})\big) \end{aligned} \tag{5.5}$$

where $X = \log(M_\star/M_{\mathrm{halo}})$ is the mass ratio and ρ_s and r_s are as above.
For X < -4.1, i.e. $M_\star/M_{\mathrm{halo}} < 8 \cdot 10^{-5}$, the profile effectively reproduces the NFW profile. For X > -1.3 the feedback of AGN, not included in the simulations, is expected to get important, making the DC14 profile potentially inaccurate. For the galaxies in our sample, we find X to be -1.1711, -2.3166, -1.4507 for NGC2824, NGC3626 and UGC6176, respectively, so we can safely use the DC14 model for the last two. NGC2824 is slightly outside

of the applicability range of the model, so the results derived for it have to be taken with caution.
It has to be noted that the mass ratios of our galaxies are rather high, therefore we expect to not see huge outflow effects as they get counteracted by the gravitational pull of the stars in the center. Thus, the DC14 results are expected to be similar to the NFW or Einasto ones.

5.2 ΛCDM expectations

The ΛCDM cosmological model is introduced in section 1.1. The dark matter in this model is cold and not self-interacting. To understand the implications of this model on the shape of dark matter halos, N-body simulations of structure formation are performed. Usually, the baryonic impact on the halo formation is neglected. From statistical analysis of the simulations, predictions can be formulated. One can derive various relationships for the halo and galaxy parameters that can be tested with observations. As effects of the cosmological model on the properties of the DM halos are non-linear, small parameter changes in the models can have non-negligable consequences for the halo structure, hence comparison to the data is crucial.

5.2.1 Concentration mass relation

One can find relationships between different halo parameters. Dutton & Macciò (2014) performed DM-only N-body simulations with different box sizes, studying a huge range of halo masses, from dwarf galaxy hosts to cluster sizes. They find a relationship between the concentration of the halo at a characteristic radius and the halo mass confined within this radius, given by

$$\log c_{200} = a - b \log \left(M_{\rm halo}/[10^{12} h^{-1} M_{\odot}]\right), \tag{5.6}$$

with an intrinsic scatter of 0.11 dex. Here, $h = 10H_0$, and a and b are cosmology-dependent parameters. The parameter values used in this work will be specified in section 5.3.
For our work, this relationship is important in two ways: on one hand, we can check if our galaxies follow it and hence confirm or challenge the results of Dutton & Macciò (2014). On the other, we can impose constraints on the dark matter halos we fit, such that they would follow the relationship a priori, leaving less freedom to the fit parameters to break several parameter degeneracies. This way, the halos we fit are necessarily be sensible in the cosmological context.

5.2.2 Multi-epoch abundance matching

Apart from exploring the properties of the dark matter halos themselves, one can also find relationships between their properties and the ones of the hosted galaxies. There are two main approaches to explore these relationships: one being to model the underlying physical processes of galaxy formation using cosmological hydrodynamical simulations and the other to match observed number of galaxies to dark matter halos from N-body simulations (so-called abundance matching).
Moster et al. (2013) use the second method and employ the multi-epoch abundance matching technique to match halos from two large DM-only N-body simulations to observations of galaxies from several large-scale surveys for a redshift range of $4 < z \leq 0$. In this process,

the functional form of the stellar-to-halo-mass (SHM) relation is assumed to be

$$\frac{M_\star}{M_{\rm halo}} = 2N\Big[\Big(\frac{M_{\rm halo}}{M_1}\Big)^\beta + \Big(\frac{M_{\rm halo}}{M_1}\Big)^\gamma\Big]^{-1}, \tag{5.7}$$

where M_1, N, β and γ are parameters. This relationship was found in previous works (Moster et al., 2010), but the analysis in Moster et al. (2013) improves on those by taking into account the evolution of the galactic stellar mass with time and hence making the matching procedure more self-consistent.
From the galaxy population resulting for the matching, a stellar mass function (SMF) is derived and the fitting parameters of the SHM are adjusted to make it reproduce the observed SMF. This way, the parameters $\log(M_1) = 11.59$, $N = 0.0351$, $\beta = 1.376$ and $\gamma = 0.608$ are found.
Similarly to the concentration-mass relation, we can either try to recover this SHM relation from our data, or impose it on our dark matter halos to make sure that the halos we fit are cosmologically sensible.

5.3 Fitting DM profiles

In fitting the dark matter profiles, we follow Li et al. (2019) and use the same python code as was used in that paper. The fitting is performed with the python MCMC package *emcee* (Foreman-Mackey D. et al., 2013). The code is supplied the total rotation curve and the rotation curves of the individual baryonic components. Additionally, a dark matter rotation curve for one of the profiles described in section 5.1 is calculated. The respective parameters of the dark matter halo, as well as the mass-to-light ratios of the stellar components, the disk inclination, and the galaxy distance, are the parameters of the fit. The priors are Gaussians, which for D and i are centered around the estimated values with a dispersion equal to the calculated error, listed in Tab. 5.1. For the mass-to-light ratios, the central values are chosen to be 0.5 for the disk and 0.55 for the bulge with a standard deviation of 0.1 dex.
For the dark matter halos, the walkers are initialized within the ranges $90 < V_{200} < 100$, $10 < c_{200} < 15$, $0.9 < \alpha_\epsilon < 1.1$. We use two approaches. In one case, we use so-called 'flat' priors. In that case, the DM halo parameters can take any value with no prior knowledge on cosmological scaling relations like the mass-concentration and SHM relations. Loose cuts is applied to keep them in a physically sensible range: $10 < V_{200} < 500$ km/s, $0 < c_{200} < 100$, and for the Einasto profile $0 < \alpha_\epsilon < 2$.
In the other approach, we impose ΛCDM priors on the dark matter parameters that follow from 5.2. For this, we need to rescale the DC14 profile concentration, as it is defined in a slightly different way than the concentration of the NFW and Einasto profiles (Di Cintio et al., 2014b). Following Katz et al. (2017), we adopt

$$c_{200}^{\rm rescaled} = c_{200}^{\rm DC14} \cdot \big[1 + 10^{-5}\ \exp(3.4(X + 4.5))\big]^{-1}. \tag{5.8}$$

For the concentration-mass relation, we use the values $a = 0.830$ and $b = -0.098$ for NFW and DC14, which use the WMAP5 cosmology. For the Einasto profile, only values for the Planck cosmology are available, given by $a = 0.977$ and $b = -0.130$. We also impose an additional constraint on α_ϵ found by Dutton & Macciò (2014), describing the dependence of this parameter on the halo mass. It is given by

$$\alpha_\epsilon = 0.0095\nu^2 + 0.155, \tag{5.9}$$

Parameter	NGC2824	NGC3626	UGC6176
D [Mpc]	39.6 ± 9.9	22.9 ± 2.5	39.3 ± 9.8
i [°]	60 ± 10	55 ± 10	56 ± 2

Table 5.1: Mean values and standard deviations used for prior calculation, derived from the tilted ring analysis. As Δi from Tab. 3.2 is smaller than the difference in i between the CO and HI disks for each of the galaxies, we use the latter value as a standard deviation estimate.

with $\log \nu = -0.11 + 0.146m + 0.0138m^2 + 0.00123m^3$ and $m = \log(M_{\rm halo}/10^{12}h^{-1}M_{\odot})$. This relation has a scatter of 0.16 dex.
The SMH relation is derived for the WMAP7 cosmology. However, as stated in Li et al. (2019), the difference induced by the use of the different cosmology models is nearly negligible and will only play a role for the values of the final distance estimates.

For each fit, we perform at least 2000 burn-in steps and at least 1000 iterations after that. Then, we re-initialize the walkers around the determined best fits values and perform at least 1000 more iterations. We visually check that the chains have converged. In cases when the posterior distributions had complex shapes, we checked that changing the number of the burn-in steps,nor the number of the walkers does not improve the results. These comples posteriour distributions occur in fits with flat priors due to strong parameter degeneracies, which are broken when imposing ΛCDM priors.

5.4 Fit results

We present our results for the dark matter profile fits in Figs. 5.1 to 5.10. We show the fits of every profile to each galaxy in one figure, followed by the corner plots for these 4 fits. We first show the fits for the flat priors, then for the ΛCDM priors on the DM profiles. In Tabs. 5.2 to 5.7 we summarize the retrieved values for the fitting parameters.
We note that the posterior distributions for the flat priors are in general not as well behaved as for the ΛCDM priors. Closer inspection shows that these distributions are multimodal. To get a better estimate of the uncertainty of the dark matter parameters, for future work we would like to decompose these posteriors following Katz et al. (2017).
In general, the fits are good in reproducing the rotation curve both in the inner and the outer parts. We note, that all fits are nearly maximal disk fits, i.e., the inner part of the rotation curve is accounted for mostly by the baryonic component.

5.4.1 NGC2824

For NGC2824, all dark matter profiles achieve fits that look equally well. However, this galaxy is in a mass range for which the DC14 profile might be inaccurate due to unaccounted AGN feedback, so the results for this profile have to be taken with a grain of salt. The retrieved distance, inclination and M/L estimates agree within errors between all profiles and also between fits with and without cosmological constraints, suggesting that these estimates are robust. The recovered M/L values agree with our estimations in chapter 4. Fits without constraints on dark matter tend to place the galaxy a little closer than the literature value. However, all distance estimates are consistent with each other and within error bars.

The χ^2 values suggest that the pseudo-isothermal halo fit describes the data better for the ΛCDM priors, however the differences between the different calculated rotation curves are within the error bars. The pseudo-isothermal corner plots show a strong degeneracy between c_{200} and v_{200}. As for the flat priors, all halo parameters show strong degeneracies due to the mentioned multimodality. This suggests that the rotation curve can be fitted for a large variety of dark matter halo parameters, among which there is a subset of cosmologically reasonable values.

Halo profile	χ^2	D [Mpc]	i [°]	M/L$_{\rm disk}$	M/L$_{\rm bulge}$	M$_{200}$	C$_{200}$	α_ϵ
NFW	6.3	33 ± 8	53 ± 10	0.5 ± 0.1	0.5 ± 0.1	222 ± 14	7 ± 2	
Einasto	–	31 ± 8	54 ± 10	0.5 ± 0.1	0.5 ± 0.1	145 ± 152	9.7 ± 5	0.3 ± 0.6
DC14	6	31 ± 8	54 ± 10	0.5 ± 0.1	0.5 ± 0.1	123 ± 140	23 ± 11	

Table 5.2: Best fit values for the fit parameters for NGC2824. No constraints on the DM halos imposed. The (reduced) χ^2 value is not defined when the number of parameters is bigger than the number of rotation curve points fitted.

Halo profile	χ^2	D [Mpc]	i [°]	M/L$_{\rm disk}$	M/L$_{\rm bulge}$	V$_{200}$	C$_{200}$	α_ϵ
NFW	9	38 ± 8	54 ± 9	0.5 ± 0.1	0.4 ± 0.1	122 ± 34	9 ± 2	
Einasto	–	34 ± 8	55 ± 9	0.5 ± 0.1	0.4 ± 0.1	108 ± 24	13 ± 4	0.19 ± 0.07
DC14	11	40 ± 8	55 ± 8	0.5 ± 0.1	0.42 ± 0.09	119 ± 21	9 ± 2	
pISO	6	33 ± 8	53 ± 9	0.5 ± 0.1	0.5 ± 0.1	197 ± 105	80 ± 20	

Table 5.3: Best fit values for the fit parameters for NGC2824 with ΛCDM constraints.

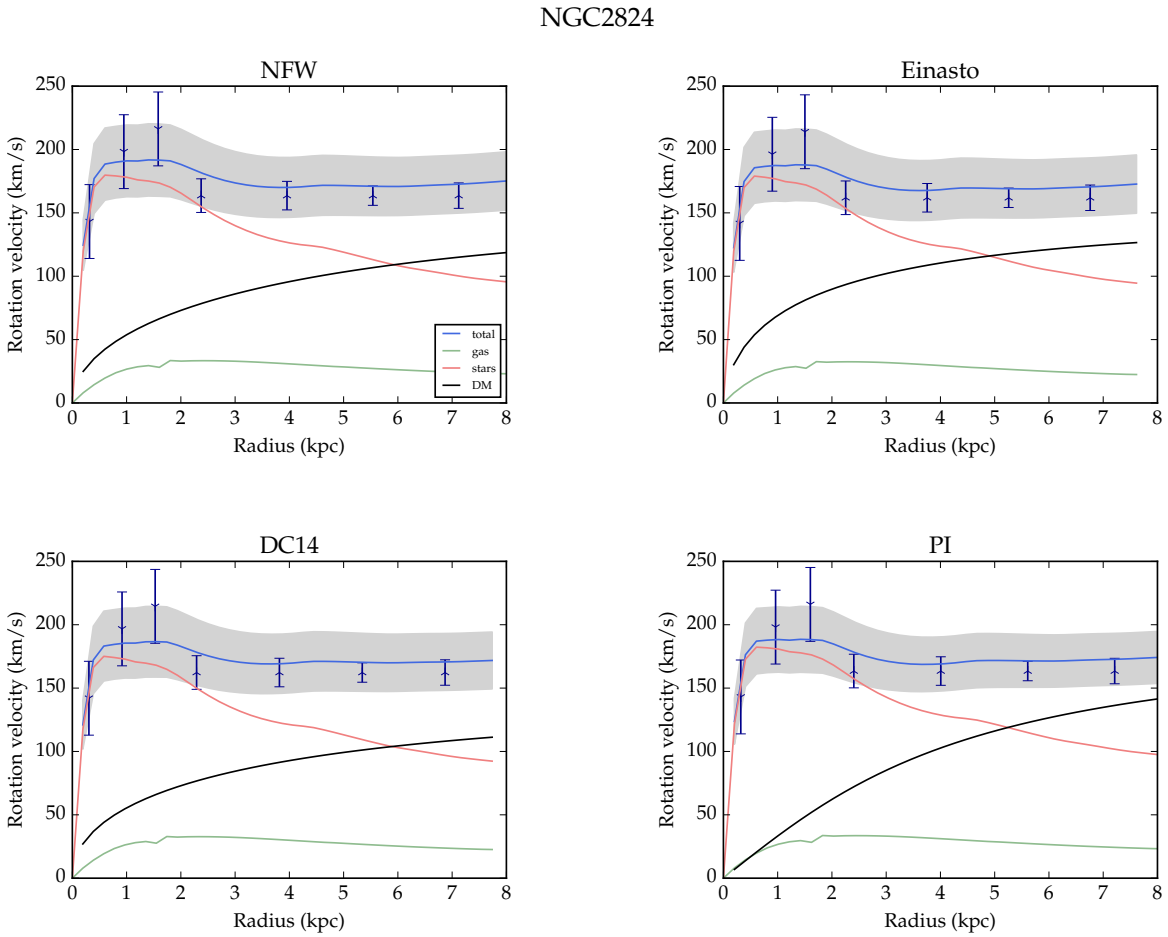

Figure 5.1: Best fits for NGC2824 for the four dark matter profiles with flat priors. Blue − total rotation curve, red − stellar component, green − gaseous components, black − dark matter component. Points show the observed rotation curve with error bars. The gray band indicates 1σ around the predicted rotation curve.

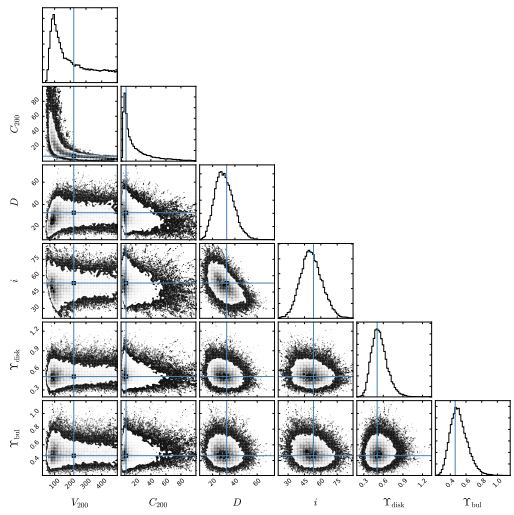

(a) NFW

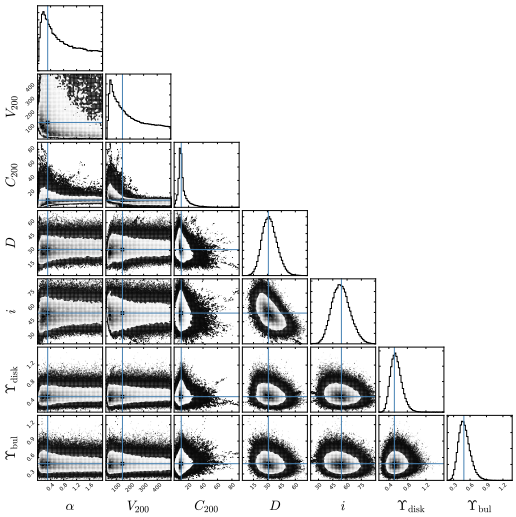

(b) Einasto

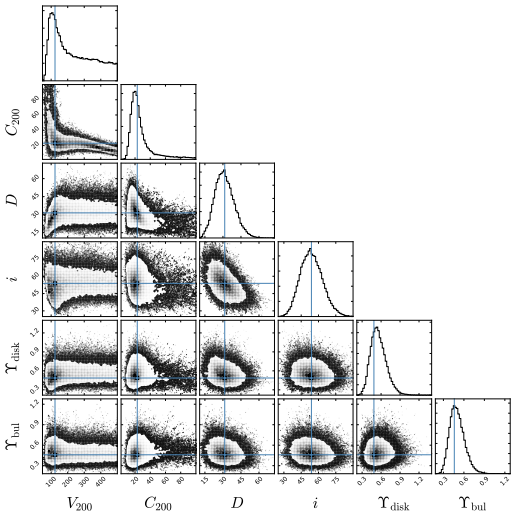

(c) DC14

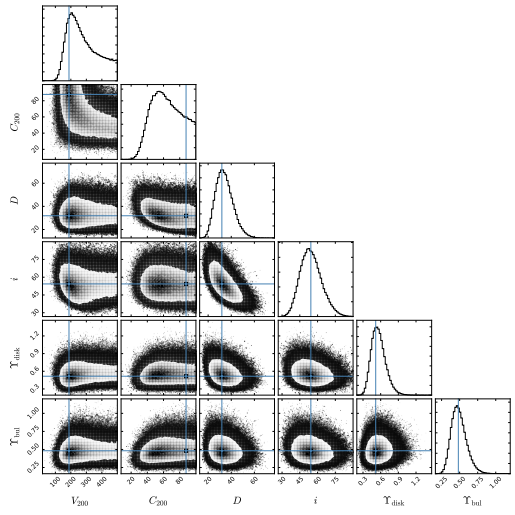

(d) PI

Figure 5.2: Corner plots for NGC2824. Fit with flat priors.

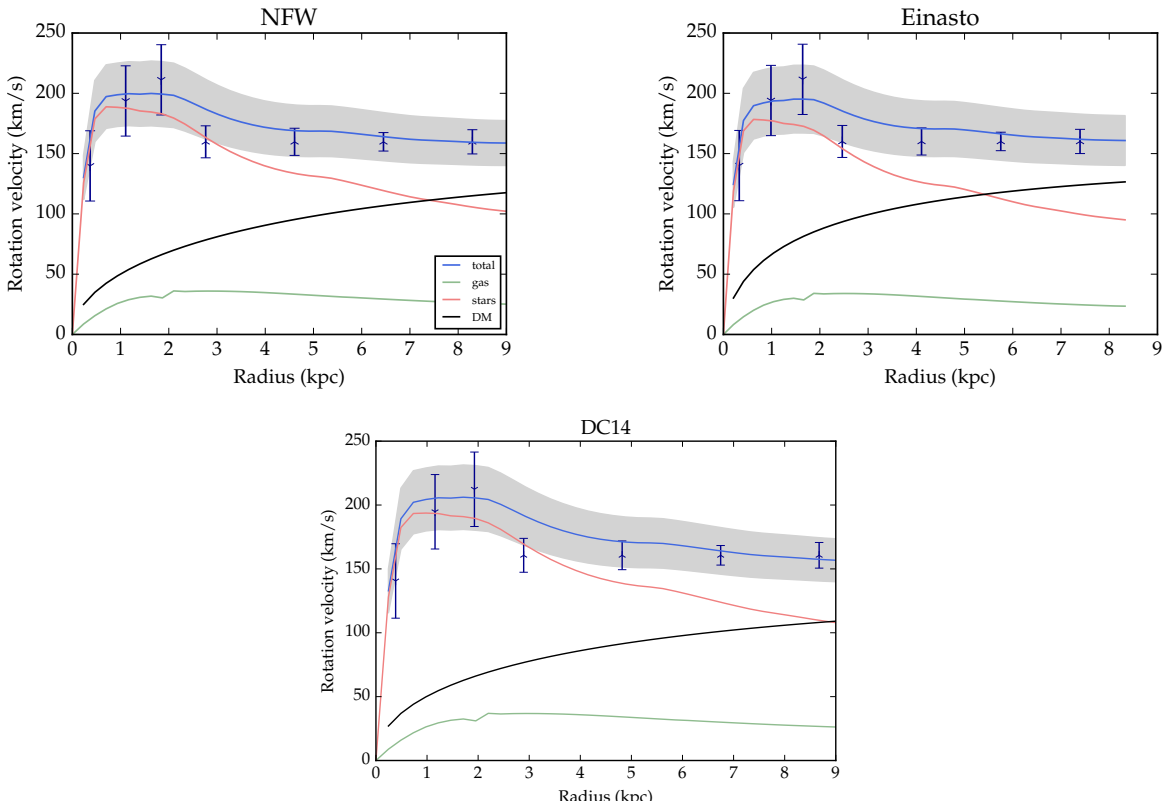

Figure 5.3: Same as 5.1, but with ΛCDM priors (the pseudo-isothermal profile is not shown, as cosmological priors cannot be imposed).

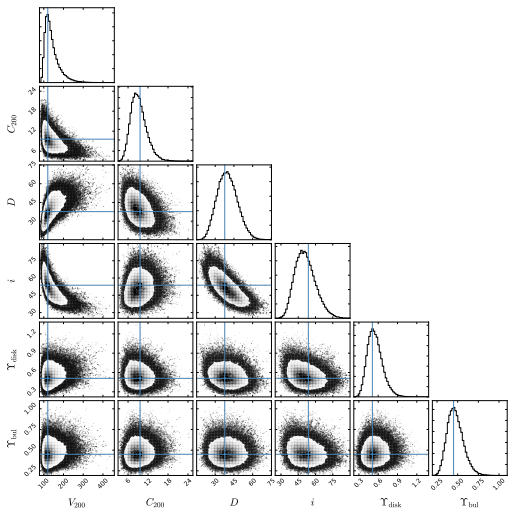

(a) NFW

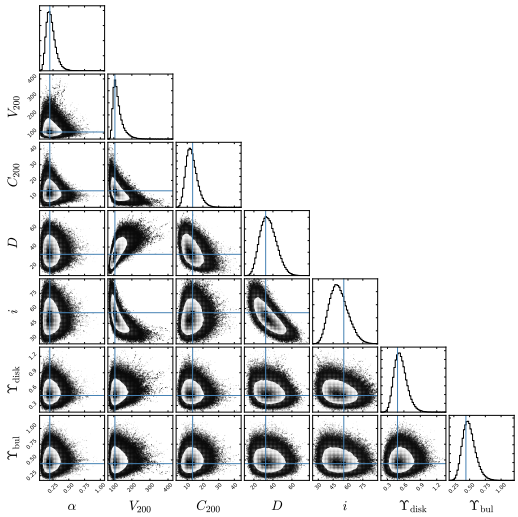

(b) Einasto

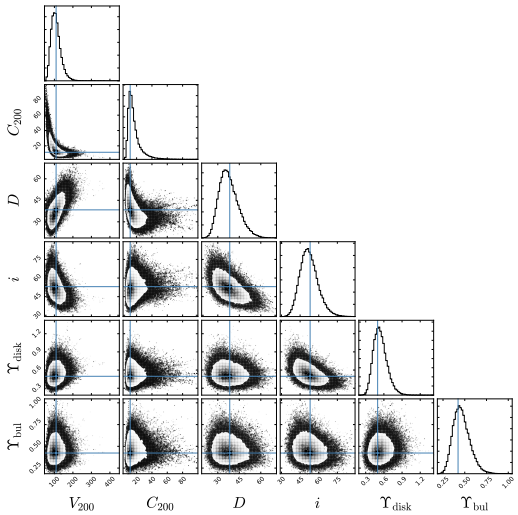

(c) DC14

Figure 5.4: Same as Fig. 5.2, but with ΛCDM priors.

5.4.2 NGC3626

For NGC3626, we find that for the flat priors, the Einasto, DC14 and pseudo-isothermal profiles fit the data, including the rotation curve dip. NFW performs worse in fitting the dip. Constraining the profiles to cosmologically sensible values significantly worsens the fit quality around the dip.
The dip in the rotation curve of this galaxy can give stronger constraints on galactic composition than usual, rising, rotation curves, as the declining rotation velocities at small radii can be explained only by the baryonic components, while the rising rotation velocity in the outer parts is a sensitive measure of the halo profile. As seen from Figs. 5.5 and 5.7, it is best modelled by a cored profile, suggesting the existence of slow rotating ETGs with large cores. The physical origin of such extended cores is interesting: while feedback models as suggested by Di Cintio et al. (2014b) cannot provide them, they might, in the ETG formation picture by Kormendy & Bender (2012), be indicative of recent mergers. This is also consistent with the findings of Silchenko et al. (2010) and Mazzei et al. (2014), that both favor a recent merger scenario of NGC3626.
The estimated galaxy parameters agree amongst the different halo fits. In all fits, the recovered M/L values are slightly higher than our interactive estimates. The recovered distance is consistent with the literature value within error bars, although the estimated mean values tend to be larger.
As for the corner plots, we notice that the isothermal halo concentration is poorly constrained. We also again see strong tails for the halo parameters of all models for the non-constrained case, while with ΛCDM priors the halo posterior distributions are well behaved.

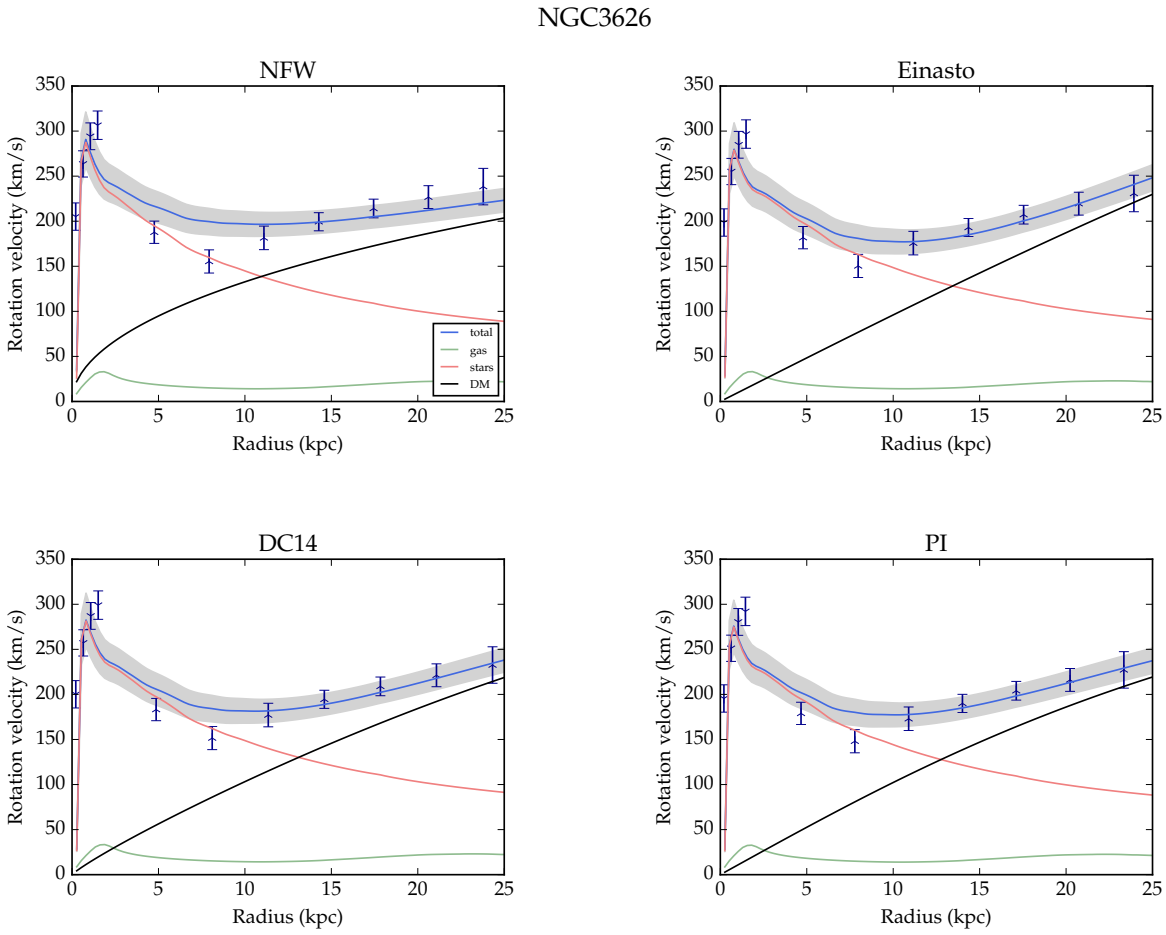

Figure 5.5: Same as Fig. 5.1, but for NGC3626.

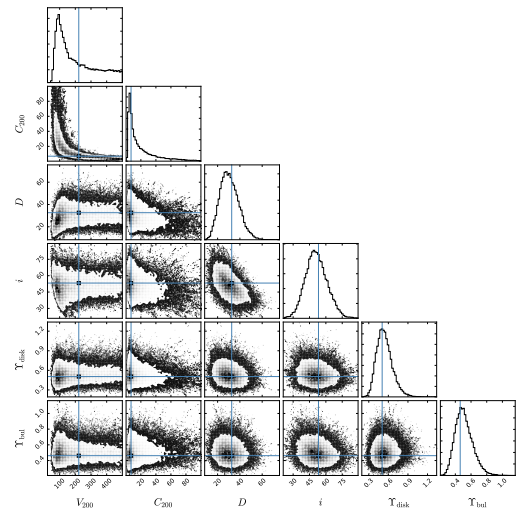

(a) NFW

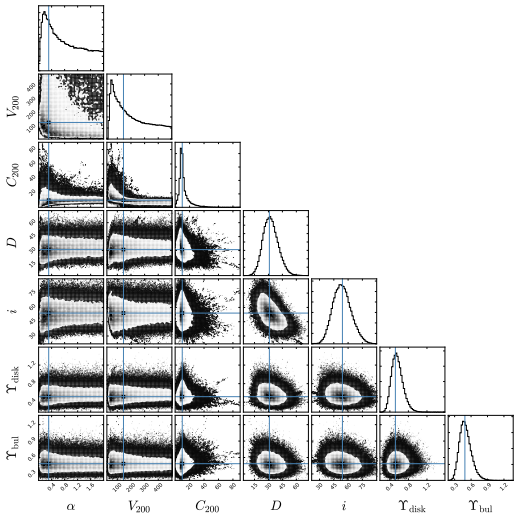

(b) Einasto

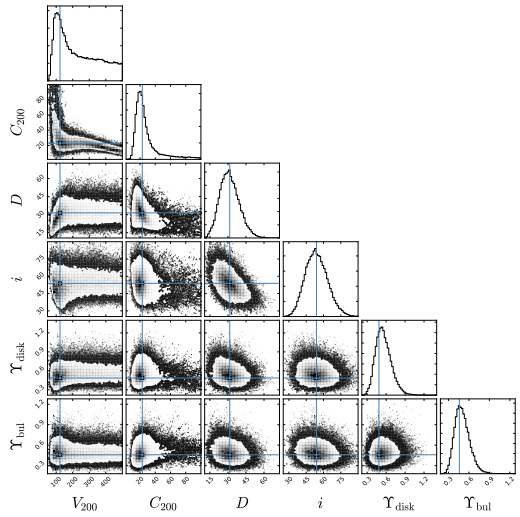

(c) DC14

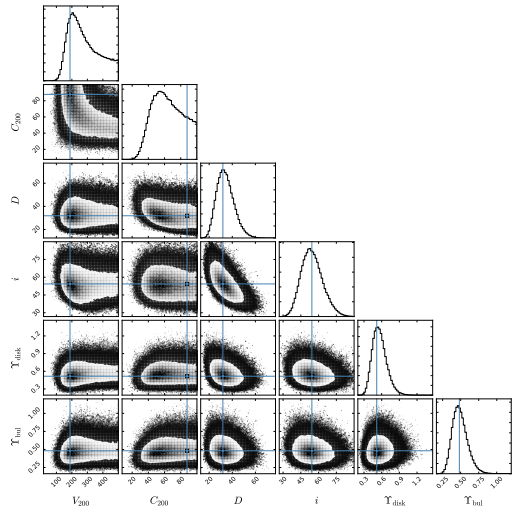

(d) PI

Figure 5.6: Same as Fig. 5.2, but for NGC3626.

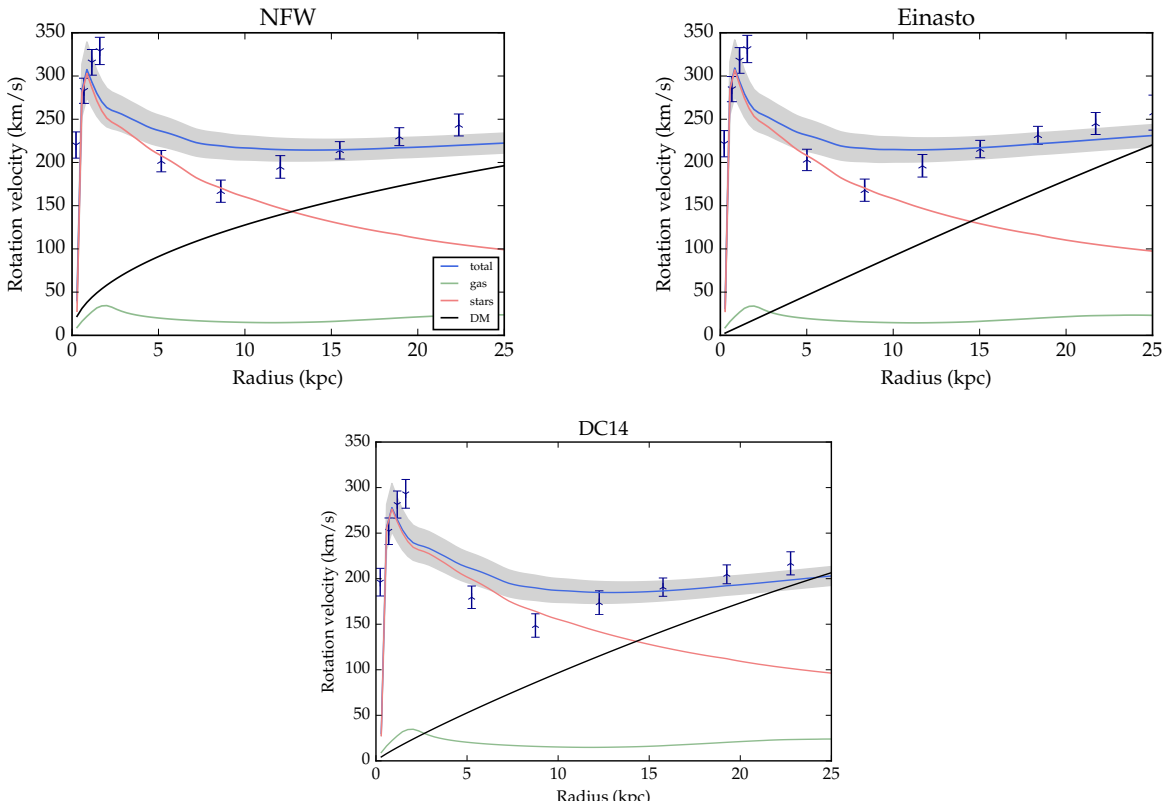

Figure 5.7: Same as Fig. 5.3, but for NGC3626.

Halo profile	χ^2	D [Mpc]	i [°]	M/L$_{\rm disk}$	M/L$_{\rm bulge}$	M$_{200}$	C$_{200}$	α_ϵ
NFW	7	22 ± 3	42 ± 5	0.35 ± 0.07	0.7 ± 0.1	498 ± 91	2 ± 1	
Einasto	7	22 ± 3	44 ± 6	0.39 ± 0.07	0.6 ± 0.1	285 ± 124	6 ± 1	1.9 ± 0.5
DC14	6	22 ± 2	43 ± 5	0.37 ± 0.07	0.6 ± 0.1	373 ± 80	13 ± 2	

Table 5.4: Best fit values for the fit parameters for NGC3626. No constraints on the DM halos imposed.

Halo profile	χ^2	D [Mpc]	i [°]	M/L$_{\rm disk}$	M/L$_{\rm bulge}$	V$_{200}$	C$_{200}$	α_ϵ
NFW	7	23 ± 2	40 ± 5	0.36 ± 0.07	0.6 ± 0.1	213 ± 52	6 ± 1	
Einasto	9	23 ± 2	38 ± 5	0.38 ± 0.08	0.7 ± 0.1	207 ± 61	7 ± 1	0.3 ± 0.1
DC14	7	24 ± 2	44 ± 5	0.36 ± 0.07	0.5 ± 0.1	217 ± 42	10 ± 1	
pISO	6	21 ± 3	45 ± 5	0.38 ± 0.07	0.6 ± 0.1	488 ± 70	24 ± 5	

Table 5.5: Best fit values for the fit parameters for NGC3626 with ΛCDM constraints.

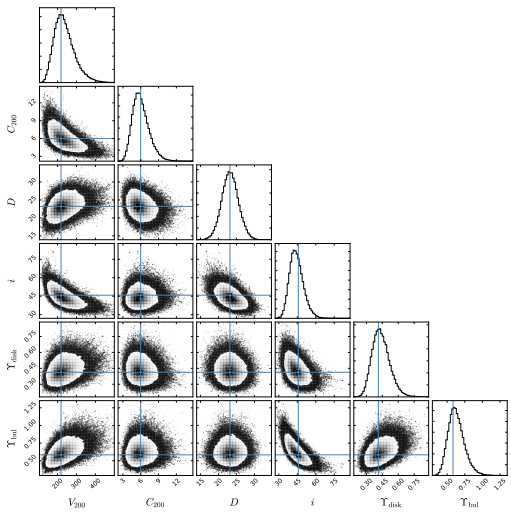

(a) NFW

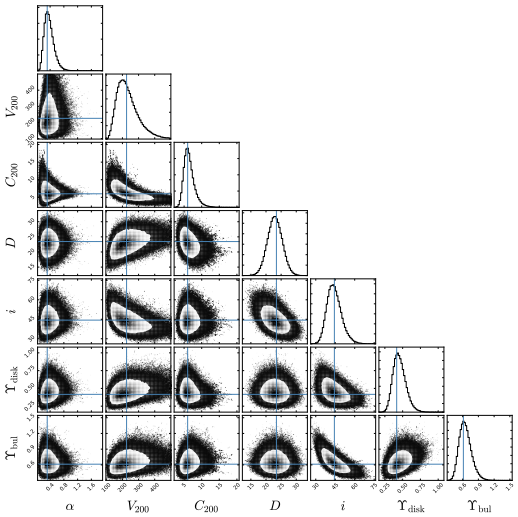

(b) Einasto

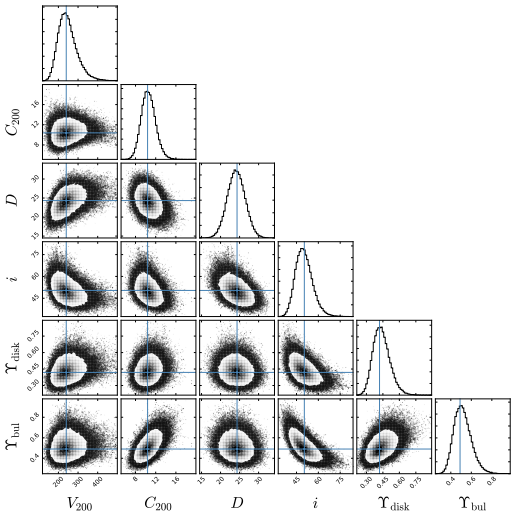

(c) DC14

Figure 5.8: Same as Fig. 5.4, but for NGC3626.

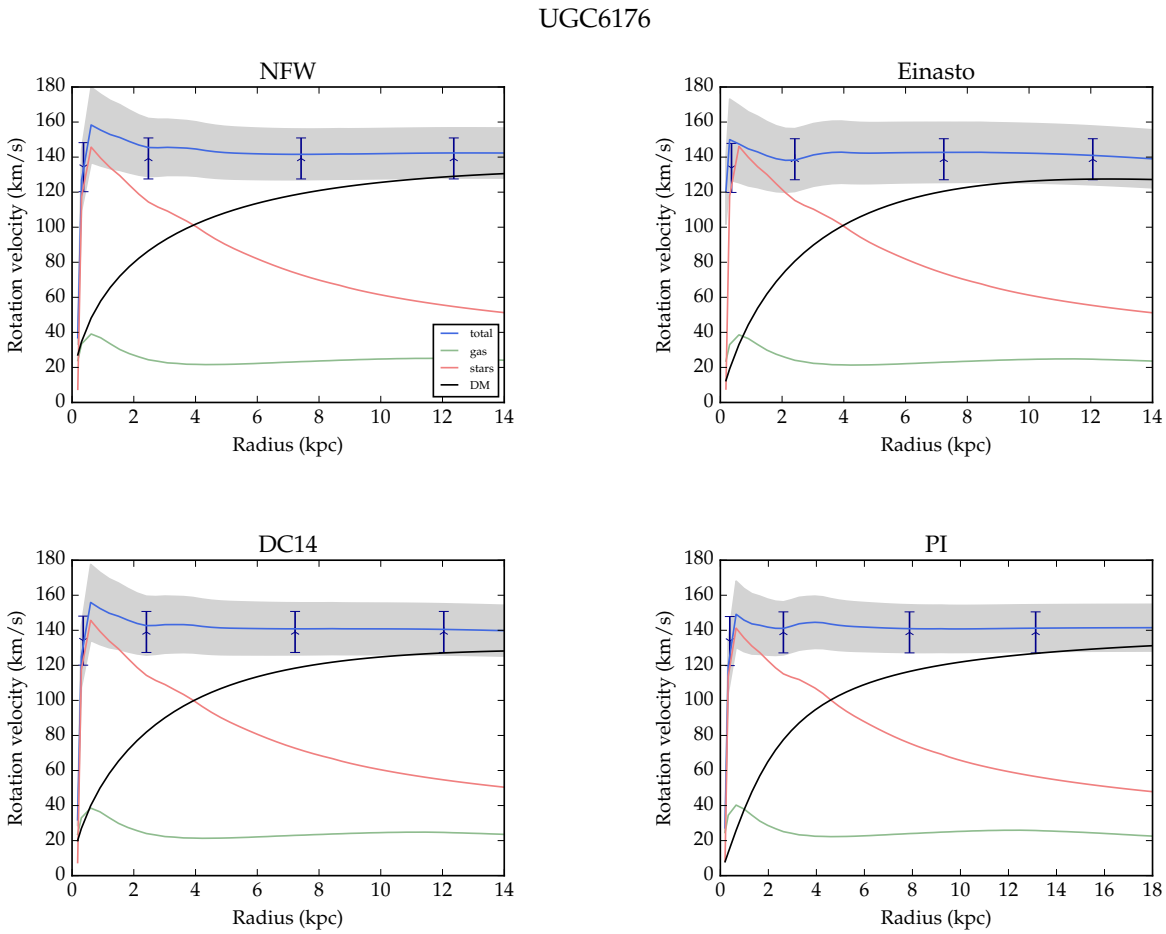

Figure 5.9: Same as Fig. 5.1, but for UGC6176.

5.4.3 UGC6176

For UGC6176, all halo models yield essentially indistinguishable fits to the rotation curve. Interestingly, the recovered galaxy parameters vary strongly. For the flat priors, the distance to the galaxy is strongly underestimated for all halo profiles (ca. 25 ± 5 vs. the literature value of 39 Mpc). The recovered M/L values also differ from our interactive estimates. The fits find the mass-to-light ratios of the disk and the bulge to be very similar, while we estimated M/L_{bulge} to be higher (0.65), and M/L_{disk} to be much smaller (0.3).
Imposing ΛCDM parameters, the distance estimates get close to the literature value for the NFW and DC14 profiles (which in this case are very similar due to the large mass of UGC6176). For the Einasto profile, the distance estimate stays too low. The estimates of the disk M/L get closer to the values we found in chapter 4. Surprisingly, the bulge M/L values decrease.
The corner plots show the same behaviour as for the other galaxies, namely poorly constrained halo parameters for the flat priors and well behaved halo posteriors for the ΛCDM priors. We notice degeneracies between the distance and the M/L values in all cases, which might explain the discrepancy between our fiducial values and the best fit values.

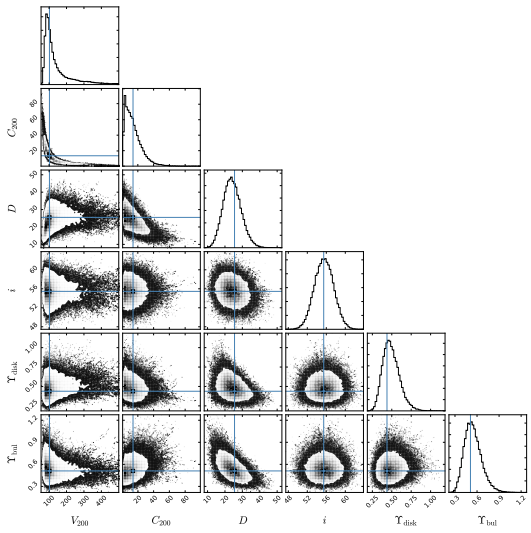

(a) NFW

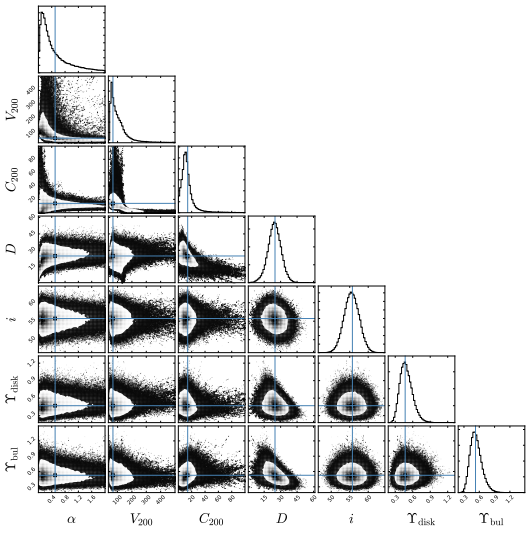

(b) Einasto

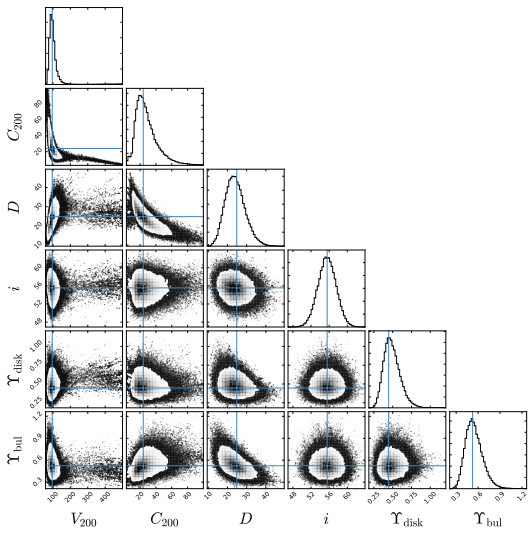

(c) DC14

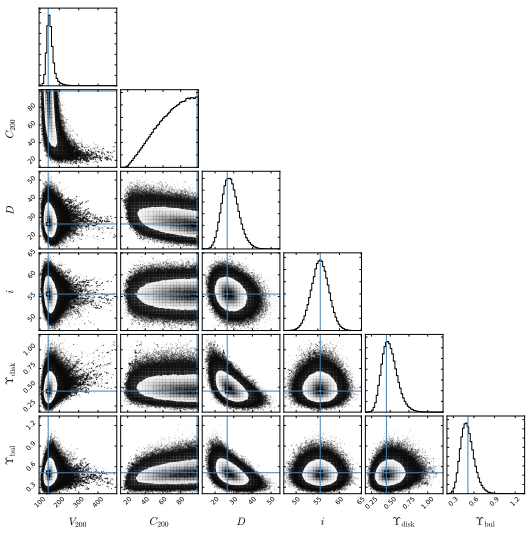

(d) PI

Figure 5.10: Same as Fig. 5.2, but for UGC6176.

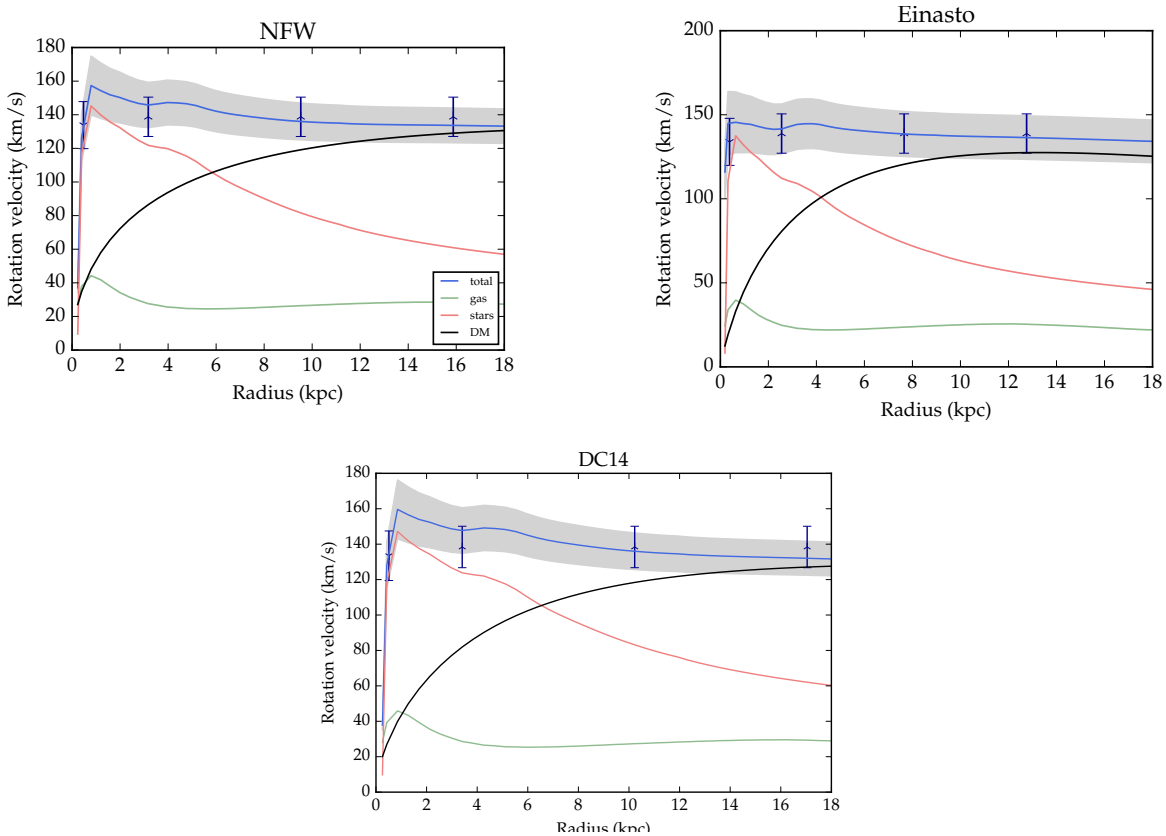

Figure 5.11: Same as Fig. 5.3, but for UGC6176.

Halo profile	χ^2	D [Mpc]	i [°]	M/L$_{\rm disk}$	M/L$_{\rm bulge}$	M$_{200}$	C$_{200}$	α_ϵ
NFW	–	26 ± 5	55 ± 2	0.4 ± 0.1	0.5 ± 0.1	102 ± 61	14 ± 10	
Einasto	–	25 ± 6	56 ± 2	0.5 ± 0.1	0.5 ± 0.1	68 ± 47	14 ± 7	0.5 ± 0.4
DC14	–	25 ± 5	56 ± 2	0.4 ± 0.1	0.5 ± 0.1	96 ± 18	24 ± 13	

Table 5.6: Best fit values for the fit parameters for UGC6176. No constraints on the DM halos imposed.

Halo profile	χ^2	D [Mpc]	i [°]	M/L$_{\rm disk}$	M/L$_{\rm bulge}$	M$_{200}$	C$_{200}$	α_ϵ
NFW	–	31 ± 5	56 ± 2	0.43 ± 0.09	0.46 ± 0.09	101 ± 8	10 ± 2	
Einasto	–	25 ± 4	56 ± 2	0.42 ± 0.09	0.5 ± 0.1	93 ± 8	14 ± 3	0.23 ± 0.06
DC14	–	34 ± 5	56 ± 2	0.43 ± 0.08	0.44 ± 0.08	104 ± 9	12 ± 3	
pISO	13	27 ± 4	56 ± 2	0.4 ± 0.1	0.5 ± 0.1	142 ± 16	99 ± 21	

Table 5.7: Best fit values for the fit parameters for UGC6176 with ΛCDM constraints.

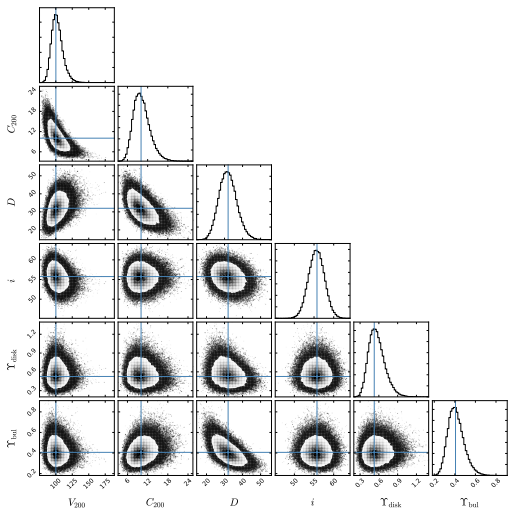

(a) NFW

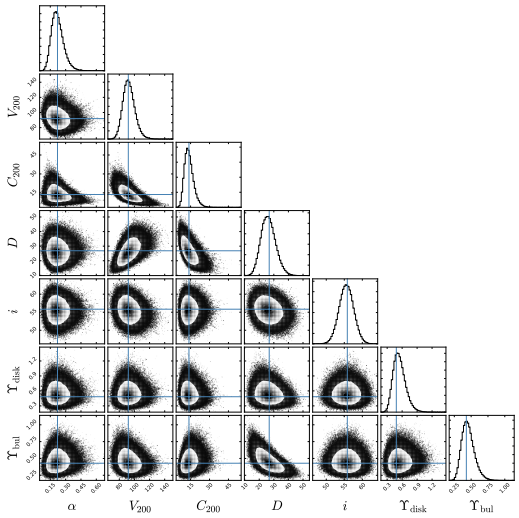

(b) Einasto

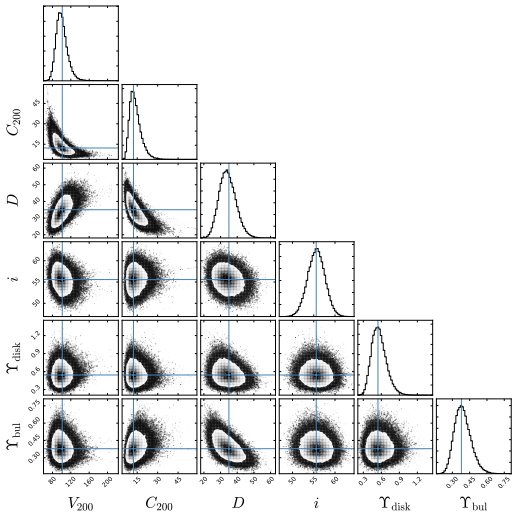

(c) DC14

Figure 5.12: Same as Fig. 5.4, but for UGC6176.

5.5 Comparison with ΛCDM expectations

In this section, we compare the halo parameters we derived from the fits to the expectations from ΛCDM we outlined in section 5.2. We will only discuss the NFW, Einasto and DC14 profiles in this section, as no cosmological parameters can be imposed on the (cosmologically non-motivated) pseudo-isothermal profile.
First, we double-check whether the halos derived from fits with imposed ΛCDM priors reproduce the relationships from 5.2, which we would expect unless our fitting procedure malfunctioned. We present the stellar-to-halo-mass relations and concentration-mass relations derived for our galaxies in the top and bottom panels of Fig. 5.13, respectively.
We see that for the SHM relation, NGC3626 is an outlier for all three dark matter profiles. This is likely caused by the dip in its rotation curve, which puts a hard constraint on the dark matter component.
The concentration-mass relation is reproduced within errorbars for the NFW and Einasto profiles. We note that the data seems to lie off the relationship for the DC14 profile, which overpredicts the concentration of NGC3626 and UGC6176.
In Fig. 5.14, we show the same relationships derived from our fits without priors on the halos. We find, that also in this case, the literature curves are reproduced fairly well. This is less expected than for the previous case, and shows that the halos chosen by the DM prior-less fit are still in the cosmologically sensible regime. An exception, again, is the concentration-mass relation for the DC14 profile, where the concentration is systematically overestimated.
As noted in section 5.4, the posterior distributions of the dark matter parameters for the flat prior fit are multimodal, so a sensible assignment of error bars is very hard. We cannot advocate calculating the σ value, as it would have no physical meaning, and therefore display the 95 percentiles in Fig. 5.14, to show where the bulk of the estimated values lies. A better approach would be to decompose the posterior distribution and display the mean value and the error bars only for the part with more counts. We leave this to future work.

Lastly, in Fig. 5.15 we compare our results from the fit with ΛCDM priors to the ones of Li et al. (2019) derived for the SPARC sample. We find that our halos follow the same general relations for the characteristic radius and density as functions of the galaxy luminosity as the other galaxies in SPARC. Therefore, our galaxies live in the same halos as LTGs, which is another indication that they have been spirals and quenched star formation only recently. This statement is also consistent with the fact that our galaxies follow the LTG radial acceleration relation. We note that the values of $\log_{10}(r_s \cdot \rho_s)$ estimated for our galaxies are on the high side, but still consistent within error bars with the SPARC sample.

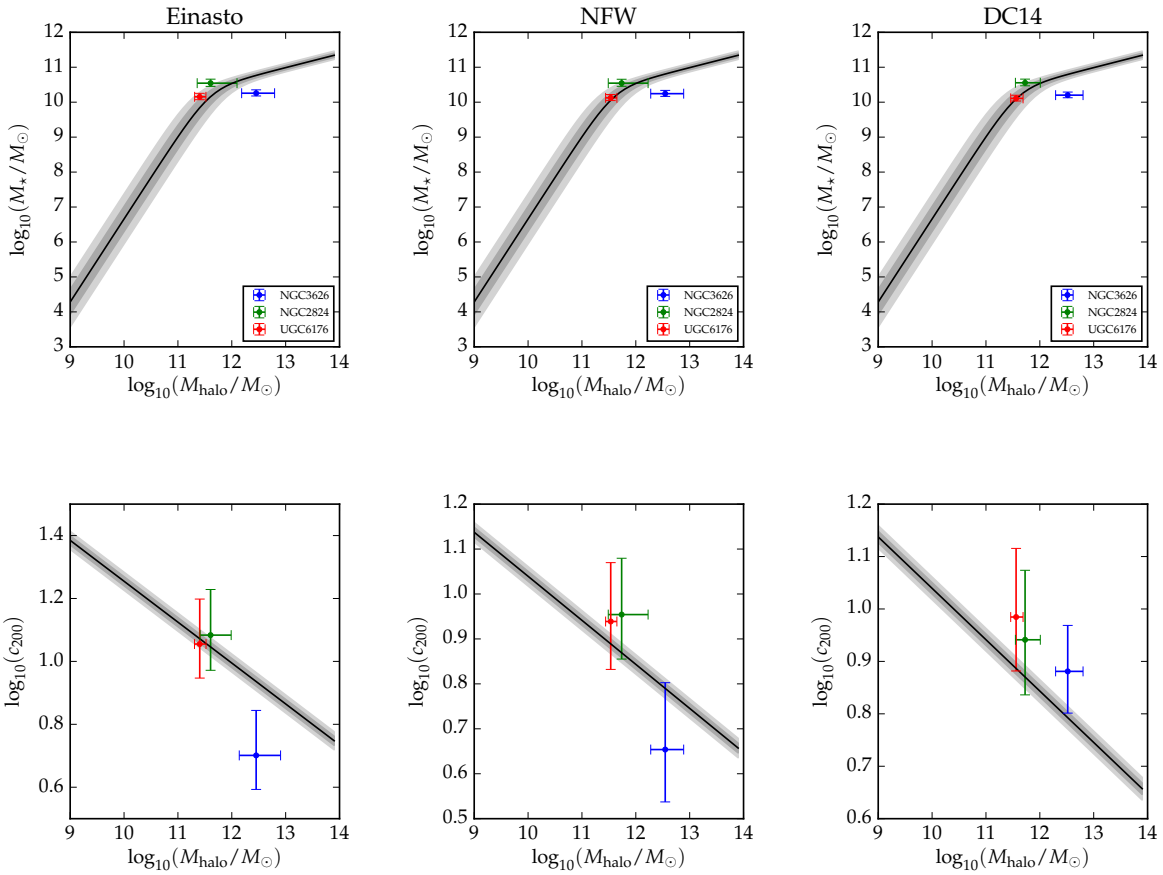

Figure 5.13: Stellar-to-halo-mass relation (upper panel) and concentration-mass relation (lower panel) for our results from fitting with ΛCDM priors imposed. The black solid line and the grey shaded areas show the literature relations together with their intrinsic scatter. The errorbars on our data points correspond to 1σ.

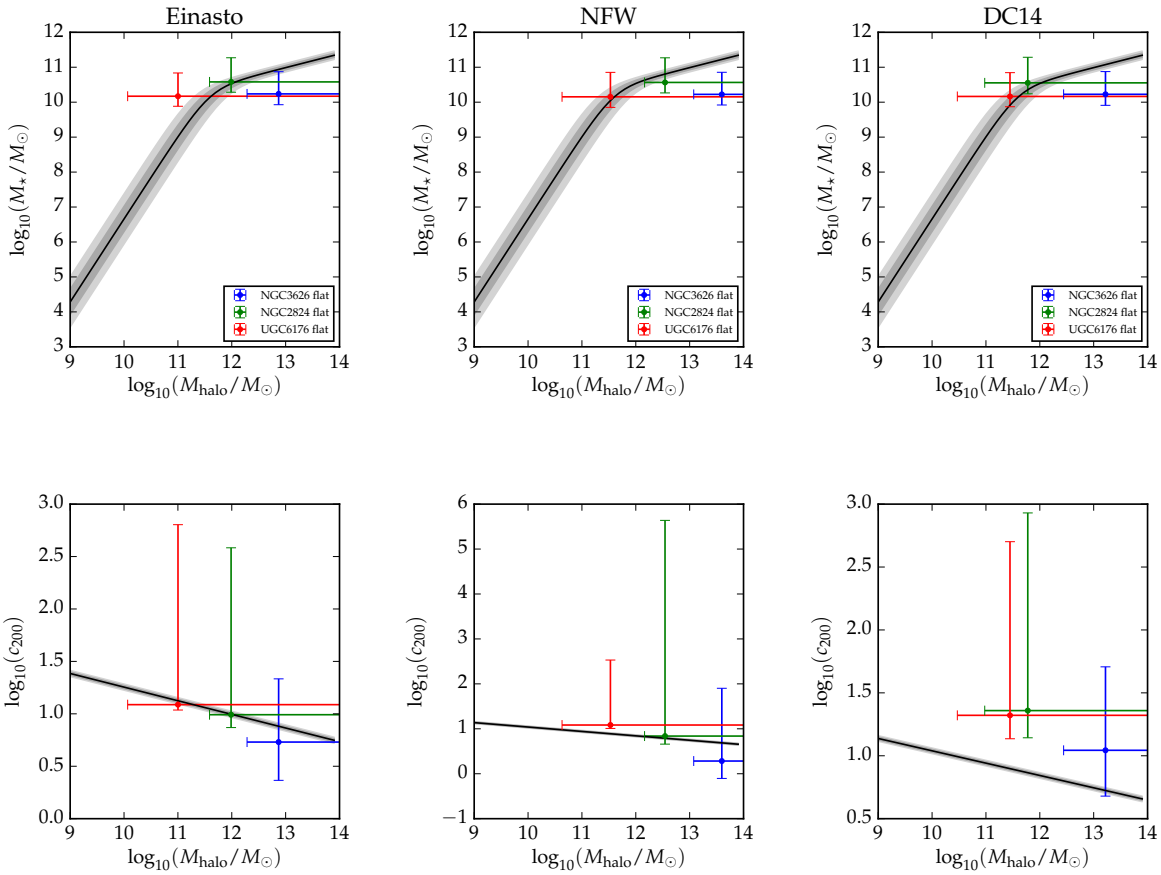

Figure 5.14: Same as Fig. 5.13, but for fit without imposed constraints on DM halos. In this case, the errorbars on the data are 95 percentiles, as the posterior distributions are not well-behaved enough to be able to reasonably assign σ intervals.

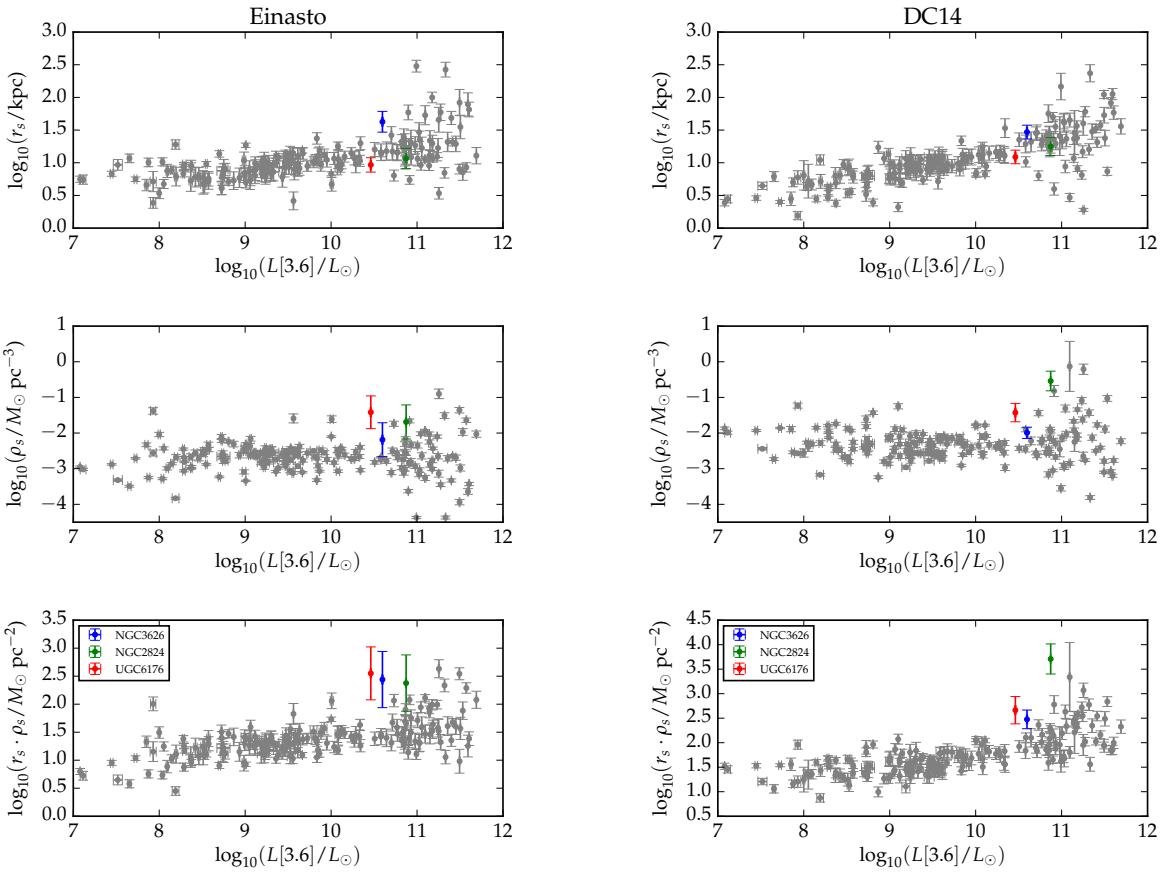

Figure 5.15: Comparison of the general dark matter halo parameters of our galaxies with the SPARC sample (grey dots) from Li et al. (2019).

Chapter 6

Summary and outlook

In this thesis, we have investigated the dynamical properties of the three early type galaxies NGC3626, NGC2824 and UGC6176.
We have derived their intensity maps and velocity fields from HI and CO observations. Then, we proceeded to derive the rotation curves of these galaxies using two different methods (*rotcur* + *galmod* and ^{3D}Barolo) and showed that the results were consistent. The rotation curves we found are flat in the outer parts.
We have calculated the total baryonic mass of the galaxies from their stellar and gas luminosities and showed that these components alone predict a rotation curve decreasing at high radii. Therefore, we trace the dark matter haloes of these early-type galaxies. Based on the low mass-to-light ratio values we found in the maximum disk fits, we conclude that our three objects have recently transitioned to the early type, having evidence of recent or even ongoing star formation. This hypothesis is backed up by findings of Yildiz et al. (2017), based on optical and UV imaging, and Silchenko et al. (2010) in the case of NGC3626.
We have found that our three galaxies follow the same radial acceleration relation as late type galaxies and dwarf spheroidals from the SPARC database. This is another indication that the RAR is a universal relationship, independent of morphological type, gas content, or star-formation activity.
Finally, we have fitted four different dark matter profiles to each of our galaxies. We found that adding dark matter, we can model the rotation curves at all radii. In all cases, the best fits are given by the maximum disk, so the dark matter contribution plays a role only at large radii.
The retrieved dark matter parameters are poorly constrained when left entirely free, leading to broad and multimodal posterior distributions. Although the best-fit values are in overall agreement with expectations from cosmology, it is hard to properly quantify this, as a different analysis of the posteriors is needed to calculate sensible errors on the parameters. We leave this to future work.
Imposing ΛCDM constraints on the dark matter halo before the fitting, we find rotation curves that reproduce the observations just as well as the unconstrained halos, while the posterior distributions of the halo parameters are much better behaved.
An exception is NGC3626. The rotation curve of this galaxy shows a prominent dip, which cannot be produced by a dark matter contribution to the potential and hence is a purely baryonic feature, helping to break the degeneracies between baryonic and DM contributions. For this galaxy, the cosmologically motivated rotation curves struggle to reproduce both the dip feature and the rising rotation curve at larger radii. The best fit is achieved by a cored DM halo, suggesting that large cores may exist also in slow-rotating Early Type galaxies. Consistently with Kormendy & Bender (2012) and Silchenko et al. (2010), the core might be a result of a recent merger of NGC3626 with a smaller galaxy.

In future work, we would like to perform a fit of our galaxy sample to the mean radial acceleration relation derived from the SPARC database. It is of great interest to see if the recovered values of the distances, inclinations and mass-to-light ratios will be physical and close to our previous estimates. Should this be the case, it would point to another success of MOND as a phenomenological description of galactic dynamics.
The analysis of a bigger ETG sample would yield statistically more valuable results. In the ALTAS^{3D} sample there are another 15 ETGs with outer HI disks, but they do not have inner CO disks. One could, however, use Hα velocity fields to trace the inner kinematics and combine it with the outer HI kinematics.
Also, some ETGs from the ATLAS^{3D} sample, including NGC2824, have been observed with higher resolution by ALMA. It is desirable to repeat the analysis of NGC2824 using the ALMA data.

Bibliography

Papers

Alatalo K., Davis T. A., Bureau M. et al., 2013, MNRAS, 432, 3, 1796-1844

Bahcall J. N., 1982, Astrophysical Journal, 1 , 276, p. 156-168

Bender R., 1988, Astron. Astrophys. 193, L7-L10

Bender R., Surma P., Doebereiner S., Moellenhoff C., Madejsky R., 1989, Astron. Astrophys. 217, 35-43

Bennett C. L., Halpern M., Hinshaw G. et al., 2003, The Astrophysical Journal Supplement Series, 148, 1, pp. 1-27

Bershady, M. A., Verheijen, M. A. W., Westfall, K. B. et al. 2010b, Astrophysical Journal, 716, 234

Bertone G. & Hooper D., 2016, Reviews of Modern Physics, 90, 4, id.045002

Bolatto A. D., Wolfire M., Leroy A. K., 2013, Annual Review of Astronomy and Astrophysics, 51, 1, pp. 207-268

Borgani S. & Kravtsov A., 2011, Advanced Science Letters, 4, 2, pp. 204-227

Bosma, A., 1978, PhD Thesis, University of Groningen

Boylan-Kolchin M., Springel V., White S. D. M., 2009, MNRAS, 398, 11501164

Bullock J. S., Boylan-Kolchin M., 2017, Annual Review of Astronomy and Astrophysics, 55, 1, pp. 343-387

Burbidge E.M., Burbidge G.R., Prendergast K.H., 1959, Astrophysical Journal, vol. 130, p.739

Cappellari M., Emsellem E., Krajnović D., 2011, MNRAS, 413, 2, 813-836

Cappellari M., 2016, Annu. Rev. Astron. Astrophys., 54, 1-67

Casertano, S., 1983, MNRAS, 203, 735-747

Ciardi B. & Ferrara A., 2005, Space Sci. Rev., 116, 625

Ciri, R., Bettoni, D., & Galletta, G. 1995, Nature, 375, 661

Clark P. C., Glover S. C. O., 2015, MNRAS, 452, 2, 2057-2070

Clowe D., Gonzalez A., & Markevitch M., 2004, Astrophysical Journal, 604, 596

Dame T. M., Hartmann D. & Thaddeus P., 2001, Astrophysical Journal, 547, 792

Davies R. L., Efstathiou G., Fall S. M., Illingworth G. & Schechter P. L., 1983, Astrophysical Journal, 266, 41

de Blok W. J. G., McGaugh S. S., Rubin V. C., 2001, The Astronomical Journal, 122, 5, pp. 2396-2427

de Blok W. J. G., & Bosma A., 2002, A&A, 385, 816

de Blok W. J. G., Walter F., Brinks E. et al., 2008, The Astronomical Journal, 136, 2648

de Blok W. J. G., 2010, Advances in Astronomy, Article ID 789293

den Heijer M., Oosterloo T. A., Serra P., et al. 2015, A&A, 581, A98

de Lapparent V., Geller M. J., Huchra J. P., 1991, Astrophysical Journal, 369, 273.

Di Cintio A., Brook C. B., Macciò A. V. et al., 2014a, MNRAS, Vol. 437, 415-423

Di Cintio A., Brook C. B., Dutton A. A. et al., 2014b, MNRAS, 441, 2986-2995

Dickman R. L., Snell R. L., Schloerb F. P.,1986, Astrophysical Journal v.309, p.326

Di Teodoro & Fratenalli, 2015, MNRAS, 451, 3021-3033

Dodelson S., 2011, International Journal of Modern Physics D, 20, 14, 2749-2753

Doroshkevich A. G., Novikov I. D., 1964, Soviet Physics Doklady, Vol. 9, p.111

Dutton, A. A., Macciò, A. V., 2014, MNRAS, 441, p.3359-3374

Einasto J., 1972, PhD thesis, Tartu University, Tartu

Einasto J., 1974, Galactic Models and Stellar Orbits (Invited Lecture), in Stars and the Milky Way System, ed. L. N. Mavridis, 291

Einasto J., 2009, eprint arXiv:0901.0632

Einstein A., 1905, Annalen der Physik, 322, 10, 891-921

Emsellem E., Cappellari M., Krajnovič D. et al., 2007., MNRAS 379, 401-417

Ewen H. I., Purcell E. M., 1951, Nature, 168, 4270, pp. 356

Faber S. M., Tremaine S., Ajhar E. A. et al., 1997., Astronomical Journal, 114, 1771

Famaey B., McGaugh S. S., 2012, Living Reviews in Relativity, 15, 1, article id. 10, 159

Ferrarese L., van den Bosch F. C., Ford H. C,. Jae W., O'Connell R. W., 1994., Astronomical Journal, 108, 1598-1609

Foreman-Mackey D., Hogg D. W., Lang D., Goodman J., 2013, PASP, 125, 306

Fratenali F., Sancisi R., Kamphuis P., 2011, A&A, 531, A64

Gentile G., Salucci P., Klein U., Vergani D., Kalberla P., 2004, MNRAS, 351, 3, pp. 903-922

Guth A. H., 1981, Physical Review D (Particles and Fields), 23, 2, pp.347-356

Haynes M. P., Jore K. P., Barrett E. A. et al., 2000, The Astronomical Journal, 120, 703

Hagen J. H. J., Helmi A., 2018, Astronomy & Astrophysics, 615, A99, 9 pp.

Hubble E. P., 1926., The Astrophysical Journal, 64, 321:369

Illingworth G., 1977, Ap. J. Let., 218, L43-L47

Jackson N., 2008, Jets from Young Stars II, Lecture Notes in Physics, Vol. 742. Springer-Verlag Berlin Heidelberg, p. 193

Jore K. P., Haynes M. P., Broeils A. H., 1996, American Astronomical Society, 189th AAS Meeting, id.68.04; Bulletin of the American Astronomical Society, Vol. 28, p.1359

Kapteyn J. C., 1922, The Astrophysical Journal, 55, 302

Katz H., McGaugh S. S., Sellwood J. A. & de Blok W. J. G., 2014, MNRAS 439,1897-1908

Katz H., Lelli F., McGaugh S. S., Di Cintio A. et al., 2017, MNRAS, 466, 1648-1668

Kent, S. M.; 1986; Astronomical Journal, Vol. 91, p. 1301-1327

Komatsu E., Dunkley J., Nolta M. R. et al., 2009, The Astrophysical Journal Supplement, 180, 2, pp. 330-376

Kormendy J., & Bender R., 2012, The Astrophysical Journal Supplement Series, 198:2 (40pp)

Kormendy J., & Bender R., 1996., Astrophysical Journal Letters, 464, L119

Kormendy J., Fisher D. B., Cornell M. E., Bender R., 2009, The Astrophysical Journal Supplement, 182, 1, pp. 216-309

Kramer E. D., Randall L., 2016, Astrophysical Journal, 824, 2, 116, 19 pp

Laurikainen E., Salo H., & Buta R. 2005, MNRAS, 362, 1319

Lelli F., Verheijen M. & Fraternali F., 2014, MNRAS, 445, 1694-1712

Lelli F., McGaugh S. S. & Schombert J. M., 2016, The Astronomical Journal, 152:157

Lelli F., McGaugh S. S., Schombert J. M. & Pawlowski M. S., 2017, The Astrophysical Journal, 836:152

Lelli F., McGaugh S. S., Schombert J. M., Desmond H. & Katz, H., 2019, MNRAS, 484, p.3267-3278

Li P., Lelli F., McGaugh S. S., Starkman N. & Schombert J. M., 2019, MNRAS, 482, 5106-5124

Linde A. D., 1982, Physics Letters B, 116, 5, p. 335-339.

Maddox S. J., Efstathiou G., Sutherland W. J., Loveday J., 1990, MNRAS, 242, 43P.

Markevitch M., Gonzalez A. H., David L., et al. 2002, Astrophysical Journal, 567, L27

Mazzei P., Marino A. et al., 2014, Advances in Space Research, 53, 6, p. 950-962

McGaugh S. S., Schombert J. M., Bothun G. D. & de Blok W. J. G., 2000, The Astrophysical Journal, 533, pp. L99-L102

McGaugh S. S., 2005, Astrophysical Journal, 632, p. 859-871

McGaugh S. S., 2016, Astrophysical Journal, 816, 42

McGaugh S. S., Lelli F., Schombert J. M., 2016, Physical Review Letters, 117, 20, id.201101

Milgrom M., 1983, Astrophysical Journal, Part 1 (ISSN 0004-637X), vol. 270, p. 365-370

Moster B. P., Somerville R. S., Maulbetsch C. et al., 2010, Astrophysical Journal, 710, 903

Moster B. P., Naab T., White S. D. M. , 2013, MNRAS, 428, p.3121-3138

Mukhanov V. F., 2004, International Journal of Theoretical Physics, 43, 3, pp. 669-693

Mukhanov V. F., 2016, Physics-Uspekhi, 59, 10, 1021-1027

Navarro J. F., Frenk C. S. & White S. D. M., 1996, Astrophysical Journal, 462, p.563

Navarro J. F., Hayashi E., Power C. et al., 2004, MNRAS, 349, 1039-1051

Oort J. H., 1932, Bulletin of the Astronomical Institutes of the Netherlands, 6, p.249

Oort J. H., 1940, Astrophysical Journal, 91, 273

Oort J. H., 1960, Bulletin of the Astronomical Institutes of the Netherlands, 15, p.45

Ostriker J. P., Peebles P. J. E., 1973, Astrophysical Journal, 186, pp. 467-480

Planck Collaboration et al., eprint arXiv:1807.06209

Pointecouteau E., Arnaud M. & Pratt G. W., 2005, A&A 435, 17

Riess A. G., Filippenko A. V., Challis P. et al., 1998, Astronomical Journal, 116, 3, pp. 1009-1038

Rix H.-W. & Zaritsky D., 1995, Astrophysical Journal, 447, 82

Roberts M. S., 1975, IAU Symposium, Vol. 69, Dynamics of the Solar Systems, ed. A. Hayli, 331

Roberts W. W., 1969, Astrophysical Journal, 158, p.123

Rogstad D. H., Shostak G. S., 1972, Astrophysical Journal, 176, 315

Rubin V. C., Ford W. K. Jr., 1970, Astrophysical Journal, vol. 159, p.379

Rubin V. C., Ford W. K. Jr., Thonnard, N., 1978, Astrophysical Journal, Part 2 - Letters to the Editor, vol. 225, p. L107-L111

Rubin V. C., Ford W. K. Jr., Thonnard N., Burstein D., 1982, Astrophysical Journal, Part 1, vol. 261, p. 439-456

Samtleben D., Staggs S., Winstein B., 2007, Annual Review of Nuclear and Particle Science, 57, 1, 245-283

Sanders R. H., McGaugh S. S., 2002, Annual Review of Astronomy and Astrophysics, 40, p. 263-317

Schombert J., McGaugh S. S., Lelli F., 2019, MNRAS, 483, 2, p.1496-1512

Schramm D., 1998, Proc. Natl. Acad. Sci. USA, Vol. 95, pp. 42 46

Serra P., Oosterloo T., Morganti R. et al., 2012, MNRAS, 422,1835-1862

Serra P., Oser L., Krajnovic D., et al., 2014, MNRAS, 444, pp. 3388-3407

Sil'chenko O. K., Moiseev A. V., Shulga A. P., 2010, The Astronomical Journal, 140, 5, pp. 1462-1474

Smoot G. F., Bennett C. L., Kogut A. et al., 1992, Astrophys. J Lett. 396, L1

Sofue Y. & Ruben V., 2001, Annual Review of Astronomy and Astrophysics, Vol. 39, 137-174

Spitzer L. Jr., 1942, Astrophysical Journal, 95, p.329

Springel V., White S. D. M., Jenkins A. et al., 2005, Nature, 435, 7042, pp. 629-636

Steinhardt P., 1983, Bulletin of the American Astronomical Society, 15, p.956

Tinsley B. M., 1972a, Astrophysical Journal, 178, L39

Tinsley B. M., 1972b, Astrophysical Journal, 178, 319-336

Tinsley B. M., 1975, New York Academy of Sciences, Annals, 262, 436-448

Thomas D., Maraston C., Bender R., Mendes de Oliveira C., 2005, Ap. J. 621, 673-694

Tully R. B. & Fisher J. R., 1977, A&A, 54, 661

Tutukov, A. V. & Fedorova, A. V. 2006, Astron. Rep., 50, 785

van Albada T. S., Bahcall J. N., Begeman K., Sancisi R, 1985, Astrophysical Journal, Part 1, 295, p. 305-313

van Albada T. S., Sancisi R., 1986, Philosophical Transactions for the Royal Society of London. Series A, Mathematical and Physical Sciences, Volume 320, Issue 1556, pp. 447-464

van de Hulst H. C., 1945, Ned.Tijd.Natuurkunde, 11, 210

van de Hulst H. C., Raimond E., van Woerden H., 1957, Bulletin of the Astronomical Institutes of the Netherlands, Vol. 14, p.1

van der Kruit P. C., Freeman K. C., 2011, Annual Review of Astronomy and Astrophysics, 49, 1, pp. 301-371

Verheijen M. A. W. & Sancisi R., 2001, A&A, 370, 765:867

Wagoner R., Fowler W., Hoyle F., 1967, Astrophysical Journal, 148, 3

White S. D. M., Rees M. J., 1978, MNRAS, Vol. 183, 341-358

Wilson R. W., Jefferts K. B., Penzias A. A., 1970, Astrophysical Journal, 161, L43

Yildiz M. K., Serra P., Peletier R. F., Oosterloo T. A., Duc P.-A., 2017, MNRAS, 464, p.329-355

Zeldovich Ya. B., 1972, MNRAS, 160, 1

Zhao W., Braatz J. A., Condon J. J., Lo, K. Y. et al., 2018, The Astrophysical Journal, 854, 2, 12 pp.

Zwicky F., 1933, Helvetica Physica Acta, Vol. 6, p. 110-127

Books

Begeman K. G., 1987, Ph.D. thesis, Kapteyn Institute

Binney J. & Tremaine S., Galactic dynamics. Princeton University Press 2008

Buta R. J., Secular Evolution of Galaxies. Cambridge University Press 2013

Keel W. C., The Road to Galaxy Formation. Springer 2007

Mukhanov, V. F., Physical foundations of Cosmology. Cambridge University Press 2005

Sparke L. S., Gallagher III J.S., Galaxies in the Universe, An Introduction. Cambridge University Press, 2007

Thompson A. R., Moran J. M. & Swenson G. W., Interferometry and Synthesis in Radio Astronomy. Wiley-VCH 2001

Toomre A., Evolution of Galaxies and Stellar Populations, Proceedings of a Conference at Yale University, 1977, Edited by Beatrice M. Tinsley and Richard B. Larson. New Haven: Yale University Observatory, 1977

Zeldovich Ya. B., Novikov, I.D., Relativistic Astrophysics, 2: The Structure and Evolution of the Universe. University of Chicago Press, 1983

Webpages

Elhoushi M., PhD Thesis, 2011, `https://www.researchgate.net/publication/263928386_Modeling_a_Quantum_Computer`, April 2019

Essential Radio Astronomy, Digital textbook by Jim Condon, `https://science.nrao.edu/opportunities/courses/era/`, February 2019

Fahad Sulehria, Astronomical Artist, `http://www.novacelestia.com/space_art_galaxies/galaxy_classification.html`, April 2019

Acknowledgements

I would like to thank...

- my wonderful, patient, helpful and always very motivated supervisor Federico!
- Pengfei Li, for sharing his codes with me and always being happily available if I had questions about them.
- Prof. Ralf Bender, for valuable feedback that helped vastly improving this thesis.
- Mr. Dan Prole, who explained to me the basics of MCMC better than all the online resources combined.
- the Table Football Boys, who taught me how to #SmashIt.
- Jérémy Fensch, who helped me to maintain my French.
- although it's unreasonable: an extensively long list of artists, who inspired me over the 5 years of my studies and beyond.
- my amazing best friend Allison: I don't know how you can bear me, but it's wonderful that we have each other!
- my dancing partner Dino: for teaching me literally all I know in dancing.
- *all* my other friends!
- my sister and my parents for their love and constant support. ♡
- again: my **Dad**, who, not only in this work but all through my studies, had the *infinite* patience to help me, coach me and support me. Without you I would never get this degree! I love you!

Erklärung:

Hiermit erkläre ich, die vorliegende Arbeit selbständig verfasst zu haben und keine anderen als die in der Arbeit angegebenen Quellen und Hilfsmittel benutzt zu haben.

München, den

Unterschrift